



MINISTÉRIO DA CIÊNCIA, TECNOLOGIA, INOVAÇÕES E COMUNICAÇÕES
INSTITUTO NACIONAL DE PESQUISAS ESPACIAIS

sid.inpe.br/mtc-m21b/2017/03.01.23.06-TDI

NETWORKS OF PHASE OSCILLATORS: SYNCHRONIZATION AND APPLICATIONS

Celso Bernardo da Nóbrega de Freitas

Doctorate Thesis of the Graduate Course in Applied Computing, guided by Drs. Elbert Einstein Nehrer Macau, and Arkady Pikovsky, approved in February 14, 2017.

URL of the original document:

<<http://urlib.net/8JMKD3MGP3W34P/3NEN8H2>>

INPE
São José dos Campos
2017

PUBLISHED BY:

Instituto Nacional de Pesquisas Espaciais - INPE

Gabinete do Diretor (GB)

Serviço de Informação e Documentação (SID)

Caixa Postal 515 - CEP 12.245-970

São José dos Campos - SP - Brasil

Tel.:(012) 3208-6923/6921

Fax: (012) 3208-6919

E-mail: pubtc@inpe.br

**COMMISSION OF BOARD OF PUBLISHING AND PRESERVATION
OF INPE INTELLECTUAL PRODUCTION (DE/DIR-544):****Chairperson:**

Maria do Carmo de Andrade Nono - Conselho de Pós-Graduação (CPG)

Members:

Dr. Plínio Carlos Alvalá - Centro de Ciência do Sistema Terrestre (CST)

Dr. André de Castro Milone - Coordenação de Ciências Espaciais e Atmosféricas (CEA)

Dra. Carina de Barros Melo - Coordenação de Laboratórios Associados (CTE)

Dr. Evandro Marconi Rocco - Coordenação de Engenharia e Tecnologia Espacial (ETE)

Dr. Hermann Johann Heinrich Kux - Coordenação de Observação da Terra (OBT)

Dr. Marley Cavalcante de Lima Moscati - Centro de Previsão de Tempo e Estudos Climáticos (CPT)

Silvia Castro Marcelino - Serviço de Informação e Documentação (SID) **DIGITAL**

LIBRARY:

Dr. Gerald Jean Francis Banon

Clayton Martins Pereira - Serviço de Informação e Documentação (SID)

DOCUMENT REVIEW:

Simone Angélica Del Duca Barbedo - Serviço de Informação e Documentação (SID)

Yolanda Ribeiro da Silva Souza - Serviço de Informação e Documentação (SID)

ELECTRONIC EDITING:

Marcelo de Castro Pazos - Serviço de Informação e Documentação (SID)

André Luis Dias Fernandes - Serviço de Informação e Documentação (SID)



MINISTÉRIO DA CIÊNCIA, TECNOLOGIA, INOVAÇÕES E COMUNICAÇÕES
INSTITUTO NACIONAL DE PESQUISAS ESPACIAIS

sid.inpe.br/mtc-m21b/2017/03.01.23.06-TDI

NETWORKS OF PHASE OSCILLATORS: SYNCHRONIZATION AND APPLICATIONS

Celso Bernardo da Nóbrega de Freitas

Doctorate Thesis of the Graduate Course in Applied Computing, guided by Drs. Elbert Einstein Nehrer Macau, and Arkady Pikovsky, approved in February 14, 2017.

URL of the original document:

<<http://urlib.net/8JMKD3MGP3W34P/3NEN8H2>>

INPE
São José dos Campos
2017

Cataloging in Publication Data

Freitas, Celso Bernardo da Nóbrega de.

F884n Networks of phase oscillators: Synchronization and applications / Celso Bernardo da Nóbrega de Freitas. – São José dos Campos : INPE, 2017.
xviii + 85 p. ; (sid.inpe.br/mtc-m21b/2017/03.01.23.06-TDI)

Thesis (Doctorate in Applied Computing) – Instituto Nacional de Pesquisas Espaciais, São José dos Campos, 2017.

Guiding : Drs. Elbert Einstein Nehrer Macau, and Arkady Pikovsky.

1. Synchronization. 2. Chaos. 3. Dynamical system.
4. Nonlinear system. 5. Phase detectors. I.Title.

CDU 004.93'1:517.57



Esta obra foi licenciada sob uma Licença [Creative Commons Atribuição-NãoComercial 3.0 Não Adaptada](https://creativecommons.org/licenses/by-nc/3.0/).

This work is licensed under a [Creative Commons Attribution-NonCommercial 3.0 Unported License](https://creativecommons.org/licenses/by-nc/3.0/).

Aluno (a): **Celso Bernardo de Nóbrega de Freitas**

Título: "NETWORKS OF PHASE OSCILLATORS: SYNCHRONIZATION AND APPLICATIONS"

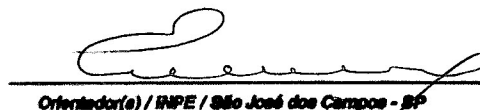
Aprovado (a) pela Banca Examinadora
em cumprimento ao requisito exigido para
obtenção do Título de **Doutor(a)** em
Computação Aplicada

Dr. **Lamartine Nogueira Frutuoso
Guimarães**



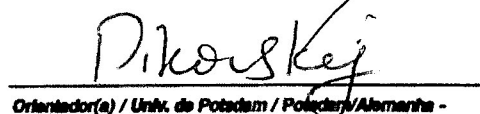
Presidente / INPE / SJCampos - SP

Dr. **Eibert Einstein Nehrer Macau**



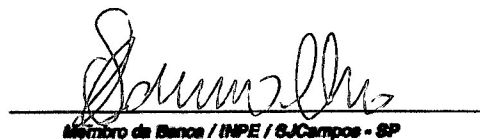
Orientador(a) / INPE / São José dos Campos - SP

Dr. **Arkadi Pikovsky**



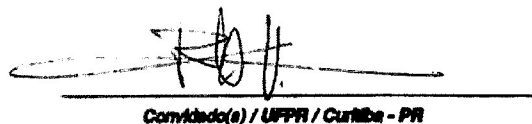
Orientador(a) / Univ. de Potsdam / Potsdam/Alemanha -

Dr. **Solon Venâncio de Carvalho**



Membro da Banca / INPE / SJCampos - SP

Dr. **Ricardo Luiz Viana**



Convidado(a) / UFPR / Curitiba - PR

Dr. **José Roberto Castilho Piqueira**



Convidado(a) / USP / São Paulo - SP

Este trabalho foi aprovado por:

maioria simples

unanimidade

São José dos Campos, 14 de fevereiro de 2017

ACKNOWLEDGEMENTS

I thank my family and friends.

I would like to thank the Coordenação de Aperfeiçoamento de Pessoal de Nível Superior - CAPES (Process: BEX 10571/13-2) for financial support.

ABSTRACT

This work explores synchronization regarding networks of active units. More specifically, we focus on the Kuramoto Model (KM), which is one of the most successful models for collective behavior. Agents here are modeled as phase-oscillators, in the sense that they are represented by a unidimensional state with a 2π increment for every complete cycle. Such model is remarkably important due to its relative simplicity and wide range of applications, either as one of its variations or as a building block for other systems. Given a time series obtained from an oscillatory phenomenon, phase assignment is the name of the process of choosing phase-variables for it. The first contribution (I) of this thesis is a test bed to evaluate phase assignment methodologies: the Double Strip Test Bed (DSTB). This is done by defining a chaotic oscillator surrogate by embedding phase-variable from a KM into suitable three dimensional surface. DSTB allows comparison between methods of phase assignment for time series since it provides an a priori reference phase-variables. For the second contribution (II), we introduce a generalization of the KM: the Deserter Hubs Model (DHM). It corresponds to a non-linear coupling scheme, where oscillators can shift from conformist to contrarian under the influence of a sufficiently large number of neighbors. This scheme holds analogy with neural synchronous oscillations at Parkinson disease. Therefore, we were able to: (i) give sufficiently conditions for phase locking; (ii) numerically show several qualitative behaviors; and (iii) correlate some of them with metrics from the corresponding coupling graph. The last contribution (III) deals with the classic version of KM, introducing a new question: Does the position of non-identical oscillators into the nodes of a graph affect synchronization? In particular, we are interested in homophily/heterophily configurations, which corresponds to multi-agents systems whose units tend to bond with others with similar/dissimilar characteristic in comparison with themselves. Thus, we present numerical evidences that Similar patterns favor the emergence of synchronization for small coupling parameter, while Dissimilar patterns undergoes abrupt synchronization for larger coupling values.

REDES DE OSCILADORES DE FASE: SINCRONIZAÇÃO E APLICAÇÕES

RESUMO

Este trabalho explora sincronização em redes de unidades ativas. Mas especificamente, foca-se no Modelo de Kuramoto (KM), um dos mais bem sucedidos modelos de comparamento coletivo. Os agentes aqui são osciladores de fase, no sentido de que são representados por uma variável unidimensional com incrementos de 2π para cada ciclo completo. Tal formulação é notavelmente importante devido a sua relativa simplicidade e vasta gama de aplicações, como uma de suas variações ou como bloco componente de outros sistemas. Dada uma série temporal obtida empiricamente, atribuição de fase é o nome do processo de escolha de várias de fase. A primeira contribuição (I) desta tese é um testbed para avaliar metodologias de atribuição de fase: o Double Strip TestBed (DSTB). Define-se para tanto um sistema caótico sintético através da imersão de variáveis de fase referenciais em uma superfície tridimensional. Com isso, o DSTB permite a comparação entre métodos de atribuição de fase. Para a segunda contribuição (II), é introduzida uma generalização do KM: o Deserter Hubs Model (DHM). Esse modelo corresponde a um esquema de acoplamento não linear, onde os osciladores podem mudar de conformistas para contrários, caso a influência dos osciladores vizinhos seja suficientemente grande. Tal esquema possui analogia com redes neurais de osciladores síncronos no contexto de mal de Parkinson. Obtém-se daí: (i) condições suficientes para travamento de fase; (ii) exemplificação de diversos comportamentos qualitativos; (iii) uma correlação entre a proporção de travamento de fase e quantificadores de rede para o grafo de acoplamento. Por fim, a contribuição (III) trata da versão clássica do KM, introduzindo uma nova questão: como o posicionamento de osciladores não idênticos nos nós de um grafo afetam a sincronização? Em particular, estudaram-se configurações do tipo homofilia/heterofilia, correspondendo a sistemas multiagentes cujas unidades tendem a conectar-se com outras que possuam características Similares/Dissimilares em comparação a eles próprios. Evidências numéricas são apresentadas mostrando que padrões Similares favorecem a emergência da sincronização para valores de acoplamento baixo, enquanto padrões Dissimilares exibem sincronização abrupta para valores elevados.

LIST OF FIGURES

	<u>Page</u>
1.1 The problem of the Seven Bridges of Königsberg. Adapted from: https://en.wikipedia.org/wiki/SevenBridgesOfKonigsberg	1
2.1 Example of graphs and graph notations: (a) simple connected graph; (b) directed graph with a self-loop and two connected components. Directed edges are depicted as blue arrows and undirected ones as black lines. Matrices A and B are the adjacency and incidence matrix of the graph in Subfig. (a).	8
2.2 Example of deterministic graphs with $N = 6$ nodes.	10
2.3 Example of ER network with $N = 250$ nodes, $M = 500$ edges: (a) graph visualization; (b) degree distribution histogram and a fitting Gaussian curve in blue. Network metrics: $GD = 11$, $GMD = 4.157$, $d_{max} = 12$, $CC = 0.019$, $\lambda_2 = 0.211$, $\lambda_N = 13.479$	10
2.4 Example of WS network with $N = 250$ nodes, $M = 500$ edges ($k = 4$ and $p = 0.25$): (a) graph visualization; (b) degree distribution histogram and a fitting Gaussian curve in blue. Network metrics: $GD = 11$, $GMD = 5.382$, $d_{max} = 8$, $CC = 0.264$, $\lambda_2 = 0.119$, $\lambda_N = 9.606$	12
2.5 Example of BA network with $N = 250$ nodes and $M = 500$ edge ($m_0 = 5$ initial clique size and $m = 2$ minimum degree): (a) graph visualization with vertex size proportional to degree; (b) degree distribution histogram and a fitting exponential curve in blue. Network metrics: $GD = 6$, $GMD = 3.47$, $d_{max} = 34$, $CC = 0.087$, $\lambda_2 = 0.604$, $\lambda_N = 35.255$	15
3.1 Original drawing of Christiann Huygens illustrating two suspended pendulum clocks. Source: https://adcs.home.xs4all.nl/Huygens/17/tekenaar.html	17
3.2 Scheme of two identical isolated pendulum showing processes α_1, α_2 (left side) and phase variables θ_1, θ_2 evolution with time (right side).	18
3.3 Scheme of two identical coupled pendulum showing processes α_1, α_2 (left side) and phase variables θ_1, θ_2 evolution with time (right side).	19
3.4 Scheme of two non-identical coupled pendulum showing processes α_1, α_2 and phase variables θ_1, θ_2 evolution with time: (a) phase-locking; (b) asynchronicity.	19

3.5	Phase assignment example for van der Pol oscillator with $\mu = 1.5$: (a) Two trajectories (in blue and orange) of (3.2) near its stable periodic solution (in black); (b) Phase variable assignment according to (3.4) along the limit cycle. Black dots mark $\theta = 0, \pi/8, \pi/4, \dots, 2\pi$; (c) Isochrone Σ corresponding to constant phase variable $\theta = 0$	20
3.6	Scheme of two identical coupled pendulum with repulsive coupling $\varepsilon < 0$, showing processes α_1, α_2 and phase variables θ_1, θ_2 evolution with time.	24
3.7	Bifurcation Diagram for the Adler Equation (3.13) with $\nu \geq 0$. The critical coupling parameter for phase-locking is $\varepsilon_{\text{PL}} = \nu/2$. Solid and dashed blue lines correspond respectively to stable and unstable equilibrium points.	25
3.8	Examples of dynamics with different values of dissonance ν and coupling parameter ε , numbered marks are depicted with unique colors representing different values of ν, ε : (a) Potential field, black corresponds to local minima ψ^* ; (b) Arnold Tongue, phase-locking occurs at the gray area defined by $ \nu \leq \varepsilon_{\text{PL}} = \nu/2$; (c) Phase difference ψ obtained after transient time.	26
3.9	Phase variables θ_i and order parameter R evolution with time for typical synchronization types: (a) Phase-locking (partial synchronization index $S = 1$) showing splay to full synchronization; (b) Phase-locking ($S = 1$) with $\langle R \rangle = 0.55$; (c) Practical phase-locking ($S = 0.98$) with $\langle R \rangle = 0.88$; (d) Phase Slips ($S = 0.95$) with $\langle R \rangle = 0.62$; (e) Periodic Order Parameter ($S = 0.78$) with $\langle R \rangle = 0.52$; (f) Asynchronicity ($S = 0.09$) with $\langle R \rangle = 0.27$. Phase variable representation in the unit circle are included as insect in subfigures (a,b) with an arrow indicating the global mean field.	28
3.10	Order parameter R as a function of coupling parameter ε for the KM (3.15). All-to-all coupling in the thermodynamic limit $N \rightarrow \infty$ with natural frequencies chosen from a Lorentzian distribution with parameter γ are considered (KURAMOTO, 1975).	30
3.11	(a) Lorenz system trajectories: (a) (x, y) and (x, z) projections of one trajectory with time color coding from 0 (Black) to 100 units of time (Cyan); (b) x, y, z components regarding two different trajectories (black and dashed/ orange) with initial conditions 0.001 apart from each other; (c) Another projection, as in the first case, in coordinates (v, z) where v is the transformation change $v = \sqrt{x^2 + y^2}$	33
3.12	Illustration of l iterations of time shift map Φ employed at Lyapunov exponents definition.	33

4.1	Rössler oscillator as in Eq. (4.2). Upper figures correspond to the coherent version and bottom figures to the non-coherent one: (a,d) x, y projection of a trajectory during 200u.t., color code ranges from cyan to blue as z increases from zero to 60; (b,e) approximately 3 cycles of the previous trajectory. The Poincaré section ($y = 0, x < 0$) is shown in magenta. (c,f) Phase assignment via four methods.	39
4.2	Additional views from the non-coherent Rössler, as in Fig. 4.1(d). The Poincaré Section $y = 0, x < 0$ is plotted in magenta. Portions of the trajectory in cyan contain sub-cycles, that is, with local minimum in x satisfying $y < 0$ and $z > 0.1$. The rest of the trajectory is shown in black.	42
4.3	(a,b,c) Double Strip Construction Scheme. (d) Two spins of the trajectory, each one over a different strip. (e) The Poincaré Return Map of section S . The Poincaré Section S is depicted in Magenta.	44
4.4	DSTB example with two coupled oscillators: (a,d) Phase locking (d,e) Phase Slip (c,f) Phase locking. The upper pictures are the oscillators . . .	47
5.1	Numerical results for Model (5.1) as a function of ε , for the coupling graphs despited as inset, including 10 random initial conditions. A black line corresponds to $\text{mean}\{\langle R \rangle\}$, while the interval between $\text{min}\{\langle R \rangle\}$ and $\text{max}\{\langle R \rangle\}$ is shown as a gray strip. The gap between $\text{min}\{R_{\text{min}}\}$ and $\text{max}\{R_{\text{max}}\}$ is shown as an orange strip. Since the orange strip is by construction larger or equal than the gray one, the first one is not displayed in the figure when they coincide. Left vertical axes show values related to norm of the order parameter, while the right ones represents the maximum Lyapunov exponent λ_{max} , shown as a red dashed line. Letters in green vertical lines from the upper experiment correspond to subfigures in Fig. 5.2.	54
5.2	Evolution of $R(t)$ for different values of ε indicated in green at the upper experiment from Fig. 5.1. Every color represents a different initial condition, while pairs of solid/dashed lines with the same color correspond to solutions whose initial conditions differ not more than 10^{-4} at each coordinate. (a) $\varepsilon = 0.04$: full synchronization; (b) $\varepsilon = 0.08$: fixed phase synchronization; (c,d,e) $\varepsilon = 0.15, 0.28, 0.35$ respect.: examples of multi stability; (f) $\varepsilon = 0.70$: example with $\lambda_{\text{max}} > 0$	55

5.3	Example of group formation: details of one of the trajectories from Fig. 5.2 (b) $\varepsilon = 0.08$. On the left side, the coupling graph with $s(i, j)$ in its edges is shown. On the right side, a histogram of $\theta_i - \psi$ in permanent regime is presented with color code representing the normalized frequency. Precisely, we divided the interval $[0, 2\pi)$ into 10 bins with the same size. So, the normalized frequency of the i -th oscillator corresponds to the ratio of points (after the transient time) that the numerical evaluation of $\theta_i - \psi$ placed at each bin.	56
5.4	Example multi-stability with group formation. Details of two trajectories from Fig. 5.2 (c) $\varepsilon = 0.15$ are provided. The left picture corresponds to the solid black line and the right one to the solid blue. Histograms of $\theta_i - \psi$ are like the one in Fig. 5.3.	57
5.5	Example of periodic norm of the order parameter: details of one of the trajectories from Fig. 5.2 (d) $\varepsilon = 0.28$. On the left side, the coupling graph with $s(i, j)$ in its edges is shown. A histogram of $\theta_i - \psi$ are like the one in Fig. 5.3 in the middle figure. We denote by $\psi(t)$ the argument of the order parameter. The picture on the right shows that the curve $(\sin(\theta_1(t) - \psi(t)), \sin(\theta_9(t) - \psi(t)))$ is closed.	58
5.6	Example of trajectory with $\lambda_{\max} > 0$: details of one of the trajectories from Fig. 5.2 (f) $\varepsilon = 0.70$. On the left side, the coupling graph with $s(i, j)$ in its edges is shown. On the right side, there is a histogram of $\theta_i - \psi$ are like the one in Fig. 5.3.	59
5.7	Numerical results for Model (5.1) as a function of ε , for the coupling graphs depicted as insect, including 10 random initial conditions. The legend of the pictures is the same as in Fig. 5.1	60
5.8	Convergence index I_c versus γ^* . Networks with $N = 10, 50, 100$ nodes are represented as circles, squares and triangles, respectively. The two experiments from Fig. 5.1 are shown as disks. We show in red an exponential fit $f(x) = e^{1.7676-1.0894x}$ for the data.	61
6.1	Examples of Similar, Neutral and Dissimilar patterns related to N -nodes graphs following network topology: 4-Regular (50 RE); Barabási-Albert (50 BA); a community graph (105 CO). Vertex color is presented according to its natural frequency ω_i , ranging from $-\pi$ (blue) to π (red); vertex size is proportional to node-degree. The associate total dissonance ν_{Total} is shown.	67

6.2	Total Dissonance ν_{Total} distribution chart of different topologies with Similar (Blue), Neutral (Gray) and Dissimilar (Orange) patterns. Data correspond to the single members from categories 50 RE, 500 RE and 105 CO; and 100 different elements for the others. Colored bars indicate the overall range of ν_{Total} obtained, while mean values of each distribution are joined by a black line within each category.	68
6.3	Mean order parameter after transient $\langle R \rangle$ and partial synchronization index S , solid and dashed lines resp., as a function of coupling strength ε for different graph topologies. Average values of all graphs simulated within each category are shown. Similar, Neutral and Dissimilar cases are respectively plotted in Blue, Gray and Orange. Lines are drawn up to ε equal to the respective average critical phase-locking ε_{PL}	69

LIST OF TABLES

	<u>Page</u>
5.1 Mean value of I_c and its standard deviation (in brackets) for each network type and size simulated.	61

CONTENTS

	<u>Pág.</u>
1 INTRODUCTION	1
1.1 Complex networks as an interdisciplinary science	1
1.2 Collective Behavior and Synchronization	2
1.3 Contributions	4
1.4 Thesis Structure	5
2 COMPLEX NETWORKS	7
2.1 Elements of graph theory	7
2.2 Networks Metrics	8
2.3 Deterministic topologies: All-to-all, k -Regular and Ring networks	9
2.4 Random networks: the Erdős Rényi topology	10
2.5 Small-World networks: Watts-Strogatz topology	11
2.6 Scale free networks: Barabási-Albert topology	13
3 SYNCHRONIZATION	17
3.1 Preliminary concepts	17
3.2 Reduction to phase oscillators	20
3.3 A model of mutually coupled oscillators	23
3.4 Kuramoto model	26
3.5 Synchronization Metrics	28
3.6 Two classic results of phase oscillators networks	30
3.7 Notes about Kuramoto Model Numerical Integration	31
3.8 Chaotic oscillators and Lyapunov exponents	32
3.9 Some generalizations of coupled oscillators networks	35
4 THE DOUBLE STRIP TEST BED FOR PHASE ASSIGNMENT METHODS	37
4.1 Phase assignment for chaotic oscillators	38
4.1.1 About accuracy techniques for phase assignment methods	41
4.2 The DSTB construction	43
4.3 Example of DSTB usage	45
4.4 Conclusions and perspectives	46

5	DESERTER HUBS MODEL	49
5.1	The Deserter Hubs Model (DHM)	50
5.2	Stability of full synchronization	51
5.3	Examples of behaviors	53
5.4	Dependence of partial synchronization regimes on network structure	59
5.5	Conclusion	62
6	SYNCHRONIZATION VERSUS NEIGHBORHOOD SIMILARITY	63
6.1	Numerical Experiment Setup	64
6.2	Similar, Neutral and Dissimilar neighborhood patterns	65
6.3	Simulation Results	68
6.4	Conclusion	69
7	CONCLUSION AND OUTLOOK	71
	References	73
	Appendix 1: The discrete complex wavelet approach to phase assignment and a new test bed for related methods	85
	Appendix 2: Partial synchronization in networks of non-linearly coupled oscillators: The Deserter Hubs Model.	103
	Appendix 3: Synchronization versus neighborhood similarity in complex networks of nonidentical oscillators	113

1 INTRODUCTION

1.1 Complex networks as an interdisciplinary science

Several authors choose Euler's solution of the Königsberg problem (EULER, 1741) as the starting point to introduce complex networks. At the end of sec. XVIII, that problem was merely a cultural trivia with unknown answer, asking whether it is possible to find a path that crosses each of the seven bridges, as depicted in Fig. 1.1(a), once and only once.

More important than Euler's answer itself, his abstraction level taking into account the relation between nodes and edges, that is, system units and the interconnections between them (Fig.1.1(b)), became the core of modern graph theory.

Another major landmark of the field was the Erdős-Rényi model (ERDÖS; RÉNYI, 1959), which aimed to describe larger real-life networks not necessarily based on its individual shapes, but in terms of their formation rules and statistical properties, what eventually became known as *complex networks*. This network topology corresponds to random graphs and they were extensively and successfully studied through algebraic and number theory.

As computational power and experimental data availability grew, Ref. (WATTS; STROGATZ, 1998) provided evidences that hardly any sufficiently large complex network fit into the Erdős-Rényi model. Yet, the authors of that article introduced the concept of *small-world networks*, which are characterized by chains of highly

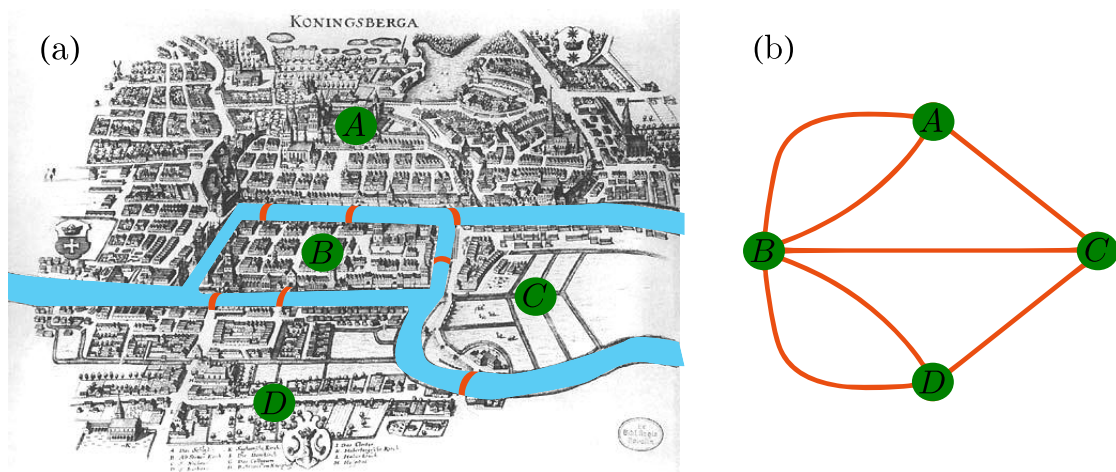


Figure 1.1 - The problem of the Seven Bridges of Königsberg. Adapted from: <https://en.wikipedia.org/wiki/SevenBridgesOfKönigsberg>

clustered nodes combined with random long-range edges, yielding smaller graph diameter. After that, small-world structure have been reported at metabolic networks (JEONG et al., 2000), foodwebs (MONTROYA; SOLÉ, 2002), co-authorship of mathematicians (BARAHONA; PECORA, 2002), on the level of cortical in the brain (SPORNS; ZWI, 2004), among others.

Even so, small-world framework could not explain the node degree heterogeneity found for instance at links among sites in the World Wide Web. Thus, Ref. (BARABÁSI; ALBERT, 2002) introduced the so-called *scale-free networks*, which are characterized by the existence of hubs, that is, a few nodes have a very large number of connections, whereas most of them have only a few. Examples of scale-free networks were later found in several of social and biological contexts like social networks (BARABÁSI, 2009), citation networks (BARABÁSI et al., 2002) and the interaction network of proteins (JEONG et al., 2001).

Among other complex networks features we cite community structure (NEWMAN, 2012), symmetry patterns (MACARTHUR et al., 2008), hybrid topologies (CHUNG; LU, 2004) and time varying networks (CASTEIGTS et al., 2012).

1.2 Collective Behavior and Synchronization

Technology has lead humankind to unprecedented interconnectivity. By 2020, there will be 50 to 100 billion devices connected to the so called Internet of Things (TRAPPENIERS et al., 2013). Therefore, strategies to collectively ensure safety, reliability and rational use of resources will become even more critical from communicating household appliances (REINISCH et al., 2010), self balancing cloud storage servers (BONVIN et al., 2010) and electrical power grid networks (BROWN, 2008), to name a few applications.

As the numbers of members of such systems scale up, the cost to control the entire group from a single master authority often becomes unfeasible (WURMAN et al., 2008). Another requirement, which is crucial for ensembles of autonomous vehicles and also spacecraft formation (NAG; SUMMERER, 2013; BENNET; MCINNES, 2012), is robustness against communication failures and time delay (ZHANG et al., 2013). As a result, each of these synthetic ecosystems demand low or even the absence of a centralized control (TURCI; MACAU, 2012).

A scenario which encompass all these features is provided by the collective behavior (STROGATZ, 2001; SARNE; GROSZ, 2013; GURUPRASAD; GHOSE, 2013; CANEDO-

RODRIGUEZ *et al.*, 2012). Broadly speaking, dynamics emerges here from the interaction of individual active units. Consider, as example, swarm intelligence (ZHANG *et al.*, 2014), where members individually follow simple rules whose combined outcome yields sophisticated group properties. As in the Aristotle's memorable quote, one tries to unravel how the whole becomes larger than the sum of its parts, inspired by biological systems (VICSEK; ZAFEIRIS, 2012). About flocks of birds, Ref. (THIEBAULT *et al.*, 2014) argues that aggregation and flocking improves foraging (THIEBAULT *et al.*, 2014), while (CAVAGNA *et al.*, 2015) discusses group turning. School of fishes can be seen as models to cooperation and social decision making (BSHARY *et al.*, 2014). Besides, collective motion could be an evolutionary response to detect and respond to predators (IOANNOU *et al.*, 2012).

Our present work focus on collective behavior that emerges from networks of coupled oscillators (BARABÁSI, 2003; TANNER *et al.*, 2003; OLFATI-SABER; MURRAY, 2004; LIN *et al.*, 2004; PALEY *et al.*, 2005; LEONARD *et al.*, 2007). At scenario, active agents are identified with the cycles they describe in phase space, in analogy to undamped simple pendulums (FIGUEIREDO; NEVES, 2005). Oscillators influence each other through communication channels defined by coupling network edges, allowing them to evolve from unordered initial conditions towards ordered configurations fostered by the adjustment of their rhythms. This phenomenon is generically called synchronization and commonly conveys swarm intelligence in the form information/energy flow, which can be expressed in a myriad of qualitative behaviors like full-synchronization, phase-locking, intermittent synchronization, remote synchronization, chaos, chimeras (REKA; BARABÁSI, 2002; BOCCALETTI *et al.*, 2006; YU *et al.*, 2010; JI *et al.*, 2013; PIKOVSKY *et al.*, 2003; BALANOV *et al.*, 2010).

There are ubiquitous phenomena in biological systems that can be studied as networks of coupled oscillator. It is the case of heart cells, which oscillates according to the rhythm originated from the sinoatrial node (HUANG *et al.*, 2011; SHOUCRI, 2011); primary visual cortex experiments provide strong evidence that neuron synchronization plays fundamental role at the sensory integration of the different visual field parts (BEER, 2014; FREEMAN *et al.*, 2013); the proper function of the hippocampus in the brain would be related with complex pattern of chaotic spatial-temporal activities produced by neuron network (CESSAC; SAMUELIDES, 2007; ZEMANOVÁ *et al.*, 2006), whose change in synchronization level is associated with epileptic seizure (CYMERBLIT-SABBA; SCHILLER, 2010).

One could also cite engineering challenges from astronomy and astrophysics, for

instance, the *Very Large Array (VLA)* (QUIRRENBACH, 2001), which is a radio-astronomy interferometer. Nowadays, this array corresponds to 27 antennas of 25m diameter, geometrically distributed in a “Y” shape in the American city of Socorro, New Mexico. Such arrangement could be more efficient by embedding their antennas into satellites, so they could occupy larger areas and be free of atmospheric interferences.

In applications like this, we have autonomous agents whose dynamics must remain synchronized, in the sense that their relative position and direction must satisfy certain properties (LEONARD et al., 2007). Moreover, such formation must be robust under travel control and be capable of reconfiguration for different observation objectives (SCHARF et al., 2003; SCHARF et al., 2004).

1.3 Contributions

The core of this thesis is a mathematical model of non-identical phase-oscillators, mutually coupled via common mean field: the Kuramoto Model (KM) (KURAMOTO, 1975), first introduced for chemical oscillators. Roughly speaking, a phase-oscillator corresponds to a cyclic unit whose dynamics is parametrized by a continuous quantifier with 2π increase for every complete revolution.

Studying this system, Kuramoto identified a synchronization transition to an oscillating global mode when the coupling strength is larger than a critical value, which is proportional to the range of the distribution of the natural frequencies. Over the time, subsequent outcomes based on Kuramoto propositions have shown that his approach can be used as a framework to several natural and technological systems where an ordered behavior (synchronization) emerges from the interactions of many dynamical agents (ACEBRÓN et al., 2005; STROGATZ, 2000).

Furthermore, others have shown that the KM can be exploited as a building block to develop highly efficient strategies to process information (FOLLMANN et al., 2015; VASSILIEVA et al., 2011) and distributed multi-agent coordination (LEONARD et al., 2007; CAO et al., 2013).

The first contribution (I) of our present work deals with a practical issue related to the phase assignment problem (PIKOVSKY et al., 2003). Some synchronization regimes like phase-locking can be characterized only in terms of phase-variables. However, assigning such variables to time series from experimental data is not trivial, specially for chaotic oscillator with non-well defined rotation center. There are

several numeric methods to perform this task, but the comparison between these methods is not straightforward. Thus, we introduced at Ref. (FERREIRA et al., 2015), *The discrete complex wavelet approach to phase assignment and a new test bed for related methods* Appendix A, a test bed for this class of problems. It applies the KM by embedding trajectories of its units into a three-dimensional surface, and using them as the input for phase assignment techniques. This approach was innovative since it provided a priori reference phase variables, improving the cross analyzes of phase assignment techniques.

The second contribution (II) is a generalization of the KM introduced at Ref. (FREITAS et al., 2015a), *Partial synchronization in networks of non-linearly coupled oscillators: The Deserter Hubs Model (DHM)*, Appendix B. It introduces a non-linear coupling schemes, in such a way that oscillators can shift from attraction to repulsive behavior if the pressure by a sufficiently large number of neighbors becomes too intense. Such design is motivated by stimulation of neural synchronous oscillations at Parkinson disease by a nonlinear feedback (POPOVYCH et al., 2005). As a result, we were able to provide sufficient conditions for stable phase-locking in the DHM and also illustrate a myriad of other qualitative dynamics regimes.

Finally, our third contribution (III) from Ref. (FREITAS et al., 2015b), *Synchronization versus neighborhood similarity in complex networks of non-identical oscillators*, Appendix C, deals with the classic version of KM, introducing a new question: Does the position of non-identical oscillators into the nodes of a graph affect synchronization? In particular, we are interested in homophily/heterophily configurations (LOZARES et al., 2014), which corresponds to multi-agents systems whose units tend to bond with others with similar/dissimilar characteristic in comparison with themselves. The individuality of each oscillator here is expressed by its natural frequency. Thus, we present numerical evidences that Similar patterns favor the emergence of synchronization for small coupling parameter, while Dissimilar patterns undergoes abrupt synchronization for larger coupling values.

1.4 Thesis Structure

This text is divided into two parts. In the first one, comprising the first two chapters, we lay the theoretical foundation for our results, while the main contributions of this work are presented in the second part.

In Chap. 2, we include the complex networks outline. One will find there the terminology used, graph notations and metrics, common complex network topologies, as

well as their associated algorithms for construction.

Synchronization is the subject of Chap. 3. We tried to select topics from the theory to provide a concise path from the subjective idea of rhythm adjustment until the Kuramoto Model, including some of its classic properties. Several qualitative synchronization regimes and metrics to characterize them are also discussed, like the mean field and partial synchronization index (GÓMEZ-GARDEÑES et al., 2007).

After that, we have the second part starting at Chap. 4 with contribution (I). Since the DCWA was already deeply discussed in another PHD thesis from our research group (FERREIRA, 2014), we focus on the test bed for phase assignment methods itself. We perform an overview of this class of problems, analyzing via test beds some common techniques to solve them.

Then, our studies contribution (II) and (III) are given in Chapters 5 and 6, respec.

Ideas for future research and a summary of the conclusions can be found in the Chap. 7.

2 COMPLEX NETWORKS

Complex Networks corresponds to an abstraction level of systems regarding solely static elements and the interconnections among them. The language to describe these networks comes from graph theory (STEEN, 2010), so we introduce in this chapter some of its concepts and notations. The terms network and graph are regarded here as synonyms.

Actually, the adjective “complex” emphasizes that units bound to each other follow statistical properties, commonly called network topologies (BARABÁSI; ALBERT, 2002). The network metrics and the topologies employed in this work are discussed in the following sections.

2.1 Elements of graph theory

A graph $G = (V, E)$ consists of a set of *vertices* (or *nodes*) $V = \{v_1, \dots, v_N\}$ and a set of *directed edges* $E = \{e_1, \dots, e_M\}$ of pairs, where $e_k = (v_i, v_j)$ and $v_i, v_j \in V$. The symbols v_1, \dots, v_N are merely vertex labels. If $(v_i, v_j) \in E$ we say that v_i is *connected* (or *adjacent*) to v_j . A *subgraph* $\tilde{G} = (\tilde{V}, \tilde{E})$ conveys the idea of a graph inside the graph, that is, \tilde{G} is a graph satisfying $\tilde{V} \subset V$ and $\tilde{E} \subset E$.

If $(v_i, v_j) \in E$ implies that (v_j, v_i) also belongs to E , then we say that the graph is *bidirectional* (or *undirected*), in contrast with the general *directed* case. Unless explicitly stated, the term edges refers to bidirectional edges. Connected nodes are also called *neighbors* and the set of all neighbors of a node is its *neighborhood*. A self-loop is an edge which connects a vertex $v_i \in V$ to itself, that is, $(v_i, v_i) \in E$. A bidirectional graph without self-loops is called *simple*.

A graph is called *connected* or *convex* if for any two vertices $v_i, v_j \in V$, there is a sequence of edges connecting them. Otherwise, we say that the graph is *unconnected*. All subgraphs of G satisfying the connectivity property are called *connected components* of G . Clearly, any connected graph has at least $N - 1$ edges.

We restrict ourselves to simple connected graphs in this work, see Fig. 2.1. As will be presented in the next chapter, in terms of networks of coupled oscillators, it means that all influences are mutual, there is no self direct feedback in the node.

An N -vertices graph may be represented by its *adjacency matrix*, which is a $N \times N$ matrix A . If the i -th vertex is connected with the j -th then $A_{ij} = 1$, otherwise $A_{ij} = 0$. The absence of self-loops and the edge bidirectionality imply that A is a

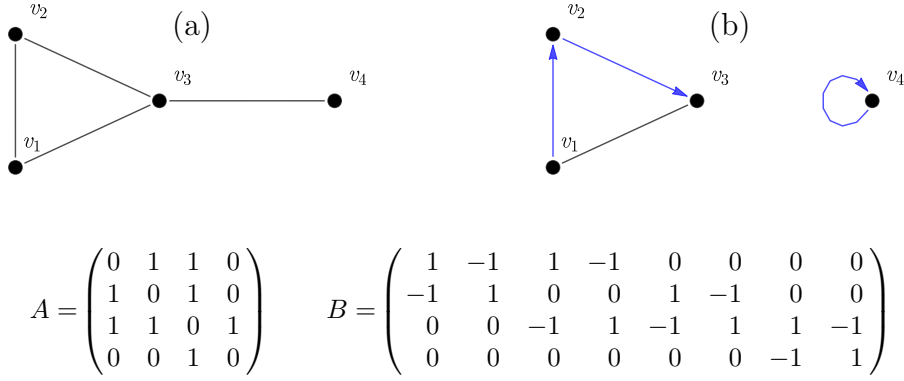


Figure 2.1 - Example of graphs and graph notations: (a) simple connected graph; (b) directed graph with a self-loop and two connected components. Directed edges are depicted as blue arrows and undirected ones as black lines. Matrices A and B are the adjacency and incidence matrix of the graph in Subfig. (a).

symmetric matrix with zeros in its diagonal.

Other graph notations are also available. Let B be the *incidence matrix* of a graph. Thus, B is a matrix with N rows and M columns, where M is the number of *directed edges* of the network. The columns of B represent the directed edges of the graph: if the k -th directed edge of the graph goes from the i -th node to the j -th node, then all entries in the k -th column of matrix B will null, except for entries $B_{ik} = 1$ and $B_{jk} = -1$.

2.2 Networks Metrics

Network metrics¹ allows us to quantitatively evaluate graphs properties. Of course, the network size N , the quantity of edges M and the quantity of connected components are network metrics.

The *Graph Mean Distance* (GMD) conceals information about communication efficiency in the graph. This quantifier is defined as the mean path length connecting the shortest path between every two vertices in the network, that is,

$$\text{GMD} = \frac{1}{N(N-1)} \sum_{i,j=1}^N \text{dist}(v_i, v_j), \quad (2.1)$$

where $\text{dist}(v_i, v_j)$ denotes the shortest path in the graph between v_i and v_j . If there is no connection between v_i and v_j , $\text{dist}(v_i, v_j) = \infty$. Similarly, the *Graph Diameter*

¹We employ the term metric in this text as a synonymic to quantifier.

(GD) is defined as the maximum value of $\text{dist}(v_i, v_j)$ over all $v_i, v_j \in V$.

The quantity of neighbors of the i -th node d_i is called its (*node*) *degree*. In terms of the adjacency matrix A , we have that $d_i := \sum_{j=1}^N A_{ij}$. From the algebraic point of view, we can make use of the *Laplacian matrix* of a graph $L := \text{diag}(d_1, \dots, d_N) - A$, where $\text{diag}(\cdot)$ is the $N \times N$ null matrix except for its diagonal². The main interest here is about the eigenvalues of L : $0 \leq \lambda_2 \leq \dots \leq \lambda_N$. The second eigenvalues λ_2 is known in the literature as the *algebraic connectivity*. It can be proven that $\lambda_2 > 0$ if and only if the graph is connected (LI; ZHANG, 1998). Besides, λ_2 is positively correlated with the graph diameter, while there is a negative correlation between d_{\max} and λ_N (LI; ZHANG, 1998).

The *degree distribution histogram* is another tool to statistically characterize network topologies. Yet about this histogram, if one fits a curve (node degree \times density) with $y(x) = cx^{-\gamma}$, this parameter γ is associated with the Scale-Free property to be explored later.

The (*global*) *clustering coefficient* measures the tendency of nodes to gather and its is based on triplets, which are groups of three nodes sharing only two edges (open triples) or three edges (closed triples). More specifically, this measure corresponds to the ratio between the quantity of close triplets over the total number of triples in the graph (open and closed) (BARABÁSI; ALBERT, 2002).

These metrics will be illustrated in the following sections along with ways to construct some common network topologies. The reader may be aware that although there is no restriction about N for the algorithms, the statistical properties may be significant only for sufficient large network sizes.

2.3 Deterministic topologies: All-to-all, k -Regular and Ring networks

The *All-to-all* (or *Full* or *Complete*) network topology corresponds to graphs with all possible edges. In other words, for every two vertices in the graph, there is an edge connecting them.

A graph is called *k -Regular* when all its nodes have precisely degree k . Since multiple edges between nodes are not allowed, a Regular graph with N nodes has to satisfy $k \leq N - 1$. We consider k to be even so, if one fixes vertex labels $V = \{v_0, \dots, v_{N-1}\}$, then v_i connects with $v_{i-k/2}, \dots, v_{i-1}, v_{i+1}, \dots, v_{i+k/2}$, where sub-index sum is mod-

²We can also express the Laplacian matrix as $L = 1/2BB^\top$, where B is its incidence matrix and $^\top$ denotes matrix transpose

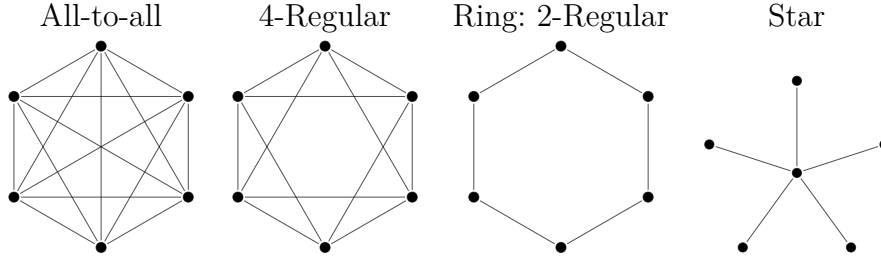


Figure 2.2 - Example of deterministic graphs with $N = 6$ nodes.

ulus N .

The 2-Regular case is commonly known as *Ring*. The graph with N nodes and $N - 1$ edges, where there is a single central node v_0 connecting all other $N - 1$ nodes is called *Star* topology. See Fig. 2.2.

For instance, All-to-all graphs yield $\lambda_2 = \dots = \lambda_N = N/(N - 1)$; while star graphs have $\lambda_2 = \dots = \lambda_{N-1} = 1$, $\lambda_N = 2$.

2.4 Random networks: the Erdős Rényi topology

Regular networks can be important for theoretical and some engineering applications, but they are seldom found in social or biological systems (BARABÁSI; ALBERT, 2002). One of the firsts attempts to model these systems occurred in 1959 by Paul Erdős e Alfréd Rényi. The *Erdős Rényi* (ER) topology regards graphs built by randomly picking edges with uniform distribution, without repetition. As we want to generate connected graphs, the Alg. 2.1 constructs first a connected component \mathcal{U}

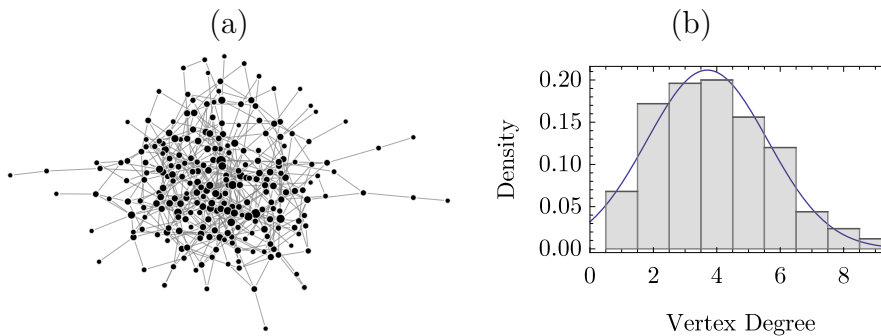


Figure 2.3 - Example of ER network with $N = 250$ nodes, $M = 500$ edges: (a) graph visualization; (b) degree distribution histogram and a fitting Gaussian curve in blue. Network metrics: $GD = 11$, $GMD = 4.157$, $d_{max} = 12$, $CC = 0.019$, $\lambda_2 = 0.211$, $\lambda_N = 13.479$.

and then adds the remaining $M - (N - 1)$ random edges. The complementary set of \mathcal{U} relative to V is denoted by \mathcal{U}^C .

Algorithm 2.1 Generate Connected ER Graph

Input: Network sizes N ; quantity of edges M , with $M \geq N - 1$

Output: Graph $G = (V, E)$

```

1:  $V \leftarrow \{v_1, \dots, v_N\}$  ▷ Node label definition
2:  $E \leftarrow \{\}$ 
3: Pick any  $w \in V$ .
4:  $\mathcal{U} \leftarrow \{w\}$ 

5: For  $i \leftarrow 1$  until  $N - 1$  do: ▷ Stage 1: Building connected component
6:   Pick any  $v \in \mathcal{U}^C$ .
7:   Pick any  $w \in \mathcal{U}$ .
8:    $\mathcal{U} \leftarrow \mathcal{U} \cup \{v\}$ 
9:    $E \leftarrow E \cup \{(v, w)\}$ 
10: End For

11: For  $i \leftarrow N$  until  $m$  do: ▷ Stage 2: Adding the remaining edges
12:   Pick any  $v, w \in V$ , such that  $(v, w) \notin E$ 
13:    $E \leftarrow E \cup \{(v, w)\}$ 
14: End For

```

See Fig. 2.3(a) for an example of this network topology. Since there is no preferential attachment rule to establish edges in the ER topology, node degree distribution is close to Gaussian (Fig. 2.3(b)).

2.5 Small-World networks: Watts-Strogatz topology

Clustering is a common property in social networks, with groups sharing high edge density (BARABÁSI; ALBERT, 2002). This characteristic refers for instance to circle of friends, but ER topology does not exhibit it. Thus, Duncan J. Watts e Steven Strogatz develop their model in 1998 to allow clustering while retaining the short average path lengths of the ER model.

The *Watts-Strogatz* topology (WS) is a family of graphs based on the rewiring parameter³ $p \in [0, 1]$. First, a k -Regular graph is constructed, then each edge is

³Newman-Watts is another small-world topology which inserts new edges instead of rewiring existing ones.

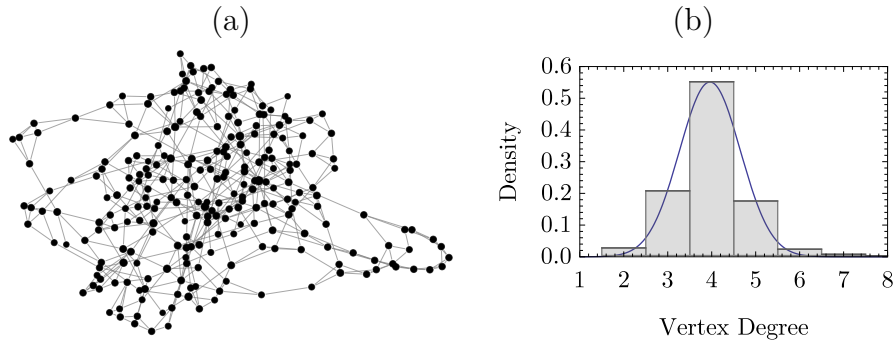


Figure 2.4 - Example of WS network with $N = 250$ nodes, $M = 500$ edges ($k = 4$ and $p = 0.25$): (a) graph visualization; (b) degree distribution histogram and a fitting Gaussian curve in blue. Network metrics: $GD = 11$, $GMD = 5.382$, $d_{max} = 8$, $CC = 0.264$, $\lambda_2 = 0.119$, $\lambda_N = 9.606$.

rewired with probability p . As a result, WS networks interpolates between k -Regular ($p = 0$: no rewiring), to ER Graphs ($p = 1$: all edges rewired). The graph connectivity check (STEEN, 2010) was included at Alg. 2.2 because this property may be violated during the rewiring phase. Unless explicitly state, we employ WS topology with $p = 0.25$.

Algorithm 2.2 Generate Connected WS graph

Input: Network size N ; mean degree $0 < k \leq N - 1$; rewiring probability $p \in [0, 1]$ **Output:** Graph $G = (V, E)$, with $M = Nk/2$ edges

```
1:  $V \leftarrow \{v_0, \dots, v_{N-1}\}$  ▷ Node label definition
2:  $A \leftarrow \{\}$ 

3: For  $i \leftarrow 0$  until  $N - 1$  do: ▷ Stage 1:  $k$ -Regular graph
4:   For  $j \leftarrow 1$  until  $k/2$  do:
5:      $A \leftarrow A \cup \{(v_i, v_{i+j})\}$ 
6:   End For
7: End For

8: For all  $(v, w) \in E$  do: ▷ Stage 2: Rewiring edges
9:    $r \leftarrow \text{RandomBetween}[0, 1]$ 
10:  If  $r \leq p$  Then
11:     $E \leftarrow E / \{(v, w)\}$  ▷ Remove  $\{(v, w)\}$  from  $E$ 
12:    Pick  $u \in V$  such that  $(u, v) \notin E$ 
13:     $E \leftarrow E \cup \{(u, v)\}$ 
14:  End If
15: End For

16: If  $G = (V, E)$  is not connected Then ▷ Accept only connected graphs
17:   Go to 1:
18: End If
```

Fig. 2.4 illustrate this topology. Note that its CC is more than ten times larger than the CC obtained in the ER example 2.3.

2.6 Scale free networks: Barabási-Albert topology

ER and WS topologies successfully described some important phenomena, even so, they could not explain most of the large scale networks like interconnections at the World Wide Web; the collaboration of movie actors in films or Protein-protein interaction networks. Therefore, Réka Albert and Albert-László Barabási ([BARABÁSI; ALBERT, 2002](#)) proposed their the *Barabási-Albert* (BA) topology. The main characteristic of it is the presence of hubs, that is, few nodes with remarkably high degree, while the majority of nodes remain with few connections⁴.

BA networks are parameterized by m_0, m , with $m_0 \geq m$. First, a clique⁵ with m_0

⁴Some authors refer to such topology as without scale

⁵A clique is subgraph where all nodes are neighbors among themselves, that is, it is an all-to-all

nodes is constructed and we define it as the initial connected set \mathcal{U} , like in the ER algorithm. Each remaining node joins the connected set through m edges, so m is the minimum node degree by construction. This new edges follow a *preferential attachment* rule in such a way that the probability of a node $w \in \mathcal{U}$ to be selected is

$$P(w) = \frac{\sigma(w)}{\sum_{w \in \mathcal{U}} \sigma(w)}, \quad (2.2)$$

where $\sigma(v)$ denotes its degree of v .

From Fig. 2.5 we observe a *Scale-Free* BA network, meaning that its degree distribution fits a power law. It is commonly assumed for this property to hold that the exponential parameter γ belongs to the interval $[2, 3]$.

Algorithm 2.3 Generate Connected BA graph

Input: Network size N ; initial clique size m_0 ; minimum degree m

Output: Graph $G = (V, E)$, with $M = m_0(m_0 - 1)/2 + (N - m_0)m$ edges

```

1:  $V \leftarrow \{v_1, \dots, v_N\}$  ▷ Node label definition
2:  $A \leftarrow \{\}$ 

3: Set  $\mathcal{U} = \{v_1, \dots, v_{m_0}\}$ ,  $m_0$  ▷ Stage 1: Building initial clique
4: For  $i \leftarrow 1$  until  $m_0 - 1$  do:
5:   For  $j \leftarrow i + 1$  until  $m_0$  do:
6:      $A \leftarrow A \cup \{(v_i, v_j)\}$ 
7:   End For
8: End For

9: For  $i \leftarrow m_0 + 1$  until  $N$  do: ▷ Stage 2: Connecting the remaining nodes  $\mathcal{U}$ 
10:   For  $j \leftarrow 1$  until  $m$  do:
11:     Draw  $w \in \mathcal{U}$ , according to (2.2), such that  $(v_i, w) \notin A$ .
12:      $A \leftarrow A \cup \{(v_i, w)\}$ 
13:   End For
14:    $\mathcal{U} \leftarrow \mathcal{U} \cup \{w\}$ 
15: End For

```

subgraph.

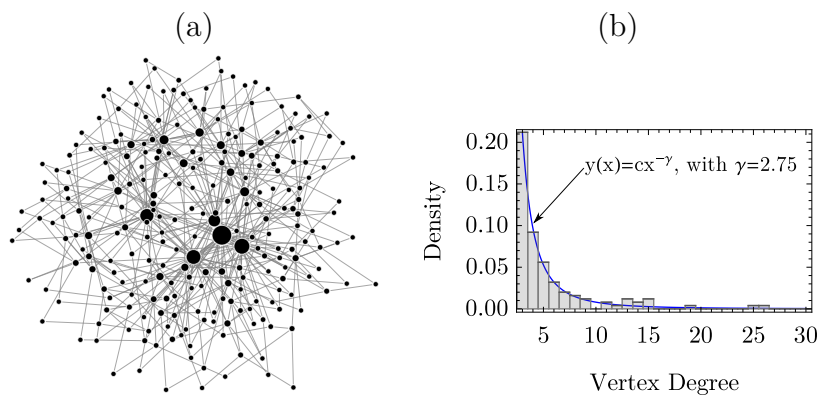


Figure 2.5 - Example of BA network with $N = 250$ nodes and $M = 500$ edge ($m_0 = 5$ initial clique size and $m = 2$ minimum degree): (a) graph visualization with vertex size proportional to degree; (b) degree distribution histogram and a fitting exponential curve in blue. Network metrics: $GD = 6$, $GMD = 3.47$, $d_{max} = 34$, $CC = 0.087$, $\lambda_2 = 0.604$, $\lambda_N = 35.255$.

3 SYNCHRONIZATION

The main synchronization concepts employed in this thesis are presented in this chapter, laying down the background results and terminology, with emphasis in phase-oscillators. Most of the content is based on classic literature of the area (YU et al., 2010; JI et al., 2013; PIKOVSKY et al., 2003; BALANOV et al., 2010).

Observations regarding massive numerical integration of coupled oscillator networks, Sec. 3.7, and chaotic oscillators, Sec. 3.8 and 3.9, are included as well.

3.1 Preliminary concepts

The study of oscillator synchronization is credited to Christiaan Huygens, a prominent Dutch mathematician and scientist from the XVII century, at what he described as “sympathy of two clocks”. In his experiment, two suspended clock pendulums, like in Fig. 3.1, spontaneously adjusted their rhythms due to a small but non-negligible motion of the beam holding them.

This phenomenon is probably the simplest coupled oscillators prototype, so we will describe it as foundation. Let α denote the pendulum bob angle related to the rest position, which is assumed to be periodic with period T . We say that θ is a *phase variable* for the pendulum, or any oscillatory process, if it is a quantifier of its periodic motion, with increments of 2π for each complete period. A more accurate definition of phase assignment will be given at Sec. 3.2. It suffices for a while to notice that phase variable encompasses information about oscillator’s movement from its starting position, as well as its position in a torus, that is, $\theta \bmod 2\pi$. For simplicity, we refer to phase variables using these two interpretations

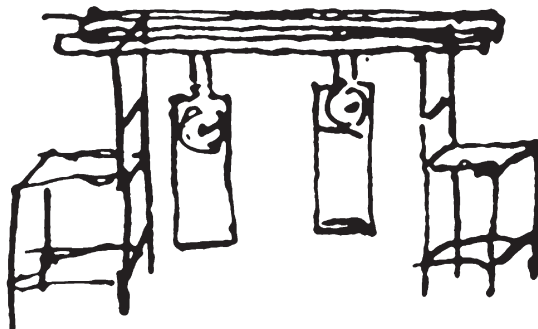


Figure 3.1 - Original drawing of Christiann Huygens illustrating two suspended pendulum clocks. Source: <https://adcs.home.xs4all.nl/Huygens/17/tekenaar.html>

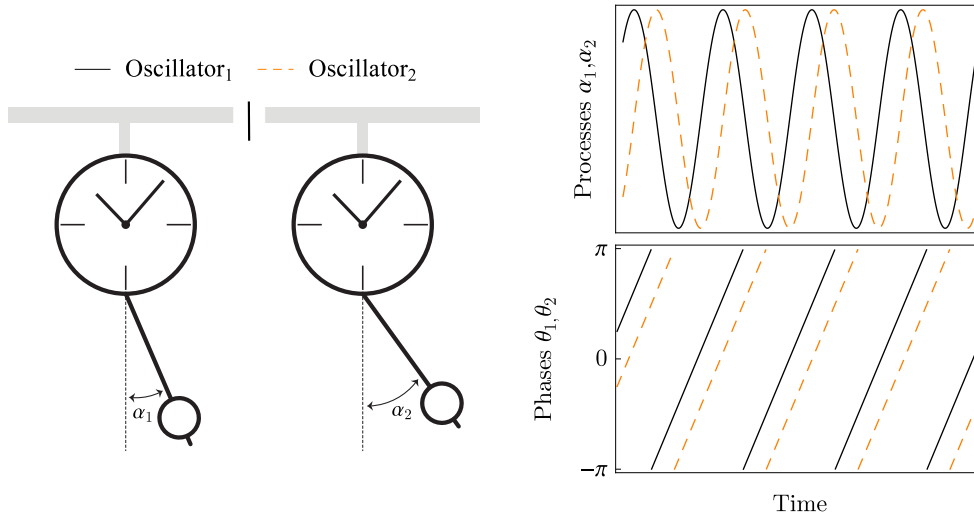


Figure 3.2 - Scheme of two identical isolated pendulum showing processes α_1, α_2 (left side) and phase variables θ_1, θ_2 evolution with time (right side).

without distinction. Variables of each oscillator will be identified by sub indexes and we assume that their periods are the same. Figure 3.2 displays two isolated completely identical pendulums scheme. As they start to oscillate from distinct initial conditions, we observe non-zero constant phase difference over time since there is no influence between them.

Let us now allow these two completely identical pendulums to interact as in Fig. 3.3, via a non-absolute rigid beam like in Huygens observations. They, again, start their movement from different initial conditions. Therefore, the motion of each pendulum can be transmitted through the supporting structure and then to the other one, by means of small bending or vibrations. Even with this weak influence, it may adjust the rhythm and we may obtain *full (phase) synchronization*, where phase difference in the unit circle vanishes with time, that is, $|\theta_1(t) - \theta_2(t)| \rightarrow 0$.

The next step is to assume oscillators with distinct periods T_1, T_2 , due to tiny parameter mismatch in their mechanisms for example. At this context, one no longer expects full synchronization. We might have *phase-locking*, which is a synchronization type where their phase differences converge to a constant value, see Fig. 3.4(a). Another way to characterize this regime is $|\dot{\theta}_1(t) - \dot{\theta}_2(t)| \rightarrow 0$, in other words, oscillators reach the same instantaneous frequency after a transient time¹. If mismatch between oscillator's periods is too high or if the coupling is not strong enough, then

¹At this point of the text we loosely regard transient time as a large enough time for the system dynamics to become close to its long term behavior.

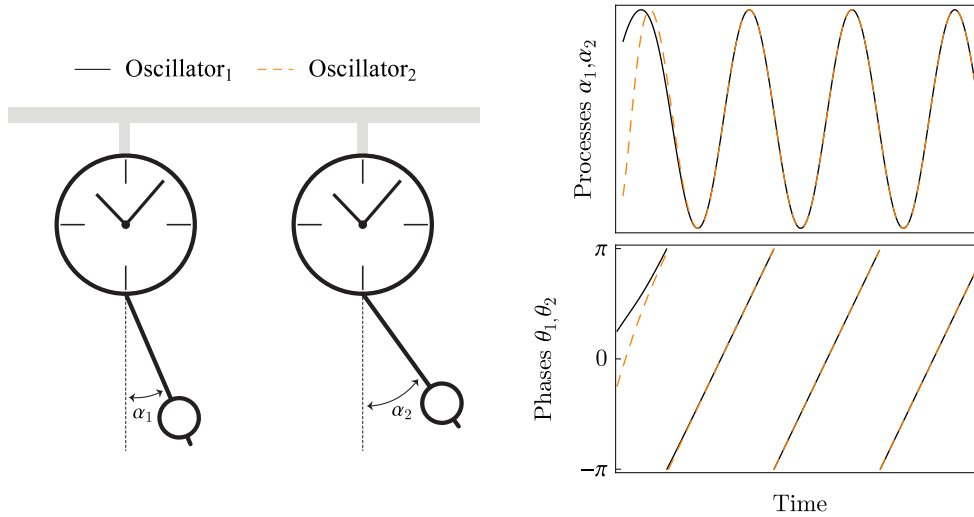


Figure 3.3 - Scheme of two identical coupled pendulum showing processes α_1, α_2 (left side) and phase variables θ_1, θ_2 evolution with time (right side).

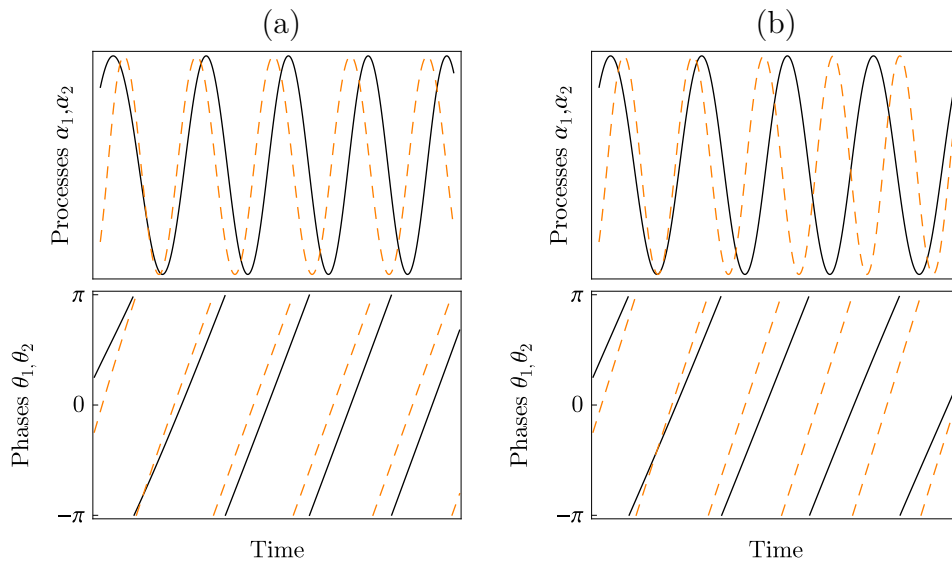


Figure 3.4 - Scheme of two non-identical coupled pendulum showing processes α_1, α_2 and phase variables θ_1, θ_2 evolution with time: (a) phase-locking; (b) asynchronicity.

we have *asynchronicity*, subsystems are affected by each other but they do not come to a “consensus”, see Fig. 3.4(b).

An advantage of such framework is that a large class of oscillators under weak influence can be reduced to phase analysis in a vicinity of its limit set. This topic will be discussed in the next section.

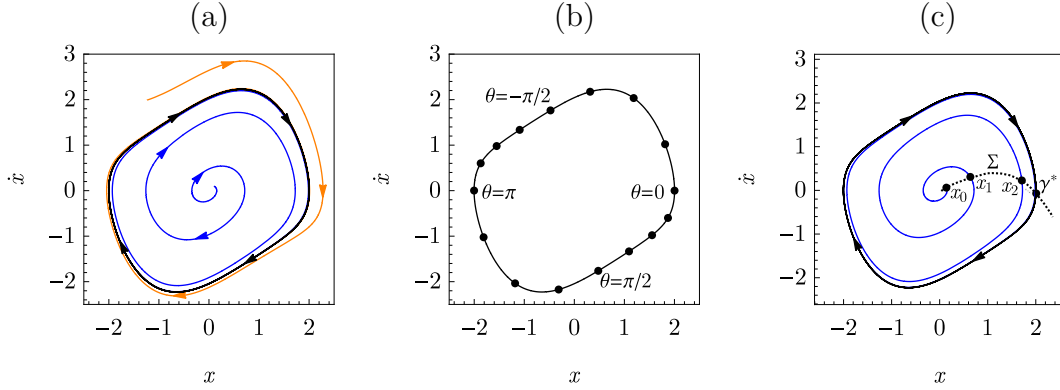


Figure 3.5 - Phase assignment example for van der Pol oscillator with $\mu = 1.5$: (a) Two trajectories (in blue and orange) of (3.2) near its stable periodic solution (in black); (b) Phase variable assignment according to (3.4) along the limit cycle. Black dots mark $\theta = 0, \pi/8, \pi/4, \dots, 2\pi$; (c) Isochrone Σ corresponding to constant phase variable $\theta = 0$.

3.2 Reduction to phase oscillators

We outline here the physical argument from (PIKOVSKY et al., 2003) about conditions for more general oscillators to be approximated by phase oscillators.

Consider a d -dimensional ordinary differential system

$$\dot{x} = f(x), \quad (3.1)$$

containing a limit cycle, that is, a stable periodic solution with period T_0 (HIRSCH et al., 2004). So, in a vicinity of this solution, the trajectory can be regarded as *self-sustained oscillator*. As an example, we mention the popular van der Pol equation

$$\ddot{x} - \mu(1 - x^2)\dot{x} + x = 0 \quad (3.2)$$

for small value of μ (PIKOVSKY et al., 2003), see Fig. 3.5(a).

We introduce phase variable θ to such oscillators as a coordinate along the limit cycle, such that it grows in the direction of the motion and gains 2π after each rotation. In the absence of external forces, phase must be defined assuring uniform growth in time

$$\dot{\theta} = \omega_0, \quad (3.3)$$

where $\omega_0 = 2\pi/T_0$ is called the *natural frequency*.

Eq. (3.3) expresses a key property of oscillators. Perturbations in the direction along the cycle are neutrally stable, which means they neither grow nor decay with time. This reflects the property of autonomous dynamical systems to be invariant under time shifts: if $x(t)$ is a time-dependent solution, then $x(t + \Delta t)$ is a solution, too (PIKOVSKY et al., 2003). Yet, perturbations in transverse directions are attenuated or amplified (in the case of chaotic oscillators), but these behaviors may not be relevant to understand the cyclic process. Chaotic oscillator and the Lyapunov exponent, which is a tool used to study such perturbations, are discussed at Sec. 3.8.

At this point, the reader must be aware that we chose to develop our argumentation based on uniformly growing phase-variables oscillators. Nevertheless, this hypothesis can be too restrictive and in several contexts only *monotonic growth* is required (PIKOVSKY et al., 2003; BALANOV et al., 2010).

Our aim now is to show a possible phase variable construction. More discussion about this topic regarding chaotic oscillators can be found at Chapter 4. Let $\gamma(t)$ be the stable periodic solution of Eq. (3.1) and $\Gamma := \gamma([0, T_0))$. One may assign phase variable through a straightforward bijection between Γ and $[0, 2\pi)$ as

$$\gamma(t) \rightarrow \theta(t) := 2\pi \frac{t}{T_0}, \quad (3.4)$$

so Eq. (3.3) holds. Fig. 3.5(b) illustrates this phase assignment.

Moreover, phase variables in a vicinity $\mathcal{V} \subset \mathbb{R}^m$ of Γ have to be also defined. To do so, we need to define the so-called *isochrones*. Let Φ be the time- T map associated to the flow of Eq. (3.1), that is, $\Phi(x(t)) = x(t + T)$. If \mathcal{V} is sufficiently close to the limit cycle, this mapping has all points on the limit cycle as fixed points, and all points on the vicinity are attracted to it (HIRSCH et al., 2004). Fix a point γ^* on the limit cycle Γ and denote by Σ all the points in the vicinity that are attracted to γ^* under the action of Φ , that is, $x_0 \in \Sigma$ if $\lim_{k \rightarrow \infty} x_k \rightarrow \gamma^*$, where $x_{k+1} = \Phi(x_k)$, see Fig. 3.5(c). We now extend the definition of phase to the vicinity \mathcal{V} , imposing constant phase value along each isochrone Σ . Therefore, every $x \in \mathcal{V}$ crosses Γ in a single point $x_\Gamma(\theta)$ following the corresponding isochrone.

Up to this point, isochrones were introduced to allow phase assignment for self-sustainable limit cycle oscillators. Since we intent to study the interaction between oscillators using phase variables, we need to include the effects of external forces in the system dynamics. We reintroduce Eq. (3.1), adding a perturbation to its vector

field

$$\dot{x} = f(x) + \varepsilon p(x, t) \quad (3.5)$$

where $p(x, t)$ is the external forcing, which is a periodic function on the variable t with period T and forcing natural frequency $\omega = 2\pi/T$ satisfying² $\omega \approx \omega_0$. Besides, we assume $\varepsilon \ll \omega$ meaning fast forcing oscillations and weak coupling, proportional to ε .

In the vicinity \mathcal{V} of Γ , we assign phase variables to solutions of (3.5) and differentiate it

$$\frac{d\theta(x(t))}{dt} = \frac{\partial\theta}{\partial x} \frac{dx}{dt} = \frac{\partial\theta}{\partial x} f(x) + \frac{\partial\theta}{\partial x} \varepsilon p(x, t) = \omega_0 + \varepsilon \frac{\partial\theta}{\partial x} p(x, t). \quad (3.6)$$

The second term on the r.h.s is small (proportional do ε), and the deviations of x from the corresponding $x_\Gamma(\theta)$ at the limit cycle are small too. Thus, we neglect these deviations and compute it at $x_\Gamma(\theta)$ yielding

$$\dot{\theta} = \omega_0 + \varepsilon Q(\theta, t), \quad (3.7)$$

where

$$Q(\theta, t) := \frac{\partial\theta}{\partial x} p(x_\Gamma(\theta), t) \quad (3.8)$$

Note that Q is 2π -periodic in θ and T -periodic in t .

If one represents Q as a double Fourier series we have

$$Q(\theta, t) = \sum_{l,k} a_{l,k} e^{i(k\theta + l\omega t)}. \quad (3.9)$$

Thus, fast oscillating terms lead to deviations of order $\varepsilon \ll \omega$, while resonant terms, satisfying $k\omega_0 + l\omega \approx 0$, can lead to large although slow variations of the phase and are mostly important for the dynamics. So, if we average forcing (3.9) leaving only the resonant terms with $k = -l$, we get $Q(\theta, t) = \sum_k a_{-k,k} e^{ik(\theta - \omega t)} = q(\theta - \omega t)$, where q is a 2π -periodic function. By substitution into (3.7) we have

$$\dot{\theta} = \omega_0 + \varepsilon q(\theta - \omega t). \quad (3.10)$$

If we set now the *phase difference* $\psi := \theta - \omega t$ and introduce $\nu := \omega - \omega_0$ as the

²Actually, even this assumption is not strictly necessary and the details of this generalization can be found at (PIKOVSKY et al., 2003).

dissonance between oscillators, the previous equations reads

$$\dot{\psi} = -\nu + \varepsilon q(\psi). \quad (3.11)$$

Eq. (3.11) reveals a profound characteristic of oscillators near its limit cycle under weak coupling: its dynamics can be described in terms of phase difference ψ , by a vector field parameterized by the dissonance ν , coupling parameter ε and coupling function q .

3.3 A model of mutually coupled oscillators

As an introduction to networks of coupled oscillators, we consider the traditional phase variable model comprising two mutually coupled oscillators

$$\begin{aligned} \dot{\theta}_1 &= \omega_1 + \varepsilon \sin(\theta_2 - \theta_1) \\ \dot{\theta}_2 &= \omega_2 + \varepsilon \sin(\theta_1 - \theta_2) \end{aligned} \quad (3.12)$$

where $\varepsilon \in \mathbb{R}$ is the *coupling gain* or *coupling parameter*, which adjusts the intensity of influence between oscillators; and $\omega_i := 2\pi/T_i$ denotes oscillator's *natural* (or *angular*) *frequencies*. The uncoupled case is characterized by $\varepsilon = 0$, where oscillators travel the torus with constant velocity defined only by their own natural frequency. The *coupling function* consists in the sinus of the phase difference, which reflects two key properties of the interaction between oscillators: (i) \sin is 2π periodic, so influence depends only on oscillator state in the unit circle position, (ii) full synchronization regarding identical oscillator ($\omega_1 = \omega_2$) is a stable regime for any positive coupling, as will be demonstrated in this section.

If we reduce the problem dimension by rewriting Eq. (3.12) in terms of phase difference $\psi := \theta_1 - \theta_2$, we obtain

$$\dot{\psi} = \nu - 2\varepsilon \sin \psi, \quad (3.13)$$

where $\nu := \omega_1 - \omega_2$ is the *dissonance* (or *detuning*) of this system. We assume $\nu \geq 0$, otherwise one can exchange oscillator indexes. Eq. (3.13) is commonly known in the literature as Adler equation, which is the simplest case of Eq. (3.11).

Of course, negative natural frequencies ω_i may not make sense physically. It would be meaningless to say that fireflies are blinking in “reverse direction”. However, we can write $\omega_i = \langle \omega \rangle + \tilde{\omega}_i$, where $\tilde{\omega}_i$ are the deviations of each isolated oscillator from

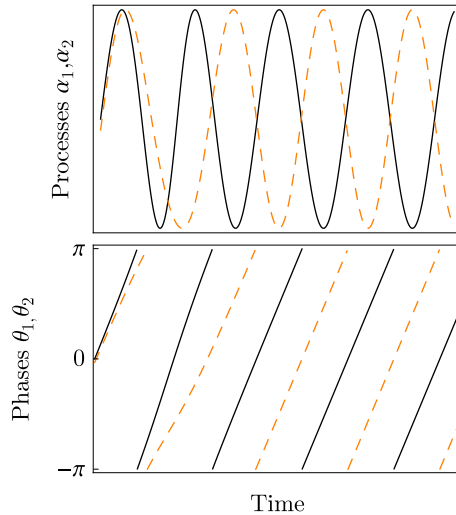


Figure 3.6 - Scheme of two identical coupled pendulum with repulsive coupling $\varepsilon < 0$, showing processes α_1, α_2 and phase variables θ_1, θ_2 evolution with time.

the mean natural frequency $\langle \omega \rangle := (\omega_1 + \omega_2) / 2$. Since only the dissonance between them, $\nu = \langle \omega \rangle + \tilde{\omega}_1 - \langle \omega \rangle - \tilde{\omega}_2 = \tilde{\omega}_1 - \tilde{\omega}_2$, is relevant to analyze this system, we may choose without loss of generality $\langle \omega \rangle = 0$. Another way to interpret this assumption is to consider phase variable $\theta_i(t)$ in a rotating frame with velocity $\langle \omega \rangle$. Also, we associate positive natural frequencies with counterclockwise direction in the unit circle without loss of generality.

One can check that $\psi = 0$ is an equilibrium point of Eq. (3.13) if and only if $\nu = 0$. So, such oscillators can reach full synchronization only if they are identical. Nevertheless, $\sin \psi = 0$ yields $\psi = 0$ or $\psi = \pi$. The stability of these points can be studied via the differential of the right hand side of this equation, which is given by $-2\varepsilon \cos \psi$ (HIRSCH et al., 2004). If $\varepsilon > 0$, $\psi = 0$ is a stable equilibrium point and $\psi = \pi$ is unstable. As a result, positive coupling favors phase difference to vanish and this is why it is called *attractive coupling*. On the other hand if $\varepsilon < 0$, these two equilibrium points exchange roles and we have *repulsive coupling*. Actually, Huygens reported such type of phase-locking synchronization where $|\theta_1(t) - \theta_2(t)| \rightarrow \pi$, which is called in modern terminology as *anti-phase synchronization* as depicted in Fig. 3.6.

Consider without loss of generality $\nu > 0$, otherwise exchange indexes between oscillators. If $\varepsilon \geq 0$, the first equilibrium point arises at $\psi = \pi/2$ when ε equals to the *critical phase-locking value* $\mathbb{L} = \nu/2$. Except at equilibrium point itself, all trajectories converge to it by traveling counterclockwise. In terms of Eq. (3.12),

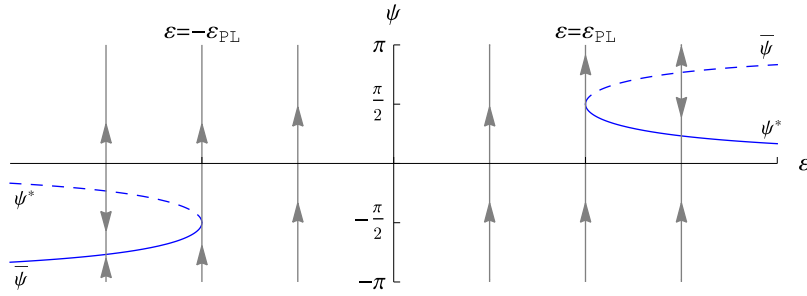


Figure 3.7 - Bifurcation Diagram for the Adler Equation (3.13) with $\nu \geq 0$. The critical coupling parameter for phase-locking is $\varepsilon_{\text{PL}} = \nu/2$. Solid and dashed blue lines correspond respectively to stable and unstable equilibrium points.

it means that oscillators reach phase-locking with the first oscillator a quarter of circle ahead the second one. Also, there is a saddle-node bifurcation at $\varepsilon = \varepsilon_{\text{PL}}$. As ε becomes larger than this critical value, two equilibrium points detach from it: a stable one $\psi^* := \arcsin(\nu/2\varepsilon)$ and an unstable one $\bar{\psi} := \pi - \arcsin(\nu/2\varepsilon)$. The larger the coupling parameter becomes, the closer ψ^* and $\bar{\psi}$ gets to 0 and π , respectively. In other words, oscillators become phase-locked increasingly closer to each other, nearer to full synchronization, as one pushes the coupling parameter ε beyond ε_{PL} . Repulsive coupling $\varepsilon > 0$ yields analogous behavior with stable and unstable equilibrium points exchanging roles, see Fig. 3.7.

The two coupled pendulums is an example of nearly identical oscillators, however this is not the general case. If ε satisfies $0 \ll |\varepsilon| < \varepsilon_{\text{PL}}$, the system is still capable to exhibit weaker synchronization forms apart from phase-locking. To discuss it, Eq. (3.12) will be recast as a gradient system $\dot{\psi} = -\nabla F(\psi)$ with potential field

$$F(\psi) := -\nu\psi - 2\varepsilon \cos \psi. \quad (3.14)$$

Therefore, one can visualize the trajectories of this system as particles sliding down the curve defined by $F(\psi)$, Fig. 3.8(a). We will employ this pictorial explanation to introduce a synchronization diagram over the space-parameter $\nu \times \varepsilon$, see Fig. 3.8(b).

At marks (1,2) from Fig. 3.8(b), we are inside the phase-lock region where $\varepsilon < \varepsilon_{\text{PL}} = \nu/2$, which is known in the literature as first order Arnold Tongue. As one increases the value of ε from (2) to (1), ψ^* becomes closer to 0, which corresponds to phase-synchronization with smaller phase difference (see also Fig. 3.7). In terms of the potential field, there are local minima ψ^* and the particle rests in one of them.

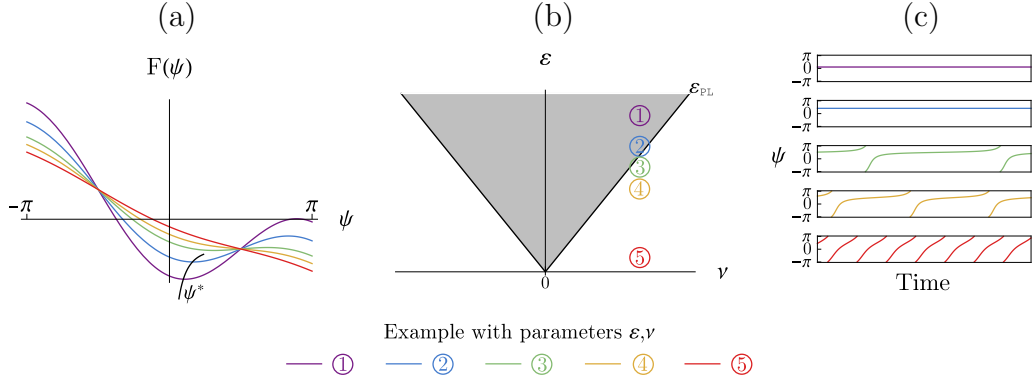


Figure 3.8 - Examples of dynamics with different values of dissonance ν and coupling parameter ε , numbered marks are depicted with unique colors representing different values of ν, ε : (a) Potential field, black corresponds to local minima ψ^* ; (b) Arnold Tongue, phase-locking occurs at the gray area defined by $|\nu| \leq \varepsilon_{\text{PL}} = \nu/2$; (c) Phase difference ψ obtained after transient time.

Mark (3) lays right after the boundary of this region. Instead of local minima, we have a slightly tilted plateau and steep slopes. Thus, we observe long epochs where phase difference varies slowly intermingled with abrupt spins of one oscillator related to the other. This intermittent phase-locking synchronization regime is known as *phase-slips*. At Mark (4), further away from the Arnold Tongue boundary, the intervals of time with almost constant phase difference become shorter.

If the coupling parameters is too small related to the dissonance, like at Mark (5), the potential field becomes close to a tilted plane. We say that there is *no synchronization* since phase difference grows almost uniformly.

3.4 Kuramoto model

When one considers ensembles of coupled oscillators, the pioneer model regarding N mutually coupled non-identical oscillators introduced by Kuramoto is probably the most celebrated choice. Beyond the fact that it corresponds to an approximation of a large class of weakly coupled oscillators (see Ref. (PIKOVSKY et al., 2003) and Sec. 3.2), the Kuramoto Model (KM) belongs to the core of Winfree’s classical study about biological rhythms (WINFREE, 1967) and applications like pattern recognition (FOLLMANN et al., 2015), power grid analysis (FILATRELLA et al., 2008; GRZYBOWSKI et al., 2016) and community detection in networks (XIE et al., 2013; QUILES et al., 2016). The state of art related to this model can be found for instance at (RODRIGUES et al., 2016) .

We focus in a version of this model where the channels of influence are defined by a *coupling graph* \mathcal{G} according to the following ordinary equation³

$$\dot{\theta}_i = \omega_i + \frac{\varepsilon}{d_i} \sum_{j=1}^N A_{ij} \sin(\theta_j - \theta_i), \quad (3.15)$$

for $i = 1, \dots, N$, where $\omega = (\omega_1, \dots, \omega_n) \in \mathbb{R}^N$ are the oscillator's *natural frequencies* and ε is the *coupling parameter* as in the previous section. The graph \mathcal{G} is expressed by its adjacency $N \times N$ matrix A . The i -th oscillator is affected by the j -th one if $A_{ij} = 1$; and $A_{ij} = 0$ otherwise. We consider the coupling graph to be simple, that is, $A_{ij} = A_{ji}$ and $A_{ii} = 0$ for all $i, j = 1, \dots, N$. Besides, \mathcal{G} is assumed without loss of generality to be connected.

At this version of the KM, the coupling parameter is divided by corresponding vertex degree, $d_i := \sum_{j=1}^N A_{ij}$. It yields *local mean field* coupling model, because if we define the complex number

$$Z_i e^{i\bar{\theta}_i} := \sum_{j=1}^N A_{ij} e^{i\theta_j}, \quad (3.16)$$

then $\bar{\theta}_i \in [0, 2\pi)$ regards the average of neighbor oscillator's phases and $Z_i \in [0, d_i]$ increases with this neighborhood cohesion. Therefore, Eq. (3.15) reads

$$\dot{\theta}_i = \omega_i + \frac{\varepsilon}{d_i} Z_i \sin(\bar{\theta}_i - \theta_i). \quad (3.17)$$

Therefore, each oscillator is affected by the mean neighborhood phase and this influence is intensified with neighborhood cohesion. This interpretation of the KM emphasizes its relation with diffusion phenomena, like epidemic (HIRSCH et al., 2004) and percolation models (CALLAWAY et al., 2000).

The quantifier Z_i can be regarded as *local order parameter* or *local mean field*⁴. The reader can notice that: (1) full synchronization $R = 1$ is equivalent to $Z_1/d_1 = \dots = Z_N/d_N = 1$; (2) splay synchronization $R = 0$ is not equivalent to $Z_1/d_1 = \dots = Z_N/d_N = 0$, unless A is the all-to-all graph.

In order to quantify consensus, classic synchronization measures are included in the next section.

³There are also versions of the KM model for discrete time and higher order $\ddot{\theta}_i$ equations (PIKOVSKY et al., 2003).

⁴An alternative version of the KM with non-linear coupling based on this Z_i will be introduced in Chap. 5.

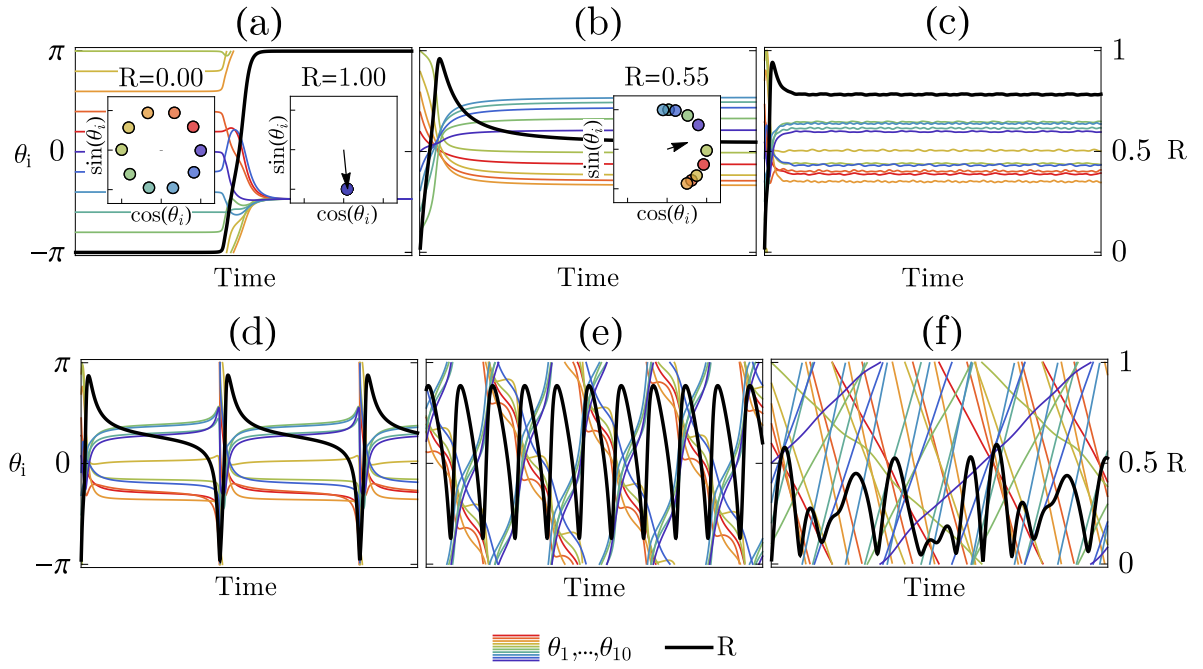


Figure 3.9 - Phase variables θ_i and order parameter R evolution with time for typical synchronization types: (a) Phase-locking (partial synchronization index $S = 1$) showing splay to full synchronization; (b) Phase-locking ($S = 1$) with $\langle R \rangle = 0.55$; (c) Practical phase-locking ($S = 0.98$) with $\langle R \rangle = 0.88$; (d) Phase Slips ($S = 0.95$) with $\langle R \rangle = 0.62$; (e) Periodic Order Parameter ($S = 0.78$) with $\langle R \rangle = 0.52$; (f) Asynchronicity ($S = 0.09$) with $\langle R \rangle = 0.27$. Phase variable representation in the unit circle are included as inset in subfigures (a,b) with an arrow indicating the global mean field.

3.5 Synchronization Metrics

The most used synchronization metric in the literature is the *global mean field*. It regards Eq. (3.16) taking into account all oscillators in the networks

$$Re^{i\Theta} := \frac{1}{N} \sum_{j=1}^N e^{i\theta_j}, \quad (3.18)$$

where Θ is the argument of this complex number and $R \in [0, 1]$ is its magnitude, called the *order parameter*. If one has $R = 0$, it means *splay synchronization* (PALEY et al., 2005). The sum of neighbor's contribution $e^{i\theta_j}$ cancel out, for instance if all oscillators are uniformly spread around the unit circle. On the other hand, *full synchronization* $\theta_1 = \dots = \theta_N$, implies $R = 1$. Fig. 3.9(a) provides an example evolving from $R = 0$ to $R = 1$.

Phase-locking occurs when the instantaneous velocity $\dot{\theta}_i$ of all oscillators converge to

a common value, irrespective to the phase shift between them. The whole ensemble travels the unit circle as a rigid body. So, the order parameter as a function of the time $R(t) := R(\theta(t))$ converges to a constant value $c \in [0, 1]$, not necessarily in splay or full synchronization, like in Fig. 3.9(b).

Fig. 3.9(c) illustrates a not convergent $R(t)$. However, it presents small fluctuations around a constant value. This type of synchronization can be called *practical phase-locking*⁵. So, it is useful to define $\langle R \rangle$ as the average value of order parameter in a large interval of time permanent regime.

To quantify phase-lock emergence, we introduce the partial synchronization index $S \in [0, 1]$ (GÓMEZ-GARDEÑES et al., 2007) based on a synchronization quantifier between oscillator pairs i, j

$$S_{ij} = S_{ji} := \left| \lim_{\Delta t \rightarrow \infty} \frac{1}{\Delta t} \int_{t_r}^{t_r + \Delta t} e^{i(\theta_i(t) - \theta_j(t))} dt \right|, \quad (3.19)$$

where t_r is a large enough transient time. It is straightforward to check that these oscillators are phase-locked, if and only if $S_{ij} = 1$. Moreover, if S_{ij} is decreased towards zero, then weaker forms of synchronization and later uncorrelated trajectories occur (FREITAS et al., 2013). We average contributions of all adjacent oscillators in the network to define the *partial synchronization index*

$$S := \frac{1}{M} \sum_{i,j=1}^N A_{ij} S_{ij}, \quad (3.20)$$

where M is the quantity of directed edges in the graph. Thus, $S = 1$ means that the whole ensemble is phase-locked. If $1 > S \gg 0$, weaker ensemble synchronization forms can be found. Fig. 3.9(d) shows phase slips. There is regular collective dynamics alternating between long periods of slow deviations from phase-locking and abrupt settlements to the previous behavior Fig. 3.9(e) does not exhibit phase slips, but its order parameter also became a periodic function.

Finally, $S \ll 1$ yields very low coherence as shown in Fig. 3.9(f).

The mean value of $R(\theta(t))$ after the transient is denoted by $\langle R \rangle$. For a given choice of parameters and initial conditions, we indicate by ε_{PL} the smallest critical coupling strength $\varepsilon > 0$ inducing phase-locking, i.e. $S = 1$ and $R(\theta(t))$ converges to a constant value, which we denote by R_{PL} .

⁵This case is commonly associated with phase-locking under the influence of noise

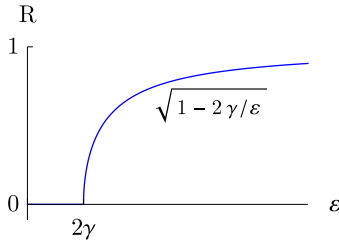


Figure 3.10 - Order parameter R as a function of coupling parameter ε for the KM (3.15). All-to-all coupling in the thermodynamic limit $N \rightarrow \infty$ with natural frequencies chosen from a Lorentzian distribution with parameter γ are considered (KURAMOTO, 1975).

3.6 Two classic results of phase oscillators networks

Kuramoto introduced in 1975 (KURAMOTO, 1975) his homonymous model regarding Eq. (3.15) with all-to-all coupling. It means that oscillators are subjected to a feedback comprising a common pool of all members in the system. Besides, considered natural frequencies were chosen from a Lorentzian distribution, which is a symmetrical and unimodal distribution, parameterized by a constant value γ defining its width.

By assuming network size in the thermodynamic limit $N \rightarrow \infty$, he was able to prove that if one increases the coupling parameter, the order parameter rises from zero at $\varepsilon = 2\gamma$ and then asymptotically approaches to 1 according to $R = \sqrt{1 - 2\gamma/\varepsilon}$, see Fig. 3.10.

Therefore, like in the $N = 2$ case discussed in Sec. 3.3, there is a critical coupling parameter ε from which R start to increase monotonically with ε .

The authors of Ref. (JADBABAIE et al., 2004) considered arbitrary network sizes and coupling strength divided by N instead of the node degree d_i in Eq. (3.15). They required the coupling graph to be simple and connected and assumed without loss of generality natural frequencies ω with zero-mean⁶. Therefore, the Euclidean norm of ω , which we denote by $\|\omega\|$, measures the dispersion of natural frequencies like the dissonance ν for the two-dimensional case or the Lorentzian parameter γ in the previous $N \rightarrow \infty$ case.

In this context, their analytic results (JADBABAIE et al., 2004) give bounds to phase-locking critical coupling and guarantee convergence to a unique (modulus 2π) stable

⁶To do so, one can rewrite the system in a rotating frame like in Sec. 3.3

phase-locked regime, irrespective to initial conditions. If all oscillators are identical, that is, $\|\omega\| = 0$, any attractive (repulsive) coupling value $\varepsilon > 0$ ($\varepsilon < 0$) yields full (splay) synchronization. In general, phase-locking occurs if the coupling strength ε is large enough in comparison to $\|\omega\| \lambda_N / \lambda_2^2$, where λ_2, λ_N are Laplacian eigenvalues of the coupling graph (see Sec. 2.2). So, phase-locking tends to emerge for smaller values coupling values of $\varepsilon > 0$ mostly with the reduction of graph diameter D , for instance in scale-free and small world networks, but with smaller values of $\|\omega\|$ and d_{\max} too⁷.

3.7 Notes about Kuramoto Model Numerical Integration

Numerical integration of large coupled oscillator networks can demand high computational effort. Some observations are included in this section to mitigate the cost of this task.

The first straightforward fact is that, although it can be interesting to express the KM in terms of the adjacency matrix due to its mathematical properties, one could write it in terms of its adjacency list, that is, replacing $\sum_{j=1}^N A_{ij} \sin(\theta_i - \theta_j)$ in Eq. (3.15) by $\sum_{j \in \mathcal{N}_i} \sin(\theta_i - \theta_j)$, where \mathcal{N}_i denotes the set of adjacent vertexes to i in the coupling graph. In addition, whenever we have an odd coupling functions, like sinus, we can store the values of $c_{ij} := \sin(\theta_i - \theta_j)$ for $i < j \leq N$ and set $\sin(\theta_j - \theta_i) \leftarrow -c_{ij}$. So, we may loop only over the undirected edges of the graph \tilde{E} only to evaluate phase differences.

About the numerical integration method itself, predictor-corrector techniques are specially interesting, like Adams-Bashforth-Moulton (ABM) (BURDEN; FAIRES, 2005), since they require only one vector field evaluation per time step. For comparison, the fourth order Runge-Kutta (4RK) requires 4 evaluations⁸. Another advantage of ABM is that it can be easily adapted to integrate delayed differential equations with constant delay time (WIRKUS, 1999), which is another see Sec. 3.9.

The size of the integration interval $[0, t_f]$ is a practical issue too. To analyze permanent regime, one needs t_f to be sufficiently large. Yet, t_f has to be small enough to make massive simulations feasible. One way to balance these conflicting demands is to define a partial synchronization index in the interval $I := [a, b]$, denoted by S_I ,

⁷In general, λ_2 increases when the graph diameter is decreased and λ_N decreases with its maximum degree d_{\max} (LI; ZHANG, 1998).

⁸On the other hand, ABM requires the storage of the vector field in 4 instants of time, while 4RK does not need it; but this is normally not a restriction for simulation purposes.

like in (3.20), replacing $S_{i,j}$ by an approximation of it over this interval, that is,

$$S_{ij}(I) := \left| \frac{1}{b-a} \int_a^b e^{i(\theta_i(t) - \theta_j(t))} dt \right|. \quad (3.21)$$

So, we compute this metric over successive time intervals $S_{I_0}, S_{I_1}, \dots, S_{I_k}, \dots$, with interrupt criterion $|S_{I_k} - S_{I_{k-1}}| < \text{tol}$ and $k > 1$. This way, the final S_{I_k} is an approximation to S and I_k can be considered beyond transient time, in terms of partial synchronization index convergence.

Unless explicitly stated, we employ the procedures explained in this section for all numerical simulations in this thesis, with time intervals of 10^3 u.t. and $\text{tol} = 0.01$.

3.8 Chaotic oscillators and Lyapunov exponents

Not only trajectories near limit cycle can be regarded as oscillators. Chaotic oscillators regards trajectories close to chaotic attractors (HIRSCH et al., 2004) which are employed in a several fields (STROGATZ, 2014).

One of the first members of this class of oscillators is the Lorenz system (PIKOVSKY et al., 2003), which was introduced in 1963 as a simplified mathematical model for atmospheric convection. It consists in a three-dimensional ordinary differential system following

$$\begin{aligned} \dot{x} &= \sigma(y - x) \\ \dot{y} &= x(\rho - z) - y \\ \dot{z} &= xy - \beta z, \end{aligned} \quad (3.22)$$

where $\sigma = 10$, $\rho = 28$ and $\beta = 8/3$ are the common parameters found in the literature yielding chaos. Fig. 3.11(a) depicts a trajectory of (3.22) showing its well known butterfly-like attractor.

Such systems have high sensibility to initial conditions, meaning that even very small positive deviation from initial condition can produce unrelated trajectories after a relative short time. For instance, Fig. 3.11(b) shows two trajectories of (3.22) becoming uncorrelated after approximately 10 units of times.

If one defines $v = \sqrt{x^2 + y^2}$, the projection into coordinates (v, z) of Lorenz system trajectories shows a clear rotation center as in Fig. 3.11(c). So, this coordinate change reveals that some chaotic attractors can be seen as smeared limit cycle (recall Fig. 3.5(a)). However, such transformation may not exist for chaotic oscillators in general

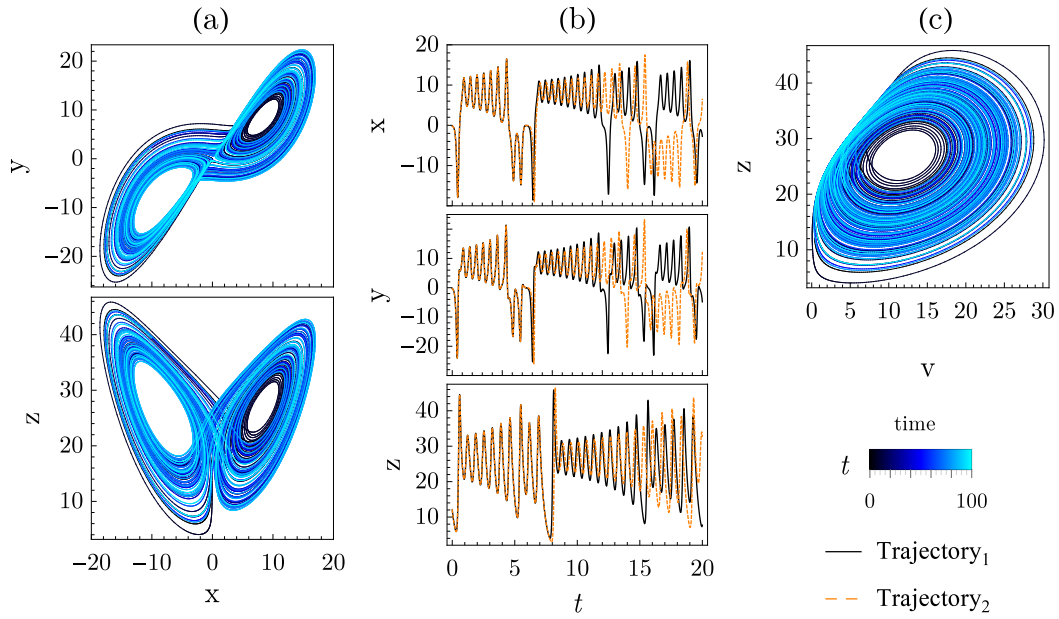


Figure 3.11 - (a) Lorenz system trajectories: (a) (x, y) and (x, z) projections of one trajectory with time color coding from 0 (Black) to 100 units of time (Cyan); (b) x, y, z components regarding two different trajectories (black and dashed/orange) with initial conditions 0.001 apart from each other; (c) Another projection, as in the first case, in coordinates (v, z) where v is the transformation change $v = \sqrt{x^2 + y^2}$.

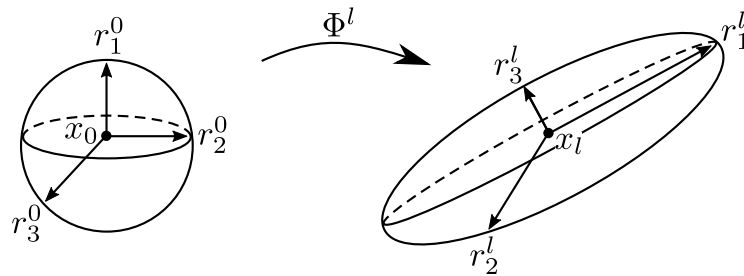


Figure 3.12 - Illustration of l iterations of time shift map Φ employed at Lyapunov exponents definition.

and we require another way to properly characterize them.

Lyapunov exponents (ALLIGOOD et al., 1997) are a mathematical tool to quantify the rate of separation of infinitesimally close trajectories. Let $\dot{x} = f(x)$ be a M dimensional system, while $\Phi(x_0)$ denotes the δ time shift map, that is, the solution of the ordinary differential equation after δ units of time, for a fixed positive constant value δ , with initial condition x_0 . We denote l successive map compositions by Φ^l , that is, $\Phi^l = \Phi \circ \Phi^{l-1}$, with $\Phi^1 = \Phi$.

Lyapunov exponents keep track of deformations suffered by a hypersphere $S \in \mathbb{R}^M$ through Φ^l , in the limit $l \rightarrow \infty$. Details about its numerical computation using variational equations can be found at (WOLF et al., 1985). We focus on the interpretation of these quantifiers here.

Let $\mathcal{S}^0 = \{r_1^0, \dots, r_M^0\}$ be an orthonormal basis of \mathbb{R}^M at x_0 . Then, we set $S^l = \Phi(S^{l-1}) = \{r_1^l, \dots, r_M^l\}$ and sort $r_1^l \geq \dots \geq r_M^l$ at each iteration of Φ . Therefore, S^l measures the contraction or expansion near the orbit x_0 during the first l iterations. The k -th largest Lyapunov exponent of x_0 is defined by

$$\lambda_k(x_0) = \ln \lim_{l \rightarrow \infty} (r_k^l)^{1/l} \quad (3.23)$$

if this limit exists. Moreover, we assume systems to be *ergodic*, meaning that they have the same behavior averaged over time as averaged over the space of all the system's states, so λ_k does not depend on the particular initial condition x_0 (HOOVER; HOOVER, 2012).

From Eq. (3.23), we conclude that if there is a direction which remains neutral relative to perturbation, where $\lim_{l \rightarrow \infty} r_k^l \rightarrow 1$, then $\lambda_k = 0$. If there are directions where perturbations are attenuated (amplified), we have negative (positive) Lyapunov exponent.

As a result, one way to characterize (PIKOVSKY et al., 2003) chaotic oscillators is the existence of at one zero, and at least one negative and one positive Lyapunov exponents λ . Perturbations along the trajectory neither grow nor decay, yielding $\lambda = 0$ in that direction; while perturbations transverse to the attractor are attenuated with time, since all solutions in a vicinity approach to it, yielding $\lambda < 0$.

Zero and negative Lyapunov exponents are also present in stable limit cycle dynamics as in Sec. 3.2. However, only chaotic oscillators have positive Lyapunov exponents, due to its sensibility to initial conditions. These Lyapunov exponents correspond to perturbations tangent to the attractor but orthogonal to its trajectories.

There are studies exploring ways to build optimal phase description of chaotic oscillations by generalizing the concept of isochrones (SCHWABEDAL et al., 2012). More discussion about phase variables and chaotic oscillator can be found at Chap. 5.

3.9 Some generalizations of coupled oscillators networks

Networks of phase oscillators are commonly modeled as the KM in Eq. (3.15), but phase reduction may not always be the best model choice, for instance, if signal amplitude, not only its phase, deeply influences dynamics. Thus, we present in this section a more general version of coupled oscillator networks to support discussions in the next chapters.

Chaotic or limit cycle oscillators in its original variables, as well as phase variables oscillators can be addressed in a common basis. Moreover, this formulation is also suitable for some non-self-sustainable oscillators, like integrate-and-fire models for neuron action potential (PIKOVSKY et al., 2003).

Consider an ensemble of N oscillators, whose dynamics of the i -th oscillator is given by

$$\frac{dx_i(t)}{dt} = f_i(x_i(t)) + \varepsilon \sum_{j=1}^N \mathcal{A}_{ij} H(x_j(t - \tau) - x_i(t)), \quad (3.24)$$

for $i = 1, \dots, N$, where $x_i(t) \in \mathbb{R}^d$ is the oscillator state at instant t , while its isolated behavior is defined by $f_i(\cdot)$, like in Eq. (3.1). This function may express natural frequency ω_i , in the case of phase oscillators, or even more sophisticated dynamics, like the r.h.s. of van der Pol or Lorenz systems (Eqs. (3.2) and (3.22)). If oscillators are identical, then $f_1 = \dots = f_N := f$.

The coupling parameter is still denoted by $\varepsilon \in \mathbb{R}$, tuning over all neighbor oscillators influence. However, the coupling graph is allowed to be weighted, meaning that oscillators can be affected each other unevenly with intensity proportional to ε times $\mathcal{A}_{ij} \in \mathbb{R}$. We also mention time varying or directed edges coupling graphs as other variations, where influence channels depend on the relative spacial position among agents (PALEY et al., 2005; LEONARD et al., 2007; VICSEK; ZAFEIRIS, 2012).

As the sinus function in the KM (3.15), $H(\cdot)$ corresponds to the coupling function. This function is *diffusive*, since it regards the state difference between oscillators. H is often assumed to be a $d \times d$ real matrix in the context of non-phase oscillators. As a simple example, a network of Lorenz oscillators with $H = \begin{pmatrix} 0 & 0 & 0 \\ 0 & 1 & 0 \\ 0 & 0 & 0 \end{pmatrix}$ indicates linear coupling by y coordinate.

The difference between states is considered at the same instant t if τ , which is the *time delay parameter*, equals to zero. However, propagation through communication channels may not be instantaneous, requiring τ units of time for the signal to

reach neighbors. Thus, oscillators are actually affected by $x_j(t - \tau)$. Among such scenarios, we have networks of semiconductors lasers (SORIANO et al., 2013) and large scale sensors networks (HONG; SCAGLIONE, 2005). When $\tau > 0$, instead of an ordinary equation, Eq. (3.24) becomes a delayed differential equation. This class of systems requires not only the initial condition $X(t)$ at $t = 0$, but also for the entire range $t \in [-\tau, 0]$, demanding special methods for numeric integration (BAKER, 2000; GRZYBOWSKI et al., 2011; EISENCRAFT et al., 2012).

We highlight that even at this context, where system dynamics is not reduced to phase variables, phase assignment to time series is often a valuable tool to study synchronization (PIKOVSKY et al., 2003) as discussed in the next chapter.

4 THE DOUBLE STRIP TEST BED FOR PHASE ASSIGNMENT METHODS

In the context of coupled oscillators, one may directly compute the norm of the differences between oscillator's states over time, without any phase assignment. If this value becomes sufficiently small after the transient, it indicates a regime close to full synchronization, when oscillators converge to a common trajectory.

However, several synchronization qualitative regimes commonly found in experiments (ROSENBLUM *et al.*, 2004) can only be characterized by phase assignment. According to (PIKOVSKY *et al.*, 2003), there seems to be no rigorous way to solve this problem for arbitrary chaotic systems. Thus, how do we compare phase assignment methods?

For this purpose, we present in this chapter the Double Strip Test Bed (DSTB), which is a methodology to construct time series similar to the ones originated from chaotic oscillators. This approach relies on a Kuramoto Model (KM), from Eq. (3.15), and a transformation of its phase variables by embedding them into a three dimensional surface, in such a way to obtain curves with phase variables are known a priori.

The DSTB has already been introduced at our paper (FERREIRA *et al.*, 2015), see Appendix A. Yet at this reference and also at the thesis (FERREIRA, 2014), phase assignment methods based on Continuous or Discrete Complex Wavelet and Hilbert Transformation were explored.

We focus here on the main ideas and some background concepts not included in those previous works about the DSTB¹.

We provide in the first session a short overview about the phase assignment problem for chaotic oscillator. Then, the DSTB is described at the second session like in (FERREIRA *et al.*, 2015). In the last section, we included an usage example of the DSTB with common phase assignments methods from the literature, as well as conclusions.

¹Other two embedding were introduced at (FERREIRA *et al.*, 2015), into a $2d$ circle and into a $3d$ Möbius Band. We show only the DSTB because it emulates more chaotic properties.

4.1 Phase assignment for chaotic oscillators

One of the properties of chaotic systems is that unstable periodic orbit are dense on its attractor (HIRSCH et al., 2004). Besides, contrary to limit cycle oscillators, it may be not straightforward to define monotonic growing phase variables. Uniform growth, like Eq. (3.3), with a global choice of natural frequency ω_0 in a neighborhood of the attractor (PIKOVSKY et al., 2003), is more restrictive yet or even impossible.

Under mild assumptions (PIKOVSKY et al., 2003), a uniformly rotating phase $\theta(t)$ can be constructed if one already has monotonic growing variable $\phi(t)$. This is done through the following time rescaling

$$\theta = \omega_0 \int_0^\phi \left(\frac{d\phi}{dt} \right)^{-1} d\phi. \quad (4.1)$$

However, this approach may not be applicable for oscillator ensembles, since it would imply different time rescaling for each network. Even so, any choice of phase must at least have a physical meaning and correctly count oscillator cycles (PIKOVSKY et al., 2003).

We focus now on classic numeric phase assignment methods, which will be introduced along with the uncoupled Rössler oscillator

$$\begin{aligned} \dot{x} &= -y - z \\ \dot{y} &= x + ay \\ \dot{z} &= 0.1 + z(x - 8.5). \end{aligned} \quad (4.2)$$

This system was chosen because it is a prototypic model for two flavors of attractors: *coherent*, where $a = 0.16$; and *non-coherent*, $a = 0.25$ (CHEN et al., 2001). By coherent attractors, we mean oscillators showing a clear rotation center regarding a projection over a pair of its coordinates, like in Fig. 4.1(a). This chaotic oscillators class resembles a smeared version of limit cycle oscillators. Otherwise, we say that an attractor is non-coherent, as in Fig. 4.1(d). In this case, the main cycle occurs in the x, y plane with $z \approx 0$ (cyan), even though a portion of its trajectory is bended like a funnel (blue).

A *Poincaré surface* is a section which is crossed transversely by trajectories of the system (HIRSCH et al., 2004). The halfplane $y = 0, x < 0$ will be taken as Poincaré surface for both versions of the Rössler system, see Fig. 4.1(a,d).

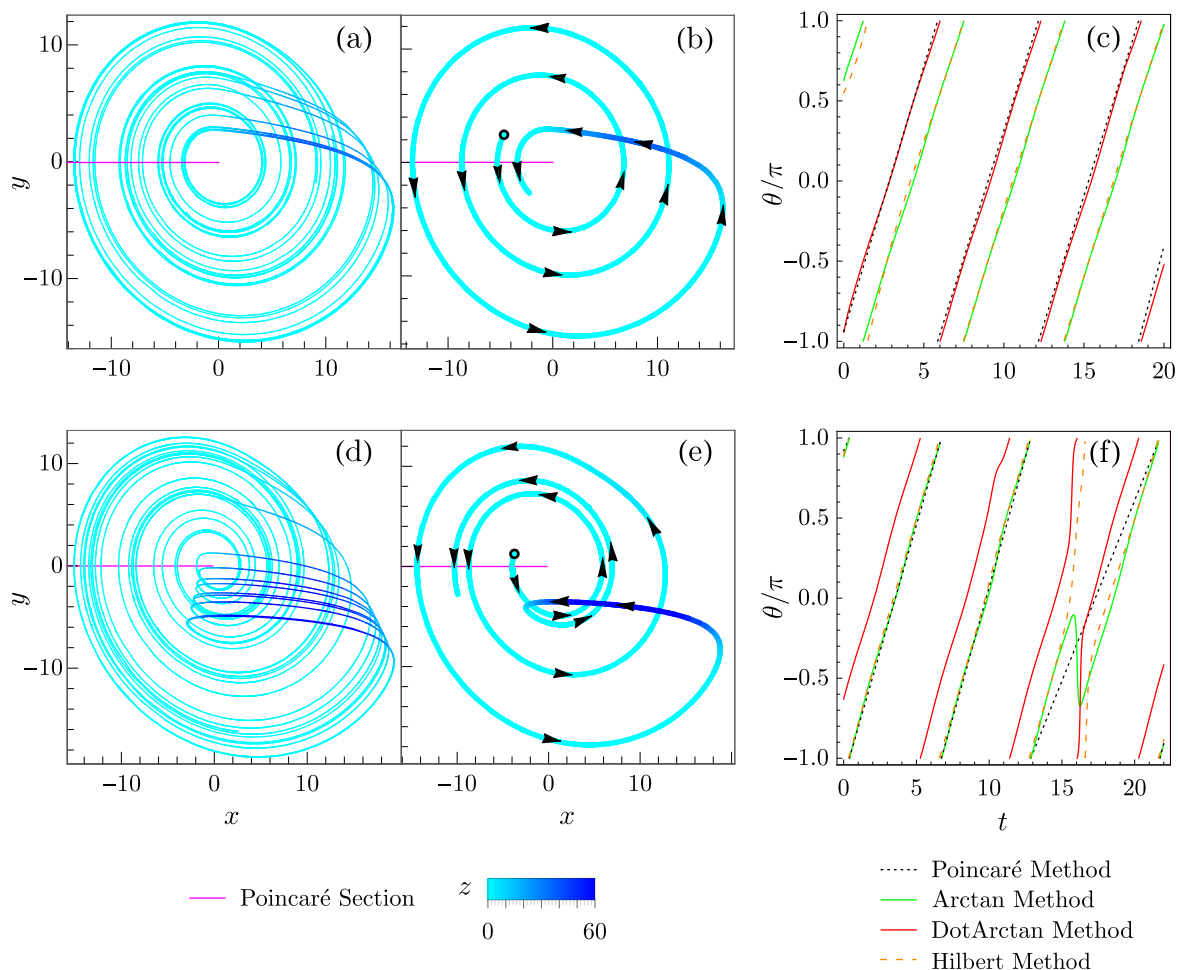


Figure 4.1 - Rössler oscillator as in Eq. (4.2). Upper figures correspond to the coherent version and bottom figures to the non-coherent one: (a,d) x, y projection of a trajectory during 200u.t., color code ranges from cyan to blue as z increases from zero to 60; (b,e) approximately 3 cycles of the previous trajectory. The Poincaré section ($y = 0, x < 0$) is shown in magenta. (c,f) Phase assignment via four methods.

If such surface exists, for each piece of a trajectory between two cross-sections, the *Poincaré method (for phase assignment)* defines phase as a linear function of time, so that phase gains 2π at each return to the surface of section:

$$\theta(t) = 2\pi \frac{t - t_n}{t_{n+1} - t_n} + 2\pi n, \quad (4.3)$$

where t_n is the time of the n -th crossing the surface. The reader must be aware that Poincaré surfaces may not exist or can be difficult to define depending on the attractor form.

As another option, one can assign coordinates via the *Arctan method* in the coherent case. This is done by selecting two coordinates, denoted by simplicity by (x, y) , such that system trajectories restricted to them perform approximately a circle centered at some $(x_0, y_0) \in \mathbb{R}$. In fact, (x, y) can be built through coordinate transformation like in Fig. 3.11(c). Then, we set

$$\theta(t) = \arctan \frac{y(t) - y_0}{x(t) - x_0}, \quad (4.4)$$

which is normally computed as a 2 parameters function $\arctan(y - y_0, x - x_0)$ regarding the argument of the complex number $x - x_0 + i(y - y_0)$.

Even if the attractor is non-coherent and there is no coordinate transformation satisfying the previous requirements, one can try a generalization provided by (CHEN et al., 2001), that we address as *DotArctan method*. This is done by considering the derivative of a pair of coordinates $(\dot{x}, \dot{y}) = \left(\frac{dx}{dt}, \frac{dy}{dt}\right)$, thus

$$\theta(t) = \arctan \frac{\dot{y}(t)}{\dot{x}(t)}. \quad (4.5)$$

Finally, the *Hilbert method* (PIKOVSKY et al., 2003) for a signal $s(t)$ is defined as

$$A(t) e^{i\theta(t)} := s(t) + i s_H(t), \quad (4.6)$$

where $s_H(t)$ is the Hilbert Transform of s . Then, $A(t)$ and $\theta(t)$ correspond to the amplitude and phase of $s(t)$. This technique is largely applied to analyze experimental data, because it requires the time series of single coordinate of the phenomena.

We apply now these four phase assignment methods to the coherent and non-coherent trajectories illustrated in Fig. 4.1(b,e), respectively. We selected in both

figures intervals of time corresponding to approximately three complete cycles taking as reference the Poincaré Section.

Fig. 4.1(c) shows that all methods agree with each other for the coherent case. The constant value differences between methods does not significant role, due the existence of the to neutral Lyapunov exponent.

However, the non-coherent case presents complications at the third cycle, when the trajectory goes through the funnel region (blue). The Arctan method yields poor results, since there is an interval where its outcome is a decreasing function, without physical meaning. In contradistinction, the DotArctan and Hilbert methods produce non-decreasing phases, but they count four cycles instead of three. Although the Poincaré method does not allow fine tracking of local phase changes due to linear its interpolation, it was the only one to report the 3 cycles.

In summary, this example shows conflicting results depending on the methodology applied. Merely analyzing a 2d projection of the time series within a time interval as in Fig. 4.1(e), one could argue that if we had chosen S' as Poincaré Section, it would display four cycles as well. Typically, this type of issue can only be answered by investigating more dimensions of the phenomena, which may not be available concerning time series from experimental data.

To tackle this question in our context, Fig 4.2 is presented with additional views of the three dimensional attractor. We recorded the local minima in x satisfying $y < 0$ and $z > 0.1$ than zero, over 500u.t. of the trajectory. Portions of this curve crossing the Poincaré Surface up to such points are colored in cyan.

Therefore, cycles through this cyan ribbon, including the one depict the third cycle in Fig 4.1(e), display sub-cycles in the x, y plane with $y < 0$.

4.1.1 About accuracy techniques for phase assignment methods

The previous section showed that the choice of phase assignments methods is not always straightforward. Poincaré, Arctan and DotArctan, require the time series of at least two dimensions of the phenomenon. Hilbert method is more effective to deal with data containing observational noise, even so low-frequency trends remains a major challenge (FERREIRA, 2014).

How does one probe the accuracy of a candidate to phase assignment method? Typically, a prototypical oscillator is chosen, like the coherent and non-coherent

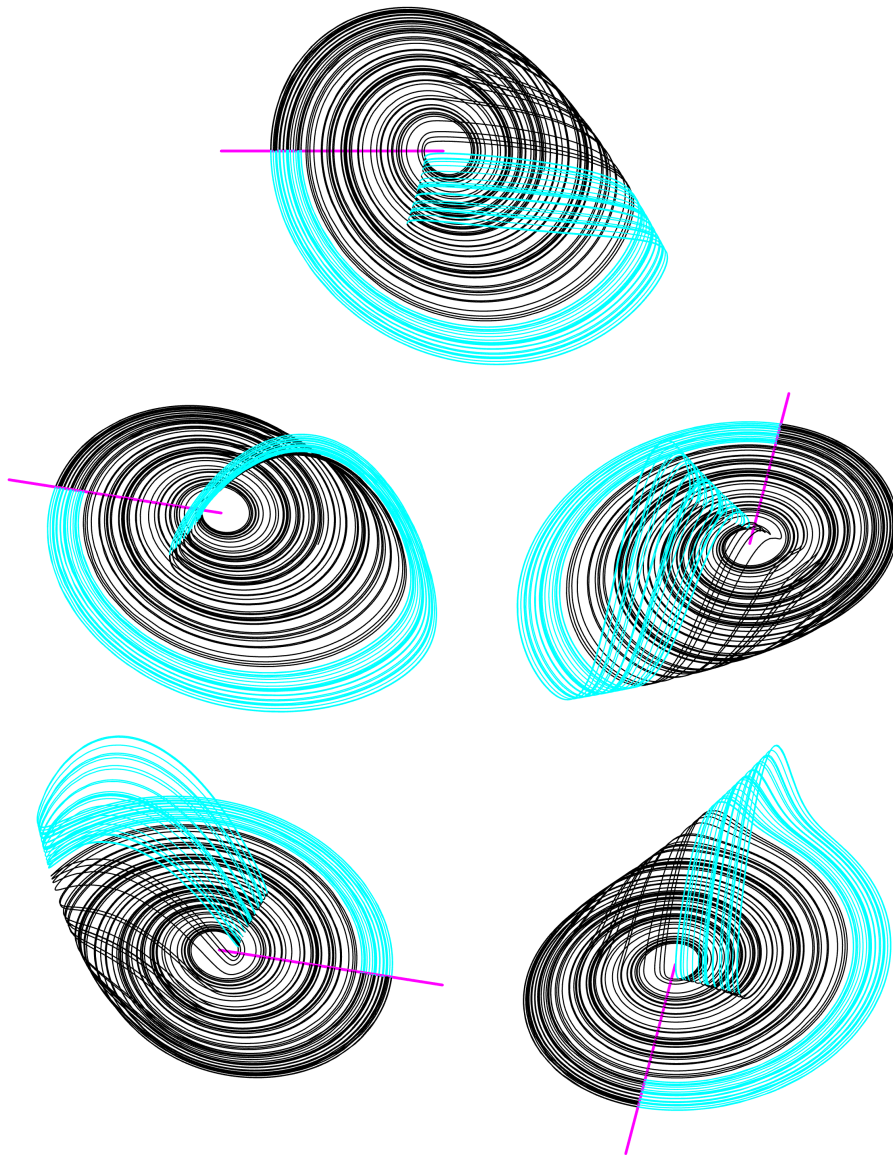


Figure 4.2 - Additional views from the non-coherent Rössler, as in Fig. 4.1(d). The Poincaré Section $y = 0, x < 0$ is plotted in magenta. Portions of the trajectory in cyan contain sub-cycles, that is, with local minimum in x satisfying $y < 0$ and $z > 0.1$. The rest of the trajectory is shown in black.

versions of the Rössler oscillator from Eq. (4.2). A reference phase is obtained via one of these four methods. Then, noise can be added to time series and some of its coordinates are used as input for the candidate method for phase assignment. The result obtained is finally compared with the reference one.

One drawback to proceed this way is that some features of the proposed method may be hidden by the characteristics of the reference phase assignment itself. So, this was the motivation to devise models for chaotic oscillators showing “canonical phase” in some sense.

Of course, phase assignment itself is not unique. We emphasize that our main objective is to provide an additional tool to enhance understanding of how phase assignment methods operate.

4.2 The DSTB construction

We include in this section the Double Strip Test Bed (DSTB) for phase assignment methods as in (FERREIRA et al., 2015). This test bed consists into embedding phase variable time series into a three dimensional surface combining an annulus and a Möbius Strip. This surface was designed following the exaggerated paper-sheet model for the coherent Rössler system (LETELLIER; ROSSLER, 2006)(Fig. 4). Other two embedding surfaces, into the circle and into the classic Möbius Strip, can be found at Ref. (FERREIRA et al., 2015).

The oscillator’s position in the DSTB is parametrized by $v \in [0, 1]$, which is constant per oscillator’s cycle and defines its transversal position over each strip, and a phase ϕ , which actually characterizes the trajectory spins. Thus, we denote points in the three dimensional surface by $X(v, \phi)$. Phase variable as input time series $\phi(t)$ could be directly constructed or obtained from a system already described in phase variables, like the KM.

Our map $X(v, \phi)$ will be defined such that, after each complete cycle of the oscillator, it returns to a Poincaré Section S given by the line segment joining the origin to $(1, 0, 0)$, more specifically $X(v, 2k\pi) \in S$ for all $k \geq 0$ and all $v \in [0, 1]$. As an embedded trajectories crosses S , its transversal parameter v is updated to $P(v)$. Therefore, we may also define a Poincaré map $P(v_k) = v_{k+1}$ of the successive returns of the orbit to S , since $X(v_k, 2(k+1)\pi) = (v_{k+1}, 0, 0) \in S$.

If $v \in [0, 0.5]$, the trajectory starting at $(v, 0, 0) \in S$ will travel in its next cycle $\phi \in [0, 2\pi)$ through the Annulus Strip - Fig 4.3(a). In this strip, v is expanded to

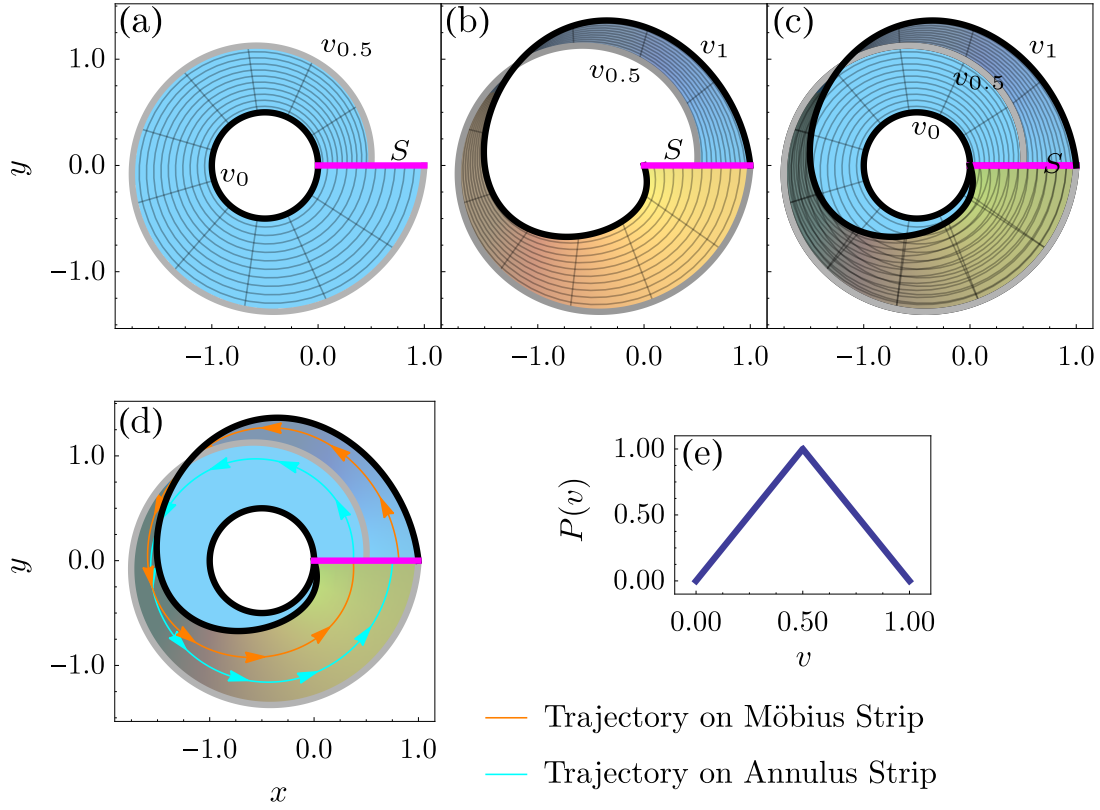


Figure 4.3 - (a,b,c) Double Strip Construction Scheme. (d) Two spins of the trajectory, each one over a different strip. (e) The Poincaré Return Map of section S . The Poincaré Section S is depicted in Magenta.

$P(v) = 2v$ once it crosses S again.

If $v \in (0.5, 1]$, it will follow the Möbius Strip - Fig 4.3(b). In this strip an inversion occurs, so v is updated to $P(v) = -2v + 2$ for the next cycle. The combination of these two strips, the DSTB, is shown at Fig 4.3(c).

We can argue that the dynamics in the Double Strip is chaotic, since its Poincaré Map P is the Tent Map, see Fig 4.3(e), which is a classical chaotic discrete map (ALLIGOOD et al., 1997).

Geometrically, the image of X was designed such that $X([0, 0.5] \times [0, 2\pi])$ interpolates between curves $v_0([0, 2\pi])$ and $v_{0.5}([0, 2\pi])$, which forms the Annulus Strip (Fig 4.3(a)); while $X([0.5, 1] \times [0, 2\pi])$ interpolates between $v_{0.5}([0, 2\pi])$ and $v_1([0, 2\pi])$, defining the Möbius Strip, (Fig 4.3(b)). The actual expression of the embedded trajectories in the DSTB are given bellow.

The position of the oscillator in the Annulus Strip is given by $X(v, \phi) = f(v, \phi)$ defined by

$$f(v, \phi) := (1 - \lambda_f(v))v_0(\phi) + \lambda_f(v)v_{0.5}(\phi), \text{ for } (v, \phi) \in [0, 0.5] \times \mathbb{R},$$

where $v_0(\phi) := 0.5(\cos \phi, \sin \phi, 0) - (0.5, 0, 0)$; $v_{0.5}(\phi) := (\phi/(4\pi) + 1)(\cos \phi, \sin \phi, 0) - (0.5, 0, 0)$; and $\lambda_f(v) := 2v$. In the other hand, the position of the oscillator in the Inversion Strip is given by $X(v, \phi) = g(v, \phi)$ with

$$g(v, \phi) := (1 - \lambda_g(v))v_{0.5}(\phi) + \lambda_g(v)v_{1.0}(\phi), \text{ for } (v, \phi) \in (0.5, 1] \times \mathbb{R},$$

where $v_{1.0}(\phi) := ((1 + 0.5\gamma(\phi) \cos(\phi/2)) \cos \phi - 0.5, (1 + 0.5 \cos(\phi/2)) \sin(\phi), 0.5 \sin(\phi/2))$; $\gamma(v) := 0.5(v - \pi)^2/\pi^2 + 0.5$; and $\lambda_g(v) := -1 + 2v$.

Fig 4.3(d) illustrates two spins over the DSTB with $\theta(t) = t$ and $v_0 = 0.82$. Starting with $t = 0$, the first cycle (orange curve) runs through the Möbius Strip, since $v_0 \in (0.5, 1]$. When $t = 2\pi$, the trajectory reaches S again and v_0 is updated to $v_1 = P(v_0) = 0.36$, which means that the second cycle (cyan curve) runs through the Möbius Strip for $t \in (2\pi, 4\pi]$.

4.3 Example of DSTB usage

In this section we compare the phases obtained through the four methods discussed in Section 4.1 with the reference phase intrinsically derived from the DSTB.

Instead of a single oscillator, as previously illustrated in Fig. 4.1, we analyze now synchronization between two coupled oscillators via phase difference. The seeds of each oscillator in this numerical experiment are $v_1 = 0.24$ and $v_2 = 0.206$. Three behavior are imposed, each one at a third of the time interval studied:

- $t \in [0, 1)$: Near phase-locking with phase difference $\theta_2 - \theta_1 \approx \pi/6$ and both oscillators over the same strip - Fig. 4.4(a).
- $t \in [1, 2)$ Phase slip with the second oscillator performing one additional spin relative the first one - Fig. 4.4(b).
- $t \in [2, 3)$ Near phase-locking with phase difference $\theta_2 - \theta_1 \approx \pi/6$ and oscillators in different strips - Fig. 4.4(c).

To achieve this particular synchronization profile, our phases were empirically chosen as $\theta_1(t) = 2\pi t$ and $\theta_2(t) = 2\pi t + h(t)$, where $h(t) =$

$$2\pi(\arctan(100(t - 1.5)) / \pi + 0.5) + \pi/6.$$

We applied the four methods for phase assignment in this context and the outcome is discussed below.

The Poincaré method followed closely both phase-locking regimes. However, it could not precisely show the moment when the phase-slip occurred.

The Arctan and Dotarctan methods also detected phase-locking in the first interval and phase-slip around $t = 1.5$. During the second phase-locking interval, where the trajectories ran over different strips, larger fluctuations around the reference phase were observed, specially for Dotarctan method.

Finally, the Hilbert method presented even larger fluctuations. Again, the second phase-locking interval showed less precise results. In contradistinction, this method sharply detected the phase slip instant, like the Arctan and Dotarctan methods.

4.4 Conclusions and perspectives

The usage of mock chaotic oscillators can provide useful information about how method for phase assignment operate. This is done by investigating how these methods respond to fixed synchronization regimes that are known a priori.

As future research, we plan to explore variations of such model including for instance a funnel-like structure like the non-coherent Rossler. Moreover, it is possible to devise mocks for other models like the Lorenz system.

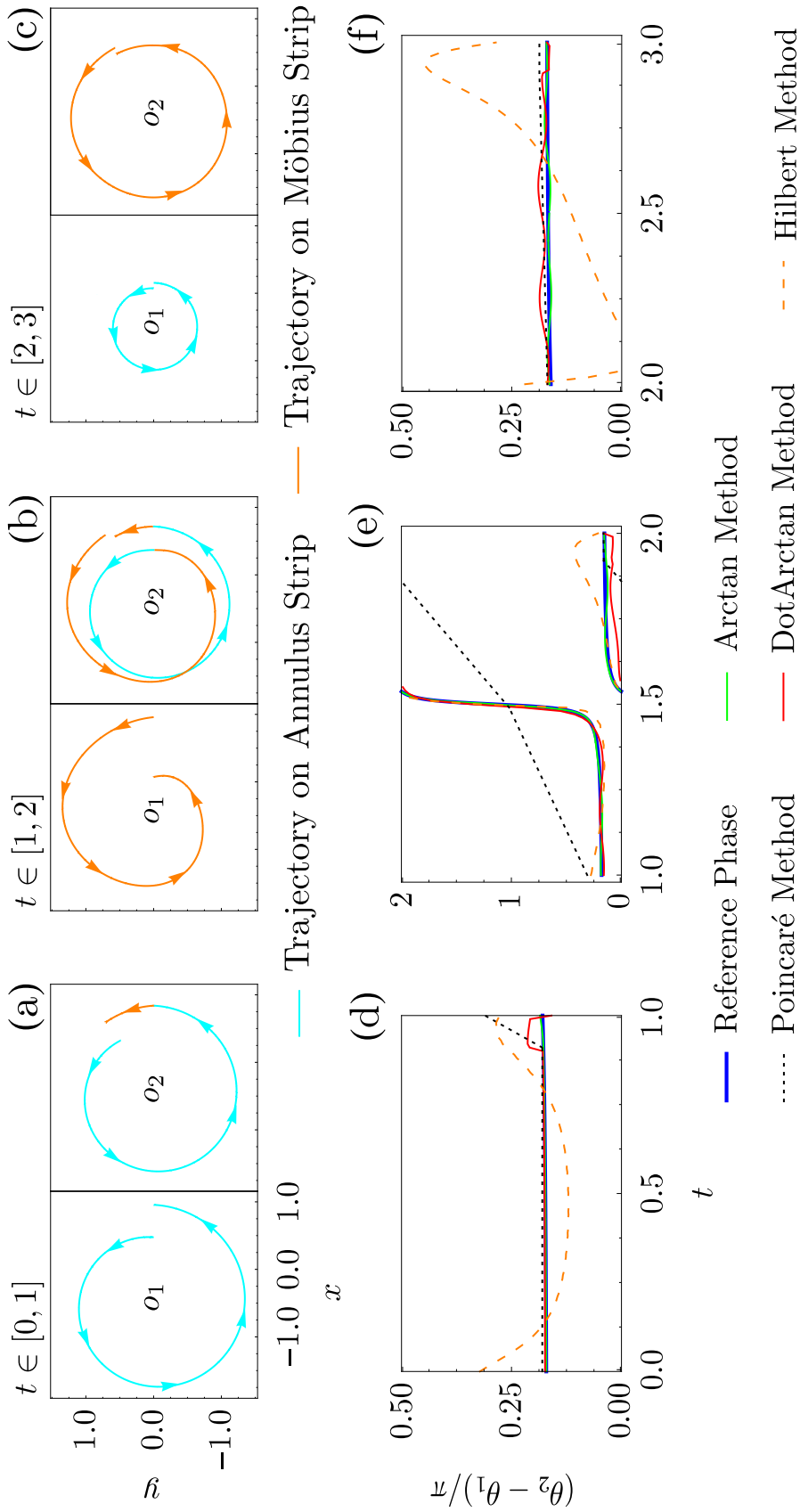


Figure 4.4 - DSTB example with two coupled oscillators: (a,d) Phase locking (d,e) Phase Slip (c,f) Phase locking. The upper pictures are the oscillators

5 DESERTER HUBS MODEL

Phase-synchronization is commonly associated with attractiveness, while repulsive coupling drags oscillators apart and often leads to desynchronized states. Nevertheless, the nature of the coupling can depend non-trivially on the level of synchrony itself.

Such coupling schemes are called nonlinear in general. They have been explored in theoretical (FILATRELLA et al., 2007; ROSENBLUM; PIKOVSKY, 2007; PIKOVSKY; ROSENBLUM, 2009; BAIBOLATOV et al., 2009) and experimental (TEMIRBAYEV et al., 2012; TEMIRBAYEV et al., 2013) studies dealing with global coupling setup. An underlying topic in these articles is partial synchrony at moderate coupling strengths, which is achieved through the balance of attractive and repulsive trends.

This scenario can be relevant for instance regarding deep brain stimulation of neural synchronous oscillations at Parkinson disease by a nonlinear feedback (POPOVYCH et al., 2005).

We introduced and studied a version of the Kuramoto Model (KM), with nonlinear coupling explicitly depending on a local cohesion quantifier, yielding the so-called *Deserter Hubs Model* (DHM). This study has already been published at Ref. (FRITAS et al., 2015a), see Appendix B, thus we restrict ourselves in this chapter to the main concepts and discussions.

Units in the DHM can switch from “conformist” to a “contrarian” behavior, that is, from attraction to repulsion, when pressure from neighbors becomes too intense. Thus, it can be considered as a dynamical generalization of the inhomogeneous populations from Ref. (HONG; STROGATZ, 2011), where the kind of behavior depends on the force acting on it. Since this transition occurs first for oscillators connected to many others, this model can fairly understood as Deserter Hubs Model.

More specifically, we deal with an ensemble of identical phase-oscillator like in Ref. (PIKOVSKY; ROSENBLUM, 2009), generalizing its results to simple coupling graph instead of all-to-all coupling.

Among dynamics regimes, we found phase-locking, multi-multistability, chaos and periodic order parameter.

We include in the first section the description of the DHM, while the second one includes a theorem with sufficient conditions for phase-locking. The third numerical

experiment shows a variety of qualitative dynamical behaviors.

5.1 The Deserter Hubs Model (DHM)

Consider a system of N phase-oscillators, whose dynamics is given by the following set of ordinary differential equations

$$\dot{\theta}_i = \left(1 - \eta Z_i^2\right) \sum_{j=1}^N A_{ij} \sin(\theta_j - \theta_i), \quad (5.1)$$

for $i = 1, \dots, N$. Like in the classic KM from Eq. (3.15) in Sec. 3.4, the coupling graph is simple, connected and symmetric, with $A_{ij} = A_{ji} = 1$ if there is an edge between the i -th and j -th oscillators, and $A_{ij} = A_{ji} = 0$ otherwise. Diffusive sinusoidal coupling function is used, so that, each direct edge contributes with the sinus of phase difference to the dynamic of the i -th oscillator.

Oscillators have identical natural frequency $\langle \omega \rangle = \omega_1 = \dots = \omega_N$, so, one can express them in rotating reference frame and suppress $\langle \omega \rangle$, like in Sec. 3.3.

Instead of the standard coupling parameter ε , from Eq. (3.15), our model employs the *nonlinear coupling parameter*¹ η . Therefore, if $\eta = 0$, the classic KM with constant unitary coupling parameter is recovered.

The cohesion quantifier used is the *local mean field* $Z_i \in [0, d_i]$, as in Eq. (3.16). Recall from Sec. 3.4 that $Z_i = d_i$ corresponds to full synchronization regarding members in the neighborhood of the i -th oscillator; while $Z_i = 0$ implies that they are in splay synchronization.

Observe that a necessary condition for a node to be able to suffer repulsive coupling, i.e., $1 - \eta Z_i^2 < 0$, is that $\eta > d_i^{-2}$. On the other hand, if $\eta < d_{\max}^{-2}$, where d_{\max} is the largest node-degree in the network, there will be no repulsive behavior in the system and full synchronized state $R = 1$ is a stable regime as will be shown in the next section.

Next, suppose that there is a single maximal hub in the network and denote its local mean field by Z_{\max}^2 . In addition, let η becomes larger than d_{\max}^{-2} and the maximal hub start as conformist. In a first moment, all oscillators get closer to full synchronization, R increases and also Z_{\max}^2 . This can yield $1 - \eta Z_{\max}^2 < 0$, which shifts this node to repulsion (contrarian). This is inspiration for the name of the model, since hubs may

¹Ref. (FREITAS et al., 2015a) denotes the nonlinear coupling parameter by ε . To avoid notation conflict, we changed it in this text.

go against the crowd, they renege, in other words, they become deserters. As a result, Z_{max}^2 may decrease and switch again the node to attraction.

In fact, depending on the coupling graph A , on the initial condition $(\theta_1^0, \dots, \theta_1^N)$, and on the intensity of the nonlinear coupling parameter η , numerical simulation from Sec. 5.3 reveals that model (5.1) can exhibit different qualitative behaviors.

5.2 Stability of full synchronization

Under small nonlinear coupling parameter η , the full synchronization is a robust phenomenon related to small perturbations over initial conditions regarding the DHM from Eq. (5.1). More specifically, our aim in this section is to show that if η is smaller than a critical value $\eta_c := 1/d_{max}^2$, then the synchronized stated ($R = 1$) is Lyapunov stable.

Our argument in this section employs a generalized norm of the order parameter to define our Lyapunov function, with the same outline from (JADBABAIE et al., 2004).

To do so, instead of the adjacency matrix A , we will rewrite Eq. (5.1) in terms of its *directed incidence matrix* B , which is a matrix with N rows and E columns, where E is the number of *directed edges*. See Sec. 2.1 for examples of this graph notation.

The usage of the directed incidence matrix allows us to reformulate model (5.1) in a vector form:

$$\dot{\theta} = -\frac{1}{2} \text{diag}(1_N - \varepsilon Z^2) B \sin(B^\top \theta), \quad (5.2)$$

where $Z^2 := (Z_1^2, \dots, Z_N^2)$, $1_N := (1, \dots, 1) \in \mathbb{R}^N$ and $\text{diag}(\cdot)$ stands for the matrix with the elements of a vector on the leading diagonal, and 0 elsewhere.

Direct substitution ensures that the square of the global order parameter can be cast as

$$R^2 = \frac{1}{N^2} \left(N + 2 \sum_{j < k} \cos(\theta_j - \theta_k) \right).$$

We define a *generalized norm of order r* to build our Lyapunov function as

$$r^2 := 1 - \frac{E - 1_E^\top \cos(B^\top \theta)}{N^2}. \quad (5.3)$$

Note that R^2 requires the sum of *all* $\cos(\theta_j - \theta_k)$ with $j < k$ (for $j, k = 1, \dots, N$), but its generalization r^2 takes into account the sum $(1_E^\top \cos(B^\top \theta))$ *only* through the

edges of the graph.

For any connected symmetrical coupling graph, one can check that the maximum of r^2 is the unit, and that $R^2 = 1$ if and only if this value is achieved .

We choose the following candidate to Lyapunov function

$$U(\theta) = 1 - r^2. \quad (5.4)$$

It is clear that the minimum value of $U(\theta) = 0$ corresponds to the maximum value of $r^2 = 1$, which is equivalent to the fully synchronized state.

In fact, algebraic manipulations show that

$$U(\theta) = \frac{2}{N^2} \left\| \sin \left(\frac{B^\top \theta}{2} \right) \right\|^2, \quad (5.5)$$

and that the differential of U is given by

$$DU = \frac{1}{N^2} \left(B \sin(B^\top \theta) \right)^\top. \quad (5.6)$$

Therefore, using the vector form of the model (5.2) and the expression of the differential DU from (5.6), we have that $\frac{d}{dt}U(\theta(t))$ equals to

$$- \frac{1}{2N^2} \left(\sin(B^\top \theta) \right)^\top B^\top \text{diag}(1_N - \varepsilon Z^2) B \sin(B^\top \theta), \quad (5.7)$$

If we set $x := B \sin(B^\top \theta)$, then we have that $x^\top \text{diag}(1_N - \varepsilon Z^2) x$ is larger or equal than $(1 - \varepsilon d_{\max}^2) \|x\|^2$. Moreover, we can also define a lower bound for $\|x\|^2$, since $\|x\|^2 = \sin(B^\top \theta)^\top B^\top B \sin(B^\top \theta) \geq \lambda_2(B^\top B) \left\| \sin(B^\top \theta) \right\|^2 = 2\lambda_2(L) \left\| \sin(B^\top \theta) \right\|^2$; where $\lambda_2(L)$ is the algebraic connectivity of the graph. In the last inequality we used that $\frac{1}{2}BB^\top = L$ and that both matrices BB^\top and $B^\top B$ have the same non-trivial eigenvalues $0 \leq \lambda_2(L) < \dots < \lambda_N(L)$, where $\lambda_2(L)$ is strictly larger than zero because the coupling graph A is connected (GODSIL; ROYLE, 2001). Thus,

$$\frac{d}{dt}U(\theta(t)) \leq -\frac{1}{N^2} \lambda_2(L) (1 - \varepsilon d_{\max}^2) \left\| \sin(B^\top \theta) \right\|^2$$

As a result, $\varepsilon < \varepsilon_c := 1/d_{\max}^2$ implies that $\frac{d}{dt}U(\theta(t)) \leq 0$, then the fully synchronized state $R = 1$ is stable.

5.3 Examples of behaviors

As it was claimed before, in dependence on the network structure, very different types of the dynamics are possible. In order to give impression on it, we present simulations of model (5.1) with two different coupling graphs displayed as inserts in Fig. 5.1. Both networks have $N = 10$ nodes and they differ only by the rewiring of a single edge. We performed simulations for 10 random initial conditions chosen with uniform distribution over $[0, 2\pi]$ for each experiment. For all these initial conditions $l = 1, \dots, 10$, the norm of the order parameter $R^l(t)$ is computed from the time series. As explained in the previous section, in these calculations a transient time is eliminated and that a statistically stationary regime \tilde{I} of 10^3 units of time and $\#\tilde{I} := 10^5 + 1$ points is considered. Then, also for each distinct initial condition, the maximum, average and minimum values of the associated norm of the order parameter are computed, respectively denoted by $R_{\max}^l := \max_{t \in \tilde{I}} R^l(t)$; $\langle R^l \rangle := (\#\tilde{I})^{-1} \sum_{t \in \tilde{I}} R^l(t)$; and $R_{\min}^l := \min_{t \in \tilde{I}} R^l(t)$. Of course, $R^l(t)$ converges to a constant if and only if $R_{\max}^l = \langle R^l \rangle = R_{\min}^l$. Now, having different simulations for a fixed coupling graph, we evaluated the maximum, average and minimum value of the *average* value of the norm of the order parameters over this ensemble, respectively denoted by $\max\{\langle R \rangle\} := \max_{l=1, \dots, 10} \langle R^l \rangle$; $\text{mean}\{\langle R \rangle\} := (10)^{-1} \sum_{l=1, \dots, 10} \langle R^l \rangle$; and $\min\{\langle R \rangle\} := \min_{l=1, \dots, 10} \langle R^l \rangle$. So, if the norm of the order parameter converges to the same value for *all* initial conditions simulated, then $\max\{\langle R \rangle\} = \text{mean}\{\langle R \rangle\} = \min\{\langle R \rangle\}$. For the cases where the norm of the order parameter does not converge over all initial conditions, it will be useful to examine the *overall maximum* and *overall minimum* values of the norm of the order parameter, respectively denoted by $\max\{R_{\max}\} := \max_{l=1, \dots, 10} R_{\max}^l$; and $\min\{R_{\min}\} := \min_{l=1, \dots, 10} R_{\min}^l$. Thus, if there is no fixed phase synchronization for all the initial conditions simulated, but the norm of the order parameter presents only small deviations around a common value, then the gap between $\max\{R_{\max}\}$ and $\min\{R_{\min}\}$ is also small. Also notice that $\min\{R_{\min}\} \leq \min\{\langle R \rangle\} \leq \text{mean}\{\langle R \rangle\} \leq \max\{\langle R \rangle\} \leq \max\{R_{\max}\}$, since $R_{\min}^l \leq \langle R^l \rangle \leq R_{\max}^l$ for all initial conditions. Finally, the maximum Lyapunov exponent λ_{\max}^l for each initial condition is also computed, according to the algorithm in (ALLIGOOD et al., 1997). The maximum Lyapunov exponent over all the chosen initial conditions $\lambda_{\max}^l := \max_{l=1, \dots, 10} \lambda_{\max}^l$ is also analyzed.

We now describe different regimes observed in the networks, using also Fig. 5.2, where we depict time series of $R(\theta(t))$ for some particular choices of ε , indicated as green letters in the upper panel from Fig. 5.1 (this is the case we choose for illustrating different regimes). Notice that $d_{\max} = 4$ in both cases, so Theorem ??

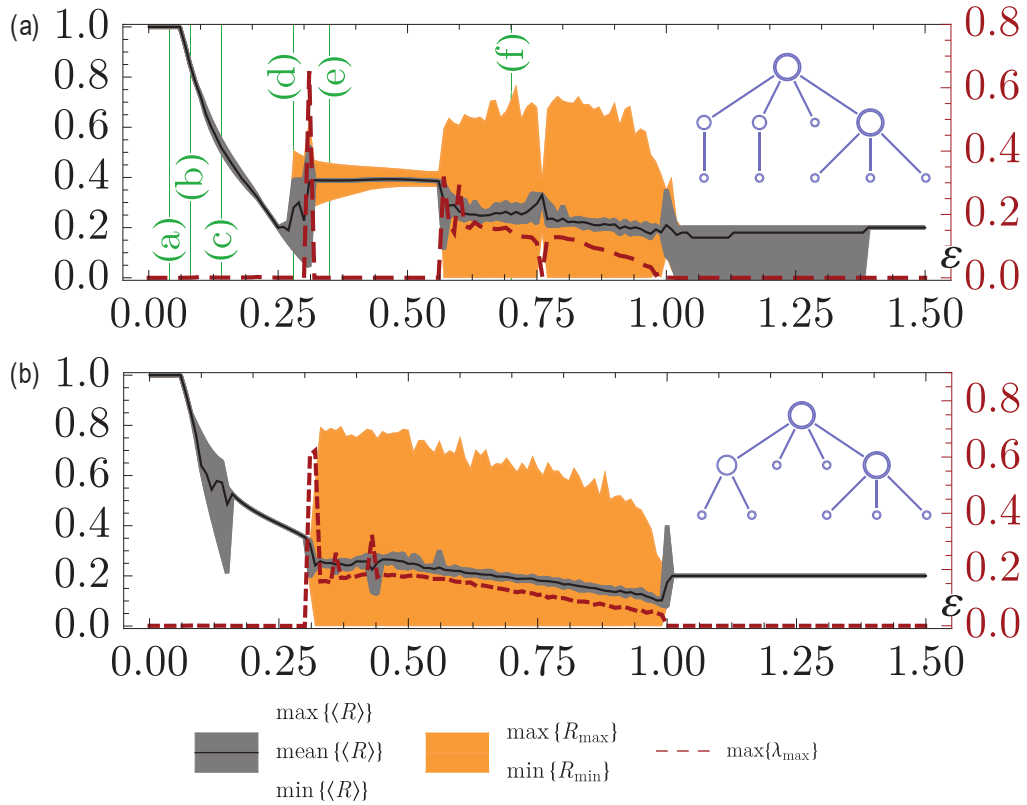


Figure 5.1 - Numerical results for Model (5.1) as a function of ε , for the coupling graphs depicted as inset, including 10 random initial conditions. A black line corresponds to $\text{mean}\{\langle R \rangle\}$, while the interval between $\text{min}\{\langle R \rangle\}$ and $\text{max}\{\langle R \rangle\}$ is shown as a gray strip. The gap between $\text{min}\{R_{\text{min}}\}$ and $\text{max}\{R_{\text{max}}\}$ is shown as an orange strip. Since the orange strip is by construction larger or equal than the gray one, the first one is not displayed in the figure when they coincide. Left vertical axes show values related to norm of the order parameter, while the right ones represents the maximum Lyapunov exponent λ_{max} , shown as a red dashed line. Letters in green vertical lines from the upper experiment correspond to subfigures in Fig. 5.2.

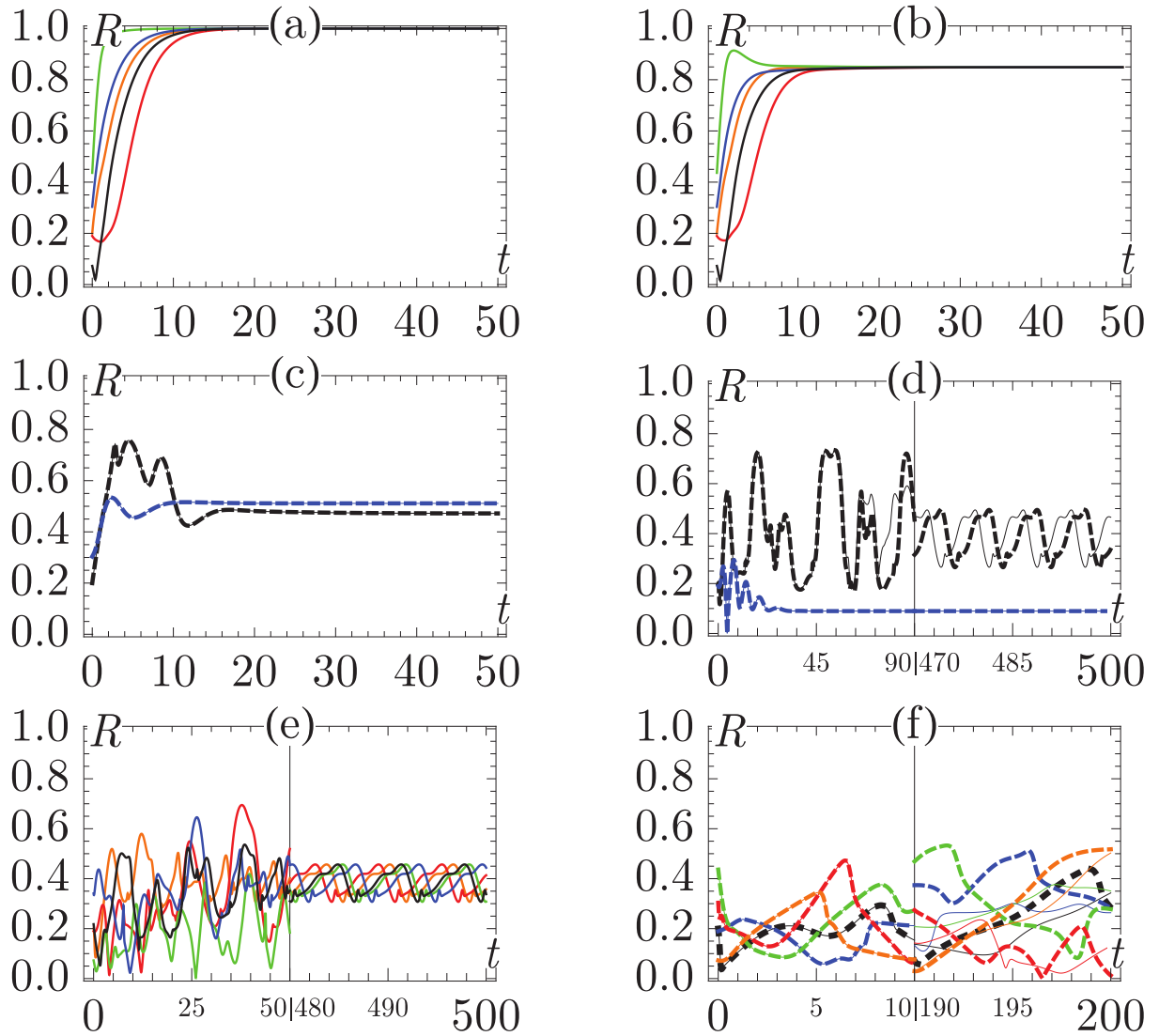


Figure 5.2 - Evolution of $R(t)$ for different values of ε indicated in green at the upper experiment from Fig. 5.1. Every color represents a different initial condition, while pairs of solid/dashed lines with the same color correspond to solutions whose initial conditions differ not more than 10^{-4} at each coordinate. (a) $\varepsilon = 0.04$: full synchronization; (b) $\varepsilon = 0.08$: fixed phase synchronization; (c,d,e) $\varepsilon = 0.15, 0.28, 0.35$ respect.: examples of multi stability; (f) $\varepsilon = 0.70$: example with $\lambda_{\max} > 0$.

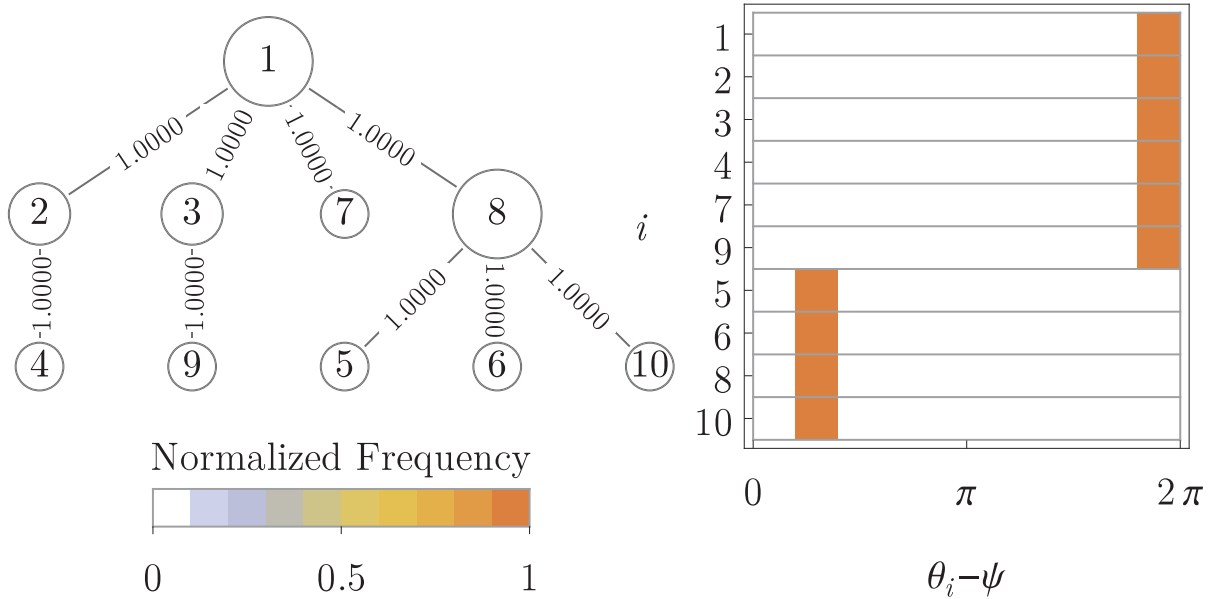


Figure 5.3 - Example of group formation: details of one of the trajectories from Fig. 5.2 (b) $\varepsilon = 0.08$. On the left side, the coupling graph with $s(i, j)$ in its edges is shown. On the right side, a histogram of $\theta_i - \psi$ in permanent regime is presented with color code representing the normalized frequency. Precisely, we divided the interval $[0, 2\pi)$ into 10 bins with the same size. So, the normalized frequency of the i -th oscillator corresponds to the ratio of points (after the transient time) that the numerical evaluation of $\theta_i - \psi$ placed at each bin.

guarantees that for $\varepsilon < \varepsilon_c = 1/4^2 = 0.0625$ the full synchronization state, $R \rightarrow 1$, is locally stable as illustrated in Fig. 5.2 (a) (with $\varepsilon = 0.04$).

Panel (a) in Fig. 5.2 illustrates full synchronization in the network for $\varepsilon < \varepsilon_c$. For ε slightly bigger than ε_c , simulations suggest that a stationary regime of partial phase synchronization, where $R \rightarrow c < 1$, is locally stable as shown in Fig. 5.2(b) ($\varepsilon = 0.08$). Details of this state are clear from Fig. 5.3. There we show that the synchronization between the individual oscillators is complete if measured by quantity s_{ij} , and all the oscillators have the same frequency. However, the oscillators are split into two groups with a constant phase shift between them; this division originates in the edge which connects the two largest hubs in the network (vertexes 1, 8).

For larger values of ε , the regimes are still static but with multistability. For instance, at $\varepsilon = 0.15$ (see Fig. 5.2 (c)) two stable configurations emerge with $R \rightarrow c$, with $c \approx 0.471$ (black) or $c \approx 0.511$ (blue), depending on the initial condition. Fig. 5.4, which is analogous to Fig. 5.3, shows the existence of three subgroups, whose members

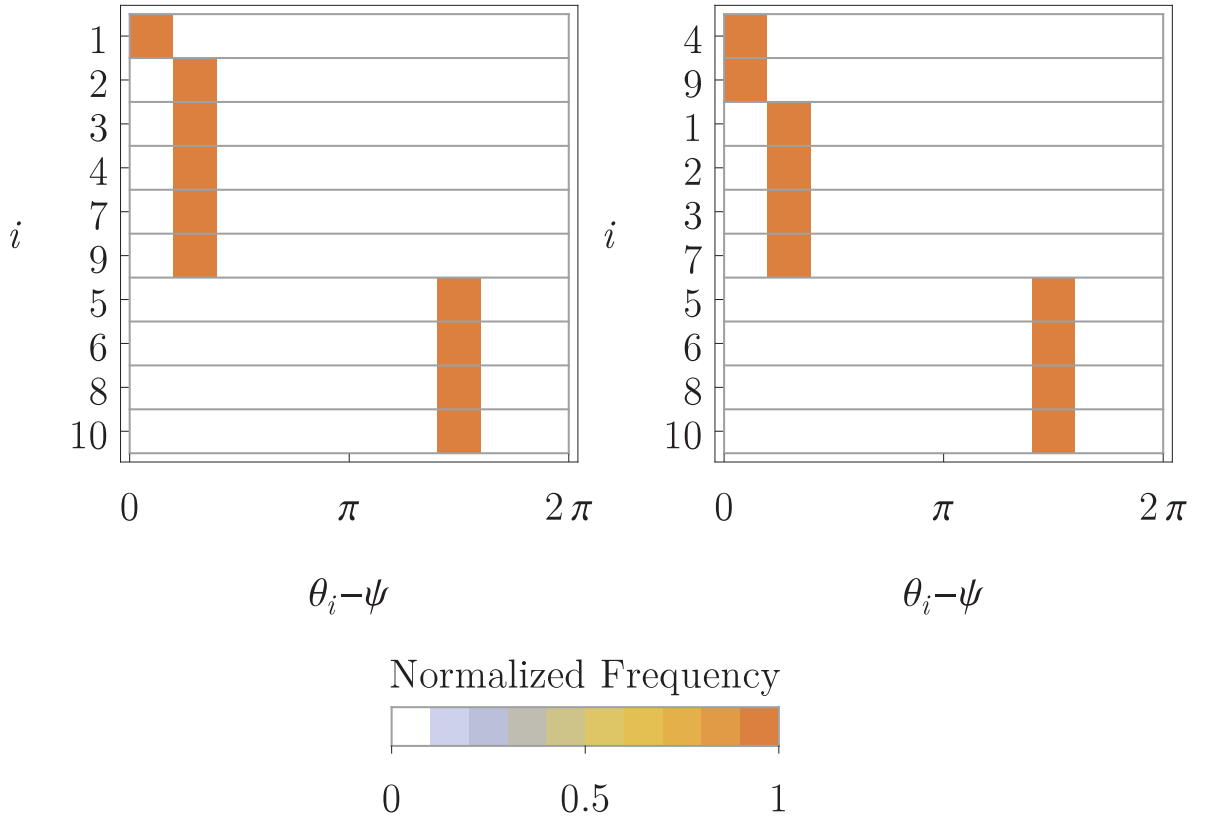


Figure 5.4 - Example multi-stability with group formation. Details of two trajectories from Fig. 5.2 (c) $\varepsilon = 0.15$ are provided. The left picture corresponds to the solid black line and the right one to the solid blue. Histograms of $\theta_i - \psi$ are like the one in Fig. 5.3.

may vary according to the initial condition.

Other types of multistabilities appear for instance at $\varepsilon = 0.28$ and $\varepsilon = 0.35$, as illustrate in Figs. 5.2 (d,e). For $\varepsilon = 0.28$ (panel d) some initial conditions do not converge to a fixed phase synchronization, but to a regime where the order parameter R is periodic in time. For $\varepsilon = 0.35$ (panel c), the norm of the order parameter of all trajectories simulated becomes periodic. Fig. 5.5 provides an illustration of this regime.

For $\varepsilon = 0.70$ (Fig. 5.2 (f)), one observes a chaotic state with $\lambda_{\max} > 0$, the distribution of phases and frequencies is illustrated in Fig. 5.6.

The emergence of chaos in the DHM can be seen as the result of irregular contractions and expansions of the oscillator's state (ALLIGOOD et al., 1997). Contraction tendencies occur when a node act as conformist (attractiveness), while expansion

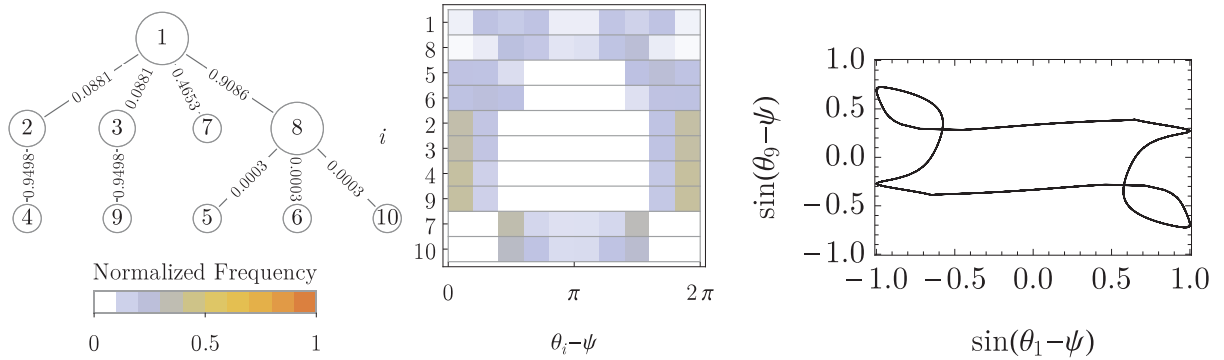


Figure 5.5 - Example of periodic norm of the order parameter: details of one of the trajectories from Fig. 5.2 (d) $\varepsilon = 0.28$. On the left side, the coupling graph with $s(i, j)$ in its edges is shown. A histogram of $\theta_i - \psi$ are like the one in Fig. 5.3 in the middle figure. We denote by $\psi(t)$ the argument of the order parameter. The picture on the right shows that the curve $(\sin(\theta_1(t) - \psi(t)), \sin(\theta_9(t) - \psi(t)))$ is closed.

takes place when it “deserts” due to local mean field cohesion (repulsiveness). When no balance is achieved between these two tendencies, one can observe sensitiveness to initial conditions.

If $\varepsilon \in [1, 1.5]$, we also obtained multistability, with the coexistence of solutions converging to phase-lock and irregular order parameter after the transient, similar to Fig. 5.2(d).

Now, we compare the results for two slightly different networks depicted in panels (a) and (b) in Fig. 5.1. The interval of values of ε with fixed phase synchronization for all initial conditions simulated is very similar for both networks, namely $\varepsilon_c < \varepsilon \lesssim 0.25$; also multistability of static partial synchronous regimes have been observed in both cases.

When $\varepsilon \in [1, 1.5]$, contrary to case (a), we observed that the solution for all initial conditions converged to the same phase-lock regime, similar to Fig. 5.2 (b).

In the conclusion of this section, Fig. 5.7 shows simulation results for two other networks. Panel (a) shows a random network with $N = 10$ nodes and 20 undirected edges. Here predominantly static regimes are observed, only in small ranges of coupling constant chaos with a positive Lyapunov exponent appears. Static regimes, however, demonstrate a large degree of multistability. In panel (b) we show a scale-free network with $N = 50$ nodes and 100 undirected edges. Here static states are rare, typically irregular regimes with low values of the order parameter are observed.

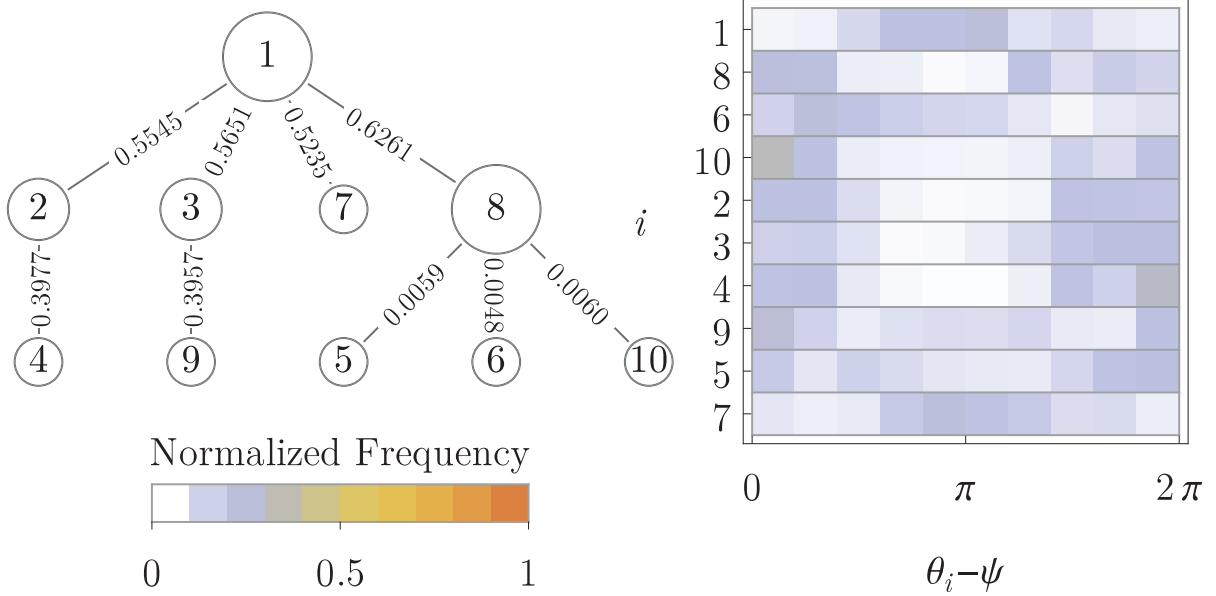


Figure 5.6 - Example of trajectory with $\lambda_{\max} > 0$: details of one of the trajectories from Fig. 5.2 (f) $\varepsilon = 0.70$. On the left side, the coupling graph with $s(i, j)$ in its edges is shown. On the right side, there is a histogram of $\theta_i - \psi$ are like the one in Fig. 5.3.

5.4 Dependence of partial synchronization regimes on network structure

We have seen that partially synchronous states can be rather different even for similar networks. It is therefore difficult to make general predictions for a relation between the network properties and the dynamical behaviors. Here we attempt such a description, focusing on the property of abundance of static regimes in comparison to time-dependent ones. For this purpose we define the *convergence index* I_c as the ratio of values of $\varepsilon \in [0, 1.5]$ such that R converges to a constant value, considering all the 10 random initial conditions. So, both networks in Fig. 5.1 have close values of this index: $I_c \approx 0.530$ in case (a) while $I_c \approx 0.549$ in case (b). In contradistinction, network shown in Fig. 5.7(a) has very large value of the index $I_c \approx 0.946$, while that in Fig. 5.7(b) a rather low value $I_c \approx 0.064$.

In order to explore which features of the coupling graph are related with I_c , we performed numerical experiments with three sets of graphs, with $N = 10, 50, 100$ nodes. Each set consists in three common types of networks, each one with 10 members, generated as: (i) random (Erdős-Rényi) graphs with $2N$ edges; (ii) scale-free graphs, also with $2N$; and (iii) tree graphs (N edges). The Barabási-Albert algorithm is applied for the last two types of networks (ii),(iii), with an initial clique of m_0 nodes and with other nodes been connected to m existing ones. For the $2N$ -

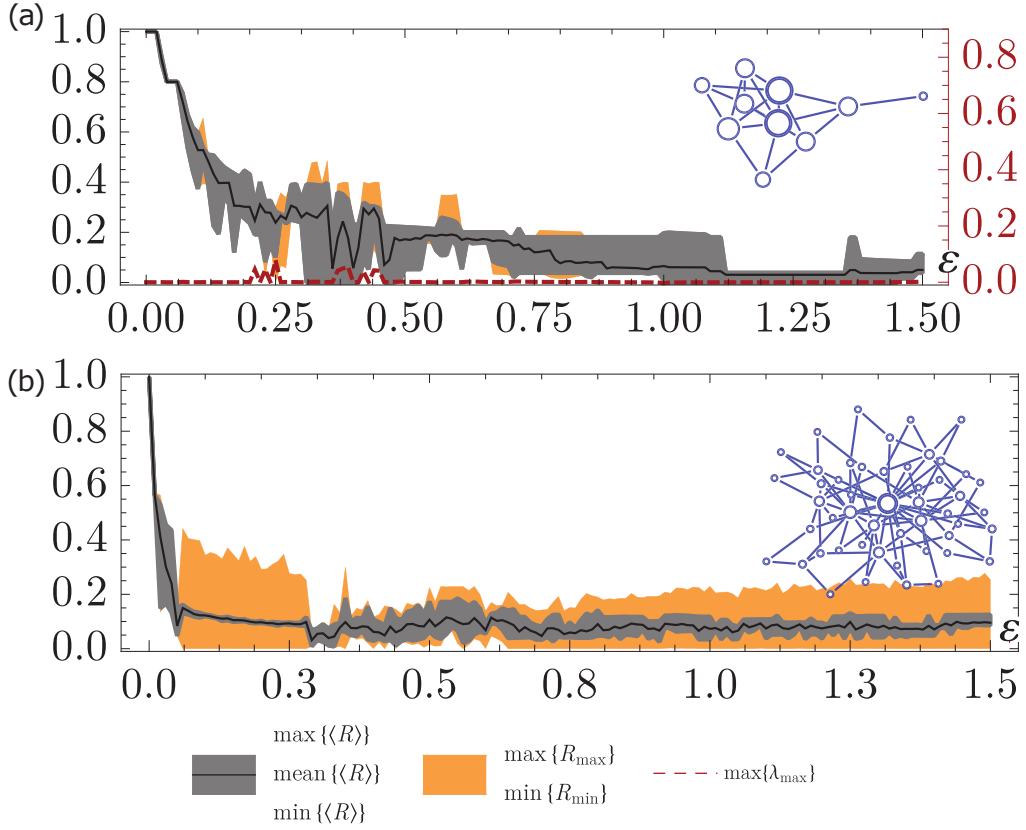


Figure 5.7 - Numerical results for Model (5.1) as a function of ε , for the coupling graphs depicted as inset, including 10 random initial conditions. The legend of the pictures is the same as in Fig. 5.1

edges scale-free graphs, we fixed $m_0 = 5$ and $m = 2$; while for the tree graphs (N edges scale-free graphs), $m_0 = m = 1$. We point out that all graphs created are connected and symmetrical. Additionally, three sets of 10 initial conditions $\theta_0 \in \mathbb{R}^N$, with uniform distribution over $[0, 2\pi]$ and $N = 10, 50, 100$, have been explored. So, for each of the 90 coupling graphs we computed its correspondent I_c values by numerical integration of model (5.1) for $\varepsilon = 0, 0.01, \dots, 1.49, 1.50$.

In Table 5.1 we report the mean value and the standard deviation of I_c for each topology and size of coupling graph. From these data we see that the mean value of I_c increases if we go from tree to scale-free and to random graphs, respectively. However, this difference becomes less noticeable for larger values of N . Both the mean value and the standard deviation of I_c decrease with larger networks.

We have explored different networks metrics, searching for one mostly correlated with the convergence index I_c . Let $0 = \gamma_1 < \gamma_2 \leq \dots \gamma_N$ denote the Laplacian

Network	$N = 10$	$N = 50$	$N = 100$
Tree	0.421 (0.260)	0.016 (0.006)	0.008 (0.004)
Scale-free	0.857 (0.029)	0.050 (0.015)	0.013 (0.003)
Random	0.872 (0.090)	0.183 (0.063)	0.077 (0.022)

Table 5.1 - Mean value of I_c and its standard deviation (in brackets) for each network type and size simulated.

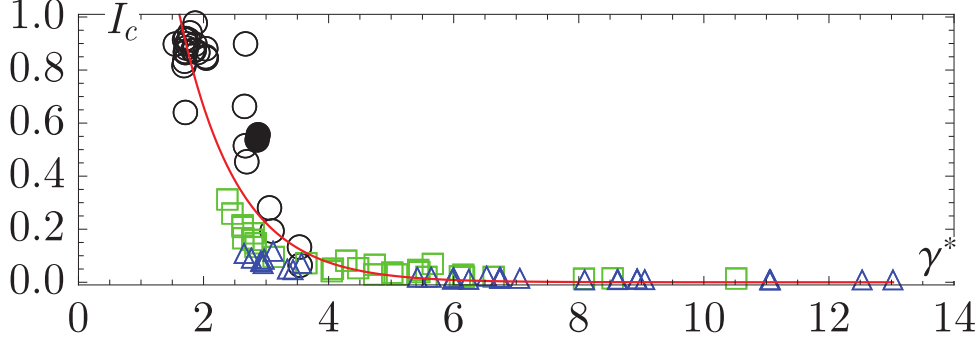


Figure 5.8 - Convergence index I_c versus γ^* . Networks with $N = 10, 50, 100$ nodes are represented as circles, squares and triangles, respectively. The two experiments from Fig. 5.1 are shown as disks. We show in red an exponential fit $f(x) = e^{1.7676 - 1.0894x}$ for the data.

eigenvalues of the coupling graph. Recall that this graph is assumed to be simple and connected. We stress that these eigenvalues express fundamental characteristics of the graph. For instance, γ_2 is related with graph diameter and γ_N with its largest degree size.

We found that the quantity γ^* , defined as the ratio between the maximum eigenvalue and the average of the non-trivial eigenvalues of the Laplacian matrix of the graph, is rather suitable for this purpose. Formally, it is defined as

$$\gamma^* := \gamma_N \left(\frac{1}{N-1} \sum_{k=2}^{N-1} \gamma_k \right)^{-1}.$$

In Fig. 5.8 a correlation plot between I_c and measure γ^* for the correspondent graph is presented. From there, we observe a clear trend indicating that the greater the value of γ^* is, the smaller is the value of I_c . Independently of the network type and size, static regimes of partial synchronization, full synchronization and phase-lock, are typical for values of $\gamma^* \lesssim 3$, like in the experiments from Fig. 5.1. On the other hand, graphs with larger values of this measure yields more irregular dynamics, like

time-dependent periodic and chaotic regimes, as the ones from Fig. 5.7.

5.5 Conclusion

In this work we introduced and studied the DHM, as a Kuramoto-like model of identical oscillators with non-linear coupling. Our main parameter was ε , which governs the coupling nonlinearity strength. It is clear that the most influence of nonlinearity in the coupling is on the hubs which experience strong forcing from many connected oscillators, while less connected nodes may still operate in a linear-coupling regime.

We proved that if this parameter is smaller than the inverse of the square of the maximum vertex degree in the network, then the full synchronized state is stable. Via numerical experiments, we showed that our model can display a variety of other qualitative behaviors of partial synchronization, like stationary phase locking, multistability, periodic order parameter variations, and chaotic regimes. We explored the relative abundance of stationary phase locking regimes under different network topologies. Our statistical analysis with 90 graphs, comprising a variety of network sizes and topologies and vertex sizes, suggests that tree graphs are much less likely to exhibit stationary phase locking in comparison with scale-free or random networks. In addition, this type of behavior becomes rarer if we increase network sizes, irrespective to the network topology. Finally, we also found a good correlation between the ration between the maximum eigenvalue and the average of the non-trivial eigenvalues of the Laplacian matrix of the graph, and the proportion of the repulsion parameter values which yield stationary phase locking. Our simulations show evidence that the greater this measure is, the smaller tend to be presence of stationary phase locking states in the system.

As a future research, we plan to investigate analytical conditions and correlations involving other graph measures related to other forms of synchronization in the model.

6 SYNCHRONIZATION VERSUS NEIGHBORHOOD SIMILARITY

Multi-agents systems from several social or biological applications are often modeled as units having distinct characteristics (SAYAMA; SINATRA, 2015). We are interested in this chapter in how dynamical properties of a system can be affected by the way its non-identical elements select each other to interact.

“Do birds of a feather flock together?”, this question belongs to the article title of Ref. (HAMM, 2000). Its authors explore this matter through a statistical analysis regarding friendship bounds among adolescents. They concluded that some common traits like ethnic identity indeed favor such connections, while others, like substance use, have lower influence. In general, positive or negative assortative matching trends are commonly found in humans (REUSCH et al., 2001) and animals (JIANG et al., 2013).

Considering social networks, there are indeed evidences of like-minded communities (MODANI et al., 2014). Moreover, Ref. (FOWLER; CHRISTAKIS, 2008) reveals that clusters of happy and unhappy people result not just from their tendency to associate with similar individuals, but also from emotion spread. Such scenario is particularly interesting due its parallel with percolation phenomena and dynamic processes on complex networks (PIKOVSKY et al., 2003).

In fact, Nature seems to employ Similar (homophily) or Dissimilar (heterophily) associations under several circumstances and this can be the result of evolutionary adaption (LOZARES et al., 2014).

We investigate ideas inspired by this context within the non-identical phase oscillator Kuramoto model, as in Sec. 3.4. Agents and its connections are represented by the network of coupled oscillators and synchronization emergence plays the role of information transfer. Besides, individual inner characteristics are expressed as their natural frequencies, that is, their travel velocity through the unit cycle when they suffer no external influence.

The weighted graph measure called *total dissonance* is employed. It generalizes the concept of dissonance, in the sense of natural frequency mismatch, from two coupled oscillators (PIKOVSKY et al., 2003). Thus, our neighborhood patterns are obtained via an optimization algorithm, exclusively by permutations of the natural frequencies over the graph nodes. Similar, Neutral and Dissimilar are associated with very small, medium and very high values of *total dissonance*.

These results have already been published at Ref. (FREITAS et al., 2015a), see Ap-

pendix C, so we focus on major results in the present chapter.

Apart from the related material discussed (FREITAS et al., 2015a), Ref. (PINTO; SAA, 2015) is a contemporary reference which strongly relates with our findings. This paper is based on the Ott-Antonsen ansatz (GOTTWALD, 2015), which assumes the oscillators' dynamics in the Kuramoto Model can be written in the form $\theta_i(t) = \alpha(t) \omega_i$. Thus, beginning with this assumption, suitable mainly for large values of coupling parameter, the authors there describe properties that the natural frequencies vector must fulfill in order to maximize the norm of the order parameter, which yield exactly our Dissimilar patterns.

We traced a complementary view. Starting from social and biologically motivated configurations, we provide evidences from numerical experiments of its synchronization properties, for a broader range of coupling parameter values and several network topologies.

In the first section, we discuss the experiment setup; while, the second section contains construction details of Similar, Neutral and Dissimilar patterns via the Simulated Annealing optimization method.

Numerical integration results are shown and discussed in the third section. Finally, conclusions are included in the last section.

6.1 Numerical Experiment Setup

Consider networks of N coupled oscillators, more specifically, the Kuramoto Model (KM)

$$\dot{\theta}_i = \omega_i + \frac{\varepsilon}{d_i} \sum_{j=1}^N A_{ij} \sin(\theta_j - \theta_i), \quad (6.1)$$

for $i = 1, \dots, N$, which is the same formulation as Eq. (3.15) from Sec. 3.4.

Several coupling graphs are studied and all of them are symmetrical and connected, see also Chap. 2. We identify graphs with their adjacency matrix A in this chapter. These graphs follow common complex networks topologies, with N nodes and $E = 4N$ (directed) edges: 4-Regular (N RE), Barabási-Albert (N BA), Erdős-Rényi (N ER) and Watts-Strogatz with rewiring probability 0.25 (N WS). An empirical graph¹ comprising $N = 105$ nodes, $E = 882$ edges and 2 communities is also included (105 CO).

¹The Krebs-Amazon Political Books network: <http://moreno.ss.uci.edu/data.html>

A single version of the empirical (105 CO) and regular networks (50 RE) and (500 RE) are considered. In addition, we perform simulations with 100 samples of each one of the random network topologies, (BA, ER and WS), with $N = 50$ and also with $N = 500$.

Our purpose to perform simulations with multiple coupling graphs is to analyze the pervasiveness of neighborhood patterns influence on synchronization metrics.

About the vector of natural frequencies, for each network size ($N = 50, 105, 500$), we draw a single choice of zero-mean natural frequencies $\omega \in \mathbb{R}^N$ from the uniform distribution over $[-\pi, \pi]$. Also, for each network size, a common initial condition $\theta_0 \in \mathbb{R}^N$ uniformly drawn over the unit circle $[0, 2\pi]$ is used for numerical integration.

Each pair (A, ω) will generate Similar, Neutral and Dissimilar configurations, taking into account only natural frequencies swapping among graph nodes. After the actual construction of such neighborhoods, which is discussed in the next section, numerical integration is performed separately for each of these three patterns.

As described in Sec. 3.7, numerical integration is performed over a sufficiently large time interval to reach permanent regime. Besides, we select increasingly values of coupling parameter $\varepsilon = 0, 0.1, \dots$ up to the critical coupling for phase-locking ε_{PL} .

6.2 Similar, Neutral and Dissimilar neighborhood patterns

Given a fixed coupling graph expressed by its adjacent matrix A of N nodes and a natural frequencies vector $\omega \in \mathbb{R}^N$, the *total dissonance* is defined as

$$\nu_{\text{Total}} := \frac{1}{N} \sqrt{\sum_{i,j=1}^N A_{ij} (\omega_i - \omega_j)^2}. \quad (6.2)$$

Notice that this metric is proportional to the sum of all natural frequencies mismatches $\omega_i - \omega_j$ over the directed edges in the graph². In particular, if oscillator's natural frequencies are close (far) to the ones from their neighborhoods in the coupling graph, then total dissonance ν_{Total} will be low (high).

Since we consider symmetrical and connected coupling graphs, it is straightforward to check that $\nu_{\text{Total}} = 0$ if and only if all oscillator are identical. If we write $\nu_{\text{Total}} =$

² We opt to divide it by network size N instead of quantity of directed edges E to reflect that the more edges a graph contains, the more conflicting pairs of dissonances exist in the network, which yields higher total dissonance. Even so, this constant has no influence regarding the actual SA output.

$\nu_{\text{Total}}(\omega)$, it quantifies how far ω is from a condition where all natural frequencies are identical. Therefore, ν_{Total} encompasses information about the total spreading of ω by summing up individual dissonances over the coupling graph edges.

We use (A, ω) as input for to the optimization process. Then, *Similar* or *Dissimilar* patterns are defined as the outcome of minimization or maximization of the objective function ν_{Total} , respectively. A Simulated Annealing is applied for this purpose and its details are discussed in the below.

The initial pair (A, ω) , without any optimization algorithm, is said to be *Neutral*. This is because for sufficiently large network size N , the total number of permutations $N!$ is so large that probability of randomly drawing a permutation such that ν_{Total} is close to the extreme values is very small. Of course, random permutations are not necessarily far from Similar/Dissimilar extremes. We ensure that our numerical setup indeed satisfied this property later in the text at Fig. 6.2.

Fig. 6.1 illustrates RE, BA and CO graphs with these three neighborhood patterns.

In all cases, Similar patterns placed natural frequencies more homogeneously, with w_i close to the corresponding mean value of its neighborhood. This is visually recognized by the node color transition from blue ($-\pi$) to white (0) and red (π).

One can also observe that this homogeneity arises differently for each topology. Hubs of the BA graph were colored with whiter tones, corresponding to natural frequency distribution closer to zero. In contradiction, the CO graph had positive and negative natural frequency values placed into distinct poles, with hubs inside them close to $\pm\pi/2$ and transition nodes between communities close to zero ω_i .

Dissimilar patterns displayed the reverse behavior. One can notice abundant connections between nodes holding extreme opposite natural frequencies values, negative (red) and positive (blue). In the RE graph, we see nodes with interchanging positive and negative natural frequency values.

Eventually, Neutral patterns can be seeing as a blending between both cases, with no clear ν_{Total} bias.

We employ the Simulated Annealing optimization method (SA) (KIRKPATRICK, 1984) to generate random permutations of the vector ω towards optimal total dissonance ν_{Total} values. More specifically, successive SA iterations are applied using three different strategies for node interchange. Since hubs influence the most ν_{Total} ,

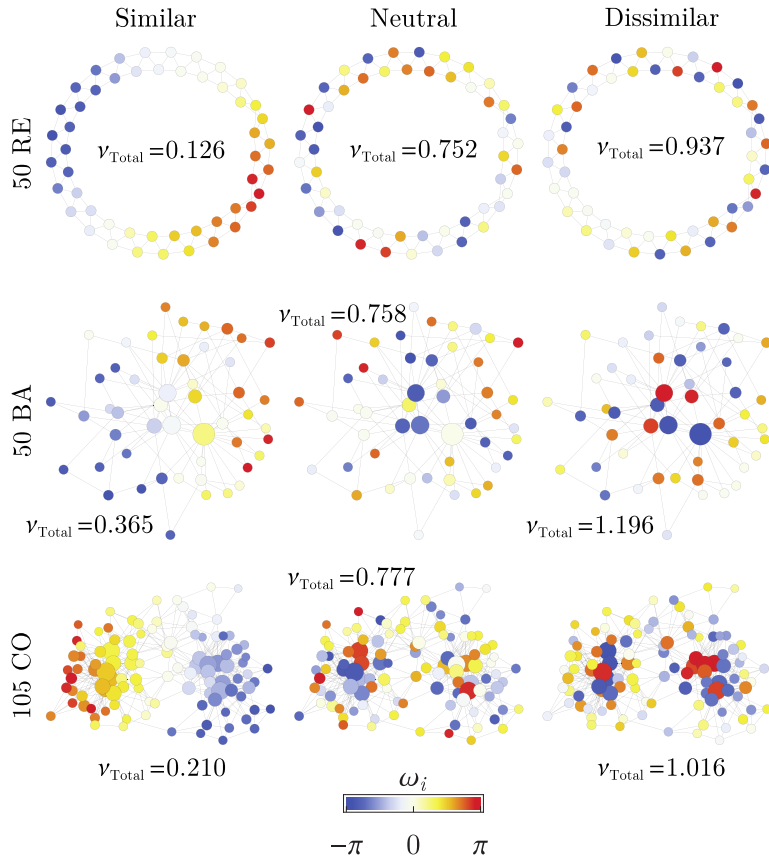


Figure 6.1 - Examples of Similar, Neutral and Dissimilar patterns related to N -nodes graphs following network topology: 4-Regular (50 RE); Barabási-Albert (50 BA); a community graph (105 CO). Vertex color is presented according to its natural frequency ω_i , ranging from $-\pi$ (blue) to π (red); vertex size is proportional to node-degree. The associate total dissonance ν_{Total} is shown.

we first select nodes to be swapped with probability proportional to vertex degree. Then, we chose vertexes to be interchanged within modularity-based community (LANCICHINETTI; FORTUNATO, 2009), as a way to focus the optimization process on relatively detached graph portions. Finally, we elect nodes with equal probability to allow fine adjustments and also to facilitate the escape from local critical points of ν_{Total} .

Fig. 6.2 presents a distribution chart of the total dissonances ν_{Total} obtained for all the network topologies included in this chapter. We see here a clear separation between patterns, since there is no ν_{Total} range overlapping. This an evidence that the optimization technique was sufficiently well tuned, yielding indeed meaningful patterns.

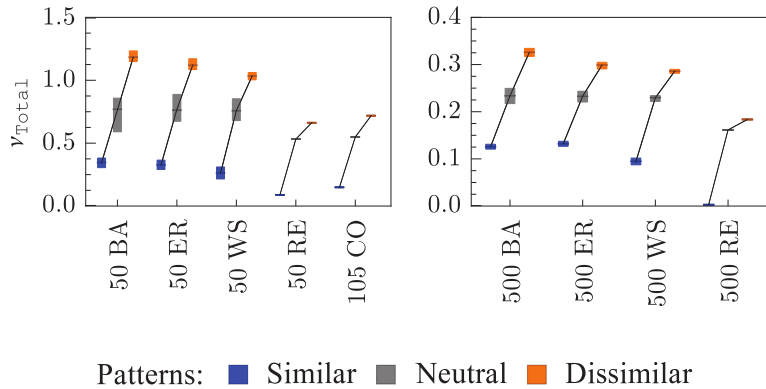


Figure 6.2 - Total Dissonance ν_{Total} distribution chart of different topologies with Similar (Blue), Neutral (Gray) and Dissimilar (Orange) patterns. Data correspond to the single members from categories 50 RE, 500 RE and 105 CO; and 100 different elements for the others. Colored bars indicate the overall range of ν_{Total} obtained, while mean values of each distribution are joined by a black line within each category.

6.3 Simulation Results

It is shown in this section our numerical integration results according to the simulation setup described in Sec. 6.1 with the neighborhood patterns from Sec. 6.2.

We focus on two synchronizations measures from Sec. 3.5 as a function of coupling strength ε : the mean value of partial synchronization index S and the mean value of the norm of the order parameter $\langle R \rangle$ after the transient. The value of these quantifiers is plotted up phase-locking. Since there are 100 different graphs of BA, ER and WS topologies, we rescale the ε time series to the associated mean value critical coupling phase-locking parameter ε_{PL} .

Overall results were qualitatively comparable regarding phase-lock regime: ε_{PL} decreases from Similar, Neutral to Dissimilar patterns; while the corresponding value of the order parameter $R_{\text{PL}} = \langle R \rangle$ tend to increase in the same ordering. Thus, Similar ensembles require higher coupling to achieve phase-locking and even when they do, oscillators are more spread around the unit circle than their counterparts. Neutral patterns required smaller ε_{PL} than Dissimilar ones, except for RE graphs.

For all topologies, higher values of ε_{PL} were measured when N was multiplied by 10. In terms of differences between network topologies, BA, ER, WS graphs exhibited smaller values of ε_{PL} in this other, if we consider Similar or Neutral patterns.

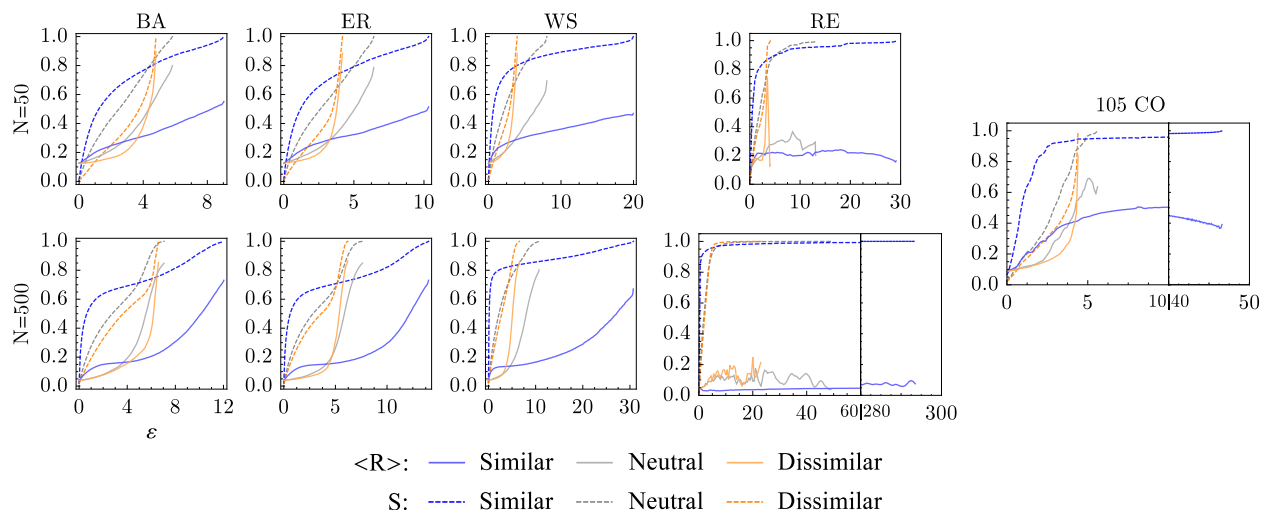


Figure 6.3 - Mean order parameter after transient $\langle R \rangle$ and partial synchronization index S , solid and dashed lines resp., as a function of coupling strength ε for different graph topologies. Average values of all graphs simulated within each category are shown. Similar, Neutral and Dissimilar cases are respectively plotted in Blue, Gray and Orange. Lines are drawn up to ε equal to the respective average critical phase-locking ε_{PL} .

Nevertheless, there is no clear bias between the coupling network topologies and R_{PL} .

We analyze at this point the impact of Similar, Neutral and Dissimilar configuration regarding the emergence of phase-synchronization, that is, for coupling parameters ε much smaller than ε_{PL} .

Except for RE graphs, we see that Similar configurations favor weaker synchronization regimes due to the initial growth of S and $\langle R \rangle$ for small coupling strength ε . However, beyond intermediate values of ε , Dissimilar patterns surpass the Similar ones through an abrupt transition. The Neutral case is in-between these two extremes, closer to the behavior of the Dissimilar pattern.

6.4 Conclusion

We investigated synchronization effects related to Similar, Neutral and Dissimilar neighborhood configuration, which can be also understood respectively as homogeneous, random or heterogeneous non-identical organization patterns.

A parallel of our findings could be made with percolation of conflicting ideas, associating communication and agreement with the emergence of synchronization and

phase-locking, respectively. In Similar scenarios, interaction mostly occurs among people with closely related culture backgrounds. Thus, communication can easily spread locally, but the overall population, which contains diverse members, will hardly find a compromise. On the other hand, when networks contain more heterogeneous neighbors, as in the Neutral and Dissimilar cases, communication demands higher effort to be established. But after that, the whole ensemble is capable to rapidly reach consensus.

In summary, experiments with several network topologies were analyzed and strong numerical trend was found. The Neutral case behaves in general between both extremes, closer to the Dissimilar case. Except for RE networks, under small coupling strength ε , Similar patterns yield larger values of partial synchronization index S , meaning early synchronization ongoing. In contradistinction, Dissimilar ones present smaller values of S , but undergo abrupt increment until phase-locking. Moreover, all networks with Similar patterns required higher values of coupling strength to achieve phase-locking, while Dissimilar patterns converged to regimes closer to full synchronization.

7 CONCLUSION AND OUTLOOK

The focus of this thesis is the emergence of synchronization regimes regarding networks of phase-oscillator, with emphasis to the interplay of dynamics and network topology. It is an interdisciplinary research, aligned with the Cap-INPE post-graduation directives, since it made use of computational modeling, massive numerical simulation and dynamical system theory. We point out the importance of data visualization and statistics tools to interpreted and analyze results too.

In the first part of the text we visited elements of graph theory, including complex network topologies and algorithms to build instances of them. We included after that a discussion about abstract oscillatory systems, its reduction to phase-variables, and an exposition about the simple case of two coupled oscillators. This lead to the main object of study here: the Kuramoto Model (KM). We recall that this model can be considered as a template for a large class of networks of oscillator. Besides, it captures key features from collective behavior.

In this first part, we laid foundation and common terminology for our major contributions (I,II,III). Since our results may be addressed to reader from a variety of backgrounds, it was interesting as a brief reference to these topics too.

Our contribution (I) is a test bed for phase assignment methods introduced at Ref. (FERREIRA et al., 2015): *The discrete complex wavelet approach (DCWA) to phase assignment and a new test bed for related methods*. The test bed consists in embedding trajectories of the KM into a suitable 3d surface, yielding time series with chaotic properties. Such a test bed is devised as a mock for time series of oscillator, where we know reference phase-variables a priori.

This is an innovative technique, because most of the articles introducing new methods for phase assignment employed as reference phases a classic method, which can hinder analyzes. As a possible way to improve the test bed, we could reshape the surface to exhibit a funnel-like geometry like the non-coherent Rössler. Analogous ideas could also be employed to generate time series to mock the ones from neuron networks, including multiple time scales synchronization with bursts and spikes.

Contribution (II) from Ref. (FREITAS et al., 2015a), *Partial synchronization in networks of non-linearly coupled oscillators: The Deserter Hubs Model (DHM)*, was a generalization of the KM. More specifically, we introduced a non-linear coupling scheme based on a local order parameter. This is performed in a way that oscillators

can shift from conformist to contrarian behavior under the influence of sufficiently large number of cohesive neighbors.

We presented a theorem for the DHM stating that if the non-linear coupling parameter is sufficiently small in comparison with the largest node degree, then the full-synchronization in the DHM is stable. Chaos, multistability and periodic order parameter were dynamic regimes observed in the DHM. Another highlight is the existence of full synchronized subgroups under phase-locking regime, which could be adapted for the use of collective motion applications using the KM like components as building blocks. As future research we cite the introduction of more elements in the model towards a more accurate description for deep brain stimulation (POPOVYCH et al., 2005).

Finally, we have contribution (III) from Ref. (FREITAS et al., 2015b), *Synchronization versus neighborhood similarity in complex networks of non-identical oscillators*. The driving question of this work is to analyze the effect of homophily/heterophily, which are phenomena from social/biological areas, into the classic KM framework. To do so, we introduced the total dissonance weighted graph measure to allow the construction of Similar, Neutral and Dissimilar neighborhood patterns. Our numerical experiments with several network topologies showed evidences that: Similar configurations favor the emergence of synchronization, with small values of coupling parameter, while Dissimilar ones undergo an abrupt synchronization for larger values of the coupling parameter. Neutral configurations were a blending between both extremes.

As prospective research, we suggest investigating intermediate values of total dissonance, in between the previously mentioned patterns, and also to expand the study to chaotic oscillator. Moreover, we are already preparing new material about the impact of these neighborhood patterns and delayed communication over transient time.

REFERENCES

- ACEBRÓN, J. A.; BONILLA, L. L.; VICENTE, C. J. P.; RITORT, F.; SPIGLER, R. The Kuramoto model: A simple paradigm for synchronization phenomena. **Rev. Mod. Phys.**, APS, v. 77, p. 1, 137–175, 2005. 4
- ALLIGOOD, K.; SAUER, T.; YORKE, J. **Chaos: an introduction to dynamical systems**. [S.l.]: Springer, 1997. (Chaos: An Introduction to Dynamical Systems). ISBN 9780387946771. 33, 44, 53, 57
- BAIBOLATOV, Y.; ROSENBLUM, M.; ZHANABAEV, Z. Z.; KYZGARINA, M.; PIKOVSKY, A. Periodically forced ensemble of nonlinearly coupled oscillators: from partial to full synchrony. **Phys. Rev. E**, v. 80, n. 4 Pt 2, p. 046211, 2009. 49
- BAKER, C. T. Retarded differential equations. **Journal of Computational and Applied Mathematics**, Elsevier, v. 125, n. 1, p. 309–335, 2000. 36
- BALANOV, A.; JANSON, N.; POSTNOV, D.; SOSNOVTSEVA, O. **Synchronization: from simple to complex**. Springer, 2010. (Springer Series in Synergetics). ISBN 9783642091285. Available from: <http://books.google.com.br/books?id=jUMpYgEACAAJ>. 3, 17, 21
- BARABÁSI, A.-L. **Linked: how everything is connected to everything else and what it means for business, science, and everyday Life**. New York: Plume, 2003. ISBN 0-452-28439-2. 3
- BARABÁSI, A.-L. Scale-free networks: a decade and beyond. **Science**, American Association for the Advancement of Science, v. 325, n. 5939, p. 412–413, 2009. 2
- BARABÁSI, A.-L.; ALBERT, R. Statistical mechanics of complex networks. **Rev. Mod. Phys.**, v. 74, n. 47, 2002. 2, 7, 9, 10, 11, 13
- BARABÁSI, A.-L.; JEONG, H.; NÉDA, Z.; RAVASZ, E.; SCHUBERT, A.; VICSEK, T. Evolution of the social network of scientific collaborations. **Physica A: Statistical mechanics and its applications**, Elsevier, v. 311, n. 3, p. 590–614, 2002. 2
- BARAHONA, M.; PECORA, L. M. Synchronization in small-world systems. **Physical review letters**, APS, v. 89, n. 5, p. 054101, 2002. 2
- BEER, R. D. Dynamical systems and embedded cognition. **The Cambridge handbook of artificial intelligence**, ed, n. 812, p. 856–873, 2014. 3

- BENNET, D. J.; MCINNES, C. R. Pattern transition in spacecraft formation flying using bifurcating potential fields. **Aerospace Science and Technology**, v. 23, n. 1, p. 250 – 262, 2012. ISSN 1270-9638. 35th ERF: Progress in Rotorcraft Research. Available from: <<http://www.sciencedirect.com/science/article/pii/S1270963811001210>>. 2
- BOCCALETTI, S.; LATORA, V.; MORENO, Y.; Chavez, M.; Hwang, D.-U. Complex networks: structure and dynamics. **Physics Reports**, v. 424, p. 175–308, feb. 2006. 3
- BONVIN, N.; PAPAIOANNOU, T. G.; ABERER, K. A self-organized, fault-tolerant and scalable replication scheme for cloud storage. In: **Proceedings of the 1st ACM symposium on Cloud computing**. New York, NY, USA: ACM, 2010. p. 205–216. ISBN 978-1-4503-0036-0. 2
- BROWN, R. E. Impact of smart grid on distribution system design. In: **IEEE. Power and Energy Society General Meeting-Conversion and Delivery of Electrical Energy in the 21st Century, 2008 IEEE**. [S.l.], 2008. p. 1–4. 2
- BSHARY, R.; GINGINS, S.; VAIL, A. L. Social cognition in fishes. **Trends in cognitive sciences**, Elsevier, v. 18, n. 9, p. 465–471, 2014. 3
- BURDEN, R.; FAIRES, J. **Numerical Analysis**. Brooks/Cole, 2005. (Available Titles CengageNOW Series). ISBN 9780534392000. Available from: <<http://books.google.com.br/books?id=wmcL0y2avuUC>>. 31
- CALLAWAY, D. S.; NEWMAN, M. E.; STROGATZ, S. H.; WATTS, D. J. Network robustness and fragility: Percolation on random graphs. **Physical review letters**, APS, v. 85, n. 25, p. 5468, 2000. 27
- CANEDO-RODRIGUEZ, A.; IGLESIAS, R.; REGUEIRO, C. V.; ALVAREZ-SANTOS, V.; PARDO, X. M. Self-organized multi-camera network for a fast and easy deployment of ubiquitous robots in unknown environments. **Sensors**, v. 13, n. 1, p. 426–454, 2012. ISSN 1424-8220. Available from: <<http://www.mdpi.com/1424-8220/13/1/426>>. 2, 3
- CAO, Y.; YU, W.; REN, W.; CHEN, G. An overview of recent progress in the study of distributed multi-agent coordination. **IEEE Transactions on Industrial informatics**, IEEE, v. 9, n. 1, p. 427–438, 2013. 4
- CASTEIGTS, A.; FLOCCHINI, P.; QUATTROCIOCCHI, W.; SANTORO, N. Time-varying graphs and dynamic networks. **International Journal of Parallel,**

Emergent and Distributed Systems, v. 27, n. 5, p. 387–408, 2012. Available from: <<http://dx.doi.org/10.1080/17445760.2012.668546>>. 2

CAVAGNA, A.; CASTELLO, L. D.; GIARDINA, I.; GRIGERA, T.; JELIC, A.; MELILLO, S.; MORA, T.; PARISI, L.; SILVESTRI, E.; VIALE, M. et al. Flocking and turning: a new model for self-organized collective motion. **Journal of Statistical Physics**, Springer, v. 158, n. 3, p. 601–627, 2015. 3

CESSAC, B.; SAMUELIDES, M. From neuron to neural networks dynamics. **The European Physical Journal Special Topics**, Springer, v. 142, n. 1, p. 7–88, 2007. 3

CHEN, J.; WONG, K.; SHUAI, J. Properties of phase locking with weak phase-coherent attractors. **Physics Letters A**, Elsevier, v. 285, n. 5, p. 312–318, 2001. 38, 40

CHUNG, F.; LU, L. The small world phenomenon in hybrid power law graphs. In: **Complex networks**. [S.l.]: Springer, 2004. p. 89–104. 2

CYMERBLIT-SABBA, A.; SCHILLER, Y. Network dynamics during development of pharmacologically induced epileptic seizures in rats in vivo. **The Journal of Neuroscience**, Soc Neuroscience, v. 30, n. 5, p. 1619–1630, 2010. 3

EISENCRAFT, M.; FANGANIELLO, R.; GRZYBOWSKI, J.; SORIANO, D.; ATTUX, R.; BATISTA, A.; MACAU, E.; MONTEIRO, L. H. A.; ROMANO, J.; SUYAMA, R. et al. Chaos-based communication systems in non-ideal channels. **Communications in Nonlinear Science and Numerical Simulation**, Elsevier, v. 17, n. 12, p. 4707–4718, 2012. 36

ERDÖS, P.; RÉNYI, A. On random graphs, i. **Publicationes Mathematicae (Debrecen)**, v. 6, p. 290–297, 1959. 1

EULER, L. Solutio problematis ad geometriam situs pertinentis. **Commentarii academiae scientiarum Petropolitanae**, v. 8, p. 128–140, 1741. 1

FERREIRA, M. T. **Detecção da sincronização de fase em sistemas caóticos por meio da transformada wavelet complexa dual-tree**. 202 p. PhD Thesis (PhD) — Instituto Nacional de Pesquisas Espaciais (INPE), São José dos Campos, 2014-06-24 2014. Available from:

<<http://urlib.net/sid.inpe.br/mtc-m21b/2014/06.10.12.28>>. Access in: 04 ago. 2016. 6, 37, 41

FERREIRA, M. T.; FREITAS, C. B. N.; DOMINGUES, M. O.; MACAU, E. E. The discrete complex wavelet approach to phase assignment and a new test bed for related methods. **Chaos: An Interdisciplinary Journal of Nonlinear Science**, AIP Publishing, v. 25, n. 1, p. 013117, 2015. 5, 37, 43, 71

FIGUEIREDO, D. G.; NEVES, A. F. Equações diferenciais aplicadas; coleção matemática universitária, impa. **Rio de Janeiro**, 2005. 3

FILATRELLA, G.; NIELSEN, A. H.; PEDERSEN, N. F. Analysis of a power grid using a kuramoto-like model. **The European Physical Journal B**, Springer, v. 61, n. 4, p. 485–491, 2008. 26

FILATRELLA, G.; PEDERSEN, N. F.; WIESENFELD, K. Generalized coupling in the Kuramoto model. **Phys. Rev. E**, v. 75, p. 017201, 2007. 49

FOLLMANN, R.; MACAU, E. E.; ROSA, E.; PIQUEIRA, J. R. Phase oscillatory network and visual pattern recognition. **Neural Networks and Learning Systems, IEEE Transactions on**, IEEE, v. 26, n. 7, p. 1539–1544, 2015. 4, 26

FOWLER, J. H.; CHRISTAKIS, N. A. Dynamic spread of happiness in a large social network: longitudinal analysis over 20 years in the framingham heart study. **Bmj**, British Medical Journal Publishing Group, v. 337, p. a2338, 2008. 63

FREEMAN, J.; ZIEMBA, C. M.; HEEGER, D. J.; SIMONCELLI, E. P.; MOVSHON, J. A. A functional and perceptual signature of the second visual area in primates. **Nature neuroscience**, Nature Publishing Group, 2013. 3

FREITAS, C.; MACAU, E.; PIKOVSKY, A. Partial synchronization in networks of non-linearly coupled oscillators: The deserter hubs model. **Chaos: An Interdisciplinary Journal of Nonlinear Science**, AIP Publishing, v. 25, n. 4, p. 043119, 2015. 5, 49, 50, 63, 64, 71

FREITAS, C.; MACAU, E.; VIANA, R. L. Synchronization versus neighborhood similarity in complex networks of nonidentical oscillators. **Physical Review E**, APS, v. 92, n. 3, p. 032901, 2015. 5, 72

FREITAS, C. B. N.; MACAU, E. E. M.; VIANA, R. L. Partial synchronization groups in the kuramoto model: Definitions and numerical experiments. In: **22nd International Congress of Mechanical Engineering (COBEM 2013)**. Ribeirão Preto, SP, Brazil: [s.n.], 2013. p. Submetido. 29

GODSIL, C.; ROYLE, G. **Algebraic Graph Theory**. [S.l.]: volume 207 of Graduate Texts in Mathematics. Springer, 2001. (Graduate Texts in Mathematics., v. 207). 52

GÓMEZ-GARDEÑES, J.; MORENO, Y.; ARENAS, A. Paths to synchronization on complex networks. **Phys. Rev. Lett.**, American Physical Society, v. 98, p. 034101, Jan 2007. Available from:
<<http://link.aps.org/doi/10.1103/PhysRevLett.98.034101>>. 6, 29

GOTTWALD, G. A. Model reduction for networks of coupled oscillators. **Chaos: An Interdisciplinary Journal of Nonlinear Science**, AIP Publishing, v. 25, n. 5, p. 053111, 2015. 64

GRZYBOWSKI, J.; MACAU, E.; YONEYAMA, T. On synchronization in power-grids modelled as networks of second-order kuramoto oscillators. **Chaos: An Interdisciplinary Journal of Nonlinear Science**, AIP Publishing, v. 26, n. 11, p. 113113, 2016. 26

GRZYBOWSKI, J.; MACAU, E. N.; YONEYAMA, T. Isochronal synchronization of time delay and delay-coupled chaotic systems. **Journal of Physics A: Mathematical and Theoretical**, IOP Publishing, v. 44, n. 17, p. 175103, 2011. 36

GURUPRASAD, K.; GHOSE, D. Performance of a class of multi-robot deploy and search strategies based on centroidal voronoi configurations. **International Journal of Systems Science**, v. 44, n. 4, p. 680–699, 2013. Available from:
<<http://www.tandfonline.com/doi/abs/10.1080/00207721.2011.618327>>. 2, 3

HAMM, J. V. Do birds of a feather flock together? the variable bases for african american, asian american, and european american adolescents' selection of similar friends. **Developmental Psychology**, American Psychological Association, v. 36(2), n. 36, p. 209–219, 2000. ISSN 1939-0599. 63

HIRSCH, M.; SMALE, S.; DEVANEY, R. **Differential Equations, Dynamical Systems, and an Introduction to Chaos**. Academic Press, 2004. (Differential equations, dynamical systems, and an introduction to chaos, v. 60). ISBN 9780123497031. Available from:
<<https://books.google.com.br/books?id=INYJuKGmgd0C>>. 20, 21, 24, 27, 32, 38

- HONG, H.; STROGATZ, S. H. Kuramoto model of coupled oscillators with positive and negative coupling parameters: An example of conformist and contrarian oscillators. **Phys. Rev. Lett.**, American Physical Society, v. 106, p. 054102, Feb 2011. Available from: <http://link.aps.org/doi/10.1103/PhysRevLett.106.054102>. 49
- HONG, Y.-W.; SCAGLIONE, A. A scalable synchronization protocol for large scale sensor networks and its applications. **Selected Areas in Communications, IEEE Journal on**, IEEE, v. 23, n. 5, p. 1085–1099, 2005. 36
- HOOVER, W. G.; HOOVER, C. G. Time reversibility, computer simulation, algorithms, chaos. **Nonlinear Dynamics**, World Scientific, v. 1, p. 3, 2012. 34
- HUANG, X.; MI, Y.; QIAN, Y.; HU, G. Phase-locking behaviors in an ionic model of sinoatrial node cell and tissue. **Physical Review E**, APS, v. 83, n. 6, p. 061917, 2011. 3
- IOANNOU, C.; GUTTAL, V.; COUZIN, I. Predatory fish select for coordinated collective motion in virtual prey. **Science**, American Association for the Advancement of Science, v. 337, n. 6099, p. 1212–1215, 2012. 3
- JADBABAIE, A.; MOTEE, N.; BARAHONA, M. On the stability of the kuramoto model of coupled nonlinear oscillators. In: **American Control Conference, 2004. Proceedings of the 2004**. [S.l.: s.n.], 2004. v. 5, p. 4296–4301 vol.5. ISSN 0743-1619. 30, 51
- JEONG, H.; MASON, S. P.; BARABÁSI, A.-L.; OLTVAI, Z. N. Lethality and centrality in protein networks. **Nature**, Nature Publishing Group, v. 411, n. 6833, p. 41–42, 2001. 2
- JEONG, H.; TOMBOR, B.; ALBERT, R.; OLTVAI, Z. N.; BARABÁSI, A.-L. The large-scale organization of metabolic networks. **Nature**, Nature Publishing Group, v. 407, n. 6804, p. 651–654, 2000. 2
- JI, P.; PERON, T. K. D.; MENCK, P. J.; RODRIGUES, F. A.; KURTHS, J. Cluster explosive synchronization in complex networks. **Physical review letters**, APS, v. 110, n. 21, p. 218701, 2013. 3, 17
- JIANG, Y.; BOLNICK, D. I.; KIRKPATRICK, M. Assortative mating in animals. **The American Naturalist**, JSTOR, v. 181, n. 6, p. E125–E138, 2013. 63
- KIRKPATRICK, S. Optimization by simulated annealing: Quantitative studies. **J. Stat. Phy.**, Springer, v. 34, n. 5-6, p. 975–986, 1984. 66

KURAMOTO, Y. Self-entrainment of a population of coupled non-linear oscillators. In: ARAKI, H. (Ed.). **International Symposium on Mathematical Problems in Theoretical Physics**. [S.l.]: Springer Berlin Heidelberg, 1975, (Lecture Notes in Physics, v. 39). p. 420–422. ISBN 978-3-540-07174-7. xii, 4, 30

LANCICHINETTI, A.; FORTUNATO, S. Community detection algorithms: a comparative analysis. **Phys. Rev. E**, APS, v. 80, n. 5, p. 056117, 2009. 67

LEONARD, N. E.; PALEY, D. A.; LEKIEN, F.; SEPULCHRE, R.; FRATANTONI, D. M.; DAVIS, R. E. Collective motion, sensor networks, and ocean sampling. **Proceedings of the IEEE**, IEEE, v. 95, n. 1, p. 48–74, 2007. 3, 4, 35

LETELLIER, C.; ROSSLER, O. E. Rössler attractor. v. 1, n. 10, p. 1721, 2006. revision 91731. 43

LI, J.-S.; ZHANG, X.-D. On the laplacian eigenvalues of a graph. **Linear algebra and its applications**, Elsevier, v. 285, n. 1, p. 305–307, 1998. 9, 31

LIN, Z.; BROUCKE, M.; FRANCIS, B. Local control strategies for groups of mobile autonomous agents. **Automatic Control, IEEE Transactions on**, v. 49, n. 4, p. 622–629, 2004. ISSN 0018-9286. 3

LOZARES, C.; VERD, J. M.; CRUZ, I.; BARRANCO, O. Homophily and heterophily in personal networks. from mutual acquaintance to relationship intensity. **Quality & Quantity**, Springer, v. 48, n. 5, p. 2657–2670, 2014. Available from: <<http://dx.doi.org/10.1007/s11135-013-9915-4>>. 5, 63

MACARTHUR, B. D.; SÁNCHEZ-GARCÍA, R. J.; ANDERSON, J. W. Symmetry in complex networks. **Discrete Applied Mathematics**, v. 156, n. 18, p. 3525 – 3531, 2008. ISSN 0166-218X. Available from: <<http://www.sciencedirect.com/science/article/pii/S0166218X08001881>>. 2

MODANI, N.; NAGAR, S.; SHANNIGRAHI, S.; GUPTA, R.; DEY, K.; GOYAL, S.; NANAVATI, A. A. Like-minded communities: bringing the familiarity and similarity together. **World Wide Web**, v. 17, n. 5, p. 899–919, 2014. ISSN 1573-1413. Available from: <<http://dx.doi.org/10.1007/s11280-013-0261-1>>. 63

MONTOYA, J. M.; SOLÉ, R. V. Small world patterns in food webs. **Journal of theoretical biology**, Elsevier, v. 214, n. 3, p. 405–412, 2002. 2

NAG, S.; SUMMERER, L. Behaviour based, autonomous and distributed scatter manoeuvres for satellite swarms. **Acta Astronautica**, v. 82, n. 1, p. 95 – 109, 2013. ISSN 0094-5765. 6th International Workshop on Satellite Constellation and Formation Flying. Available from: <<http://www.sciencedirect.com/science/article/pii/S0094576512001452>>. 2

NEWMAN, M. E. Communities, modules and large-scale structure in networks. **Nature Physics**, Nature Publishing Group, v. 8, n. 1, p. 25–31, 2012. 2

OLFATI-SABER, R.; MURRAY, R. Consensus problems in networks of agents with switching topology and time-delays. **Automatic Control, IEEE Transactions on**, v. 49, n. 9, p. 1520–1533, 2004. ISSN 0018-9286. 3

PALEY, D.; LEONARD, N.; SEPULCHRE, R.; GRUNBAUM, D.; PARRISH, J. Oscillator models and collective motion. **Control Systems, IEEE**, v. 27, n. 4, p. 89–105, 2005. ISSN 1066-033X. 3, 28, 35

PIKOVSKY, A.; ROSENBLUM, M. Self-organized partially synchronous dynamics in populations of nonlinearly coupled oscillators. **Physica D: Nonlinear Phenomena**, Elsevier, v. 238, n. 1, p. 27–37, 2009. 49

PIKOVSKY, A.; ROSENBLUM, M.; KURTHS, J. **Synchronization: a universal concept in nonlinear sciences**. Cambridge University Press, 2003. (Cambridge Nonlinear Science Series). ISBN 9780521533522. Available from: <<http://books.google.com.br/books?id=FuIv845q3QUC>>. 3, 4, 17, 20, 21, 22, 26, 27, 32, 34, 35, 36, 37, 38, 40, 63

PINTO, R. S.; SAA, A. Optimal synchronization of kuramoto oscillators: A dimensional reduction approach. **Physical Review E**, APS, v. 92, n. 6, p. 062801, 2015. 64

POPOVYCH, O. V.; HAUPTMANN, C.; TASS, P. A. Effective desynchronization by nonlinear delayed feedback. **Phys. Rev. Lett.**, American Physical Society, v. 94, p. 164102, Apr 2005. Available from: <<http://link.aps.org/doi/10.1103/PhysRevLett.94.164102>>. 5, 49, 72

QUILES, M. G.; MACAU, E. E.; RUBIDO, N. Dynamical detection of network communities. **Scientific reports**, Nature Publishing Group, v. 6, 2016. 26

QUIRRENBACH, A. Astronomical interferometry, from the visible to sub-mm waves. **Europhysics News**, v. 32, p. 237–239, nov. 2001. 4

REINISCH, C.; KOFLER, M. J.; KASTNER, W. Thinkhome: A smart home as digital ecosystem. In: IEEE. **Digital Ecosystems and Technologies (DEST), 2010 4th IEEE International Conference on**. [S.l.], 2010. p. 256–261. 2

REKA, A.; BARABÁSI. Statistical mechanics of complex networks. **Rev. Mod. Phys.**, v. 74, p. 47–97, jun. 2002. Available from: <<http://arxiv.org/abs/cond-mat/0106096>>. 3

REUSCH, T. B.; HAÈBERLI, M. A.; AESCHLIMANN, P. B.; MILINSKI, M. Female sticklebacks count alleles in a strategy of sexual selection explaining mhc polymorphism. **Nature**, Nature Publishing Group, v. 414, n. 6861, p. 300–302, 2001. 63

RODRIGUES, F. A.; PERON, T. K. D.; JI, P.; KURTHS, J. The kuramoto model in complex networks. **Physics Reports**, Elsevier, v. 610, p. 1–98, 2016. 26

ROSENBLUM, M.; PIKOVSKY, A. Self-organized quasiperiodicity in oscillator ensembles with global nonlinear coupling. **Phys. Rev. Lett.**, v. 98, p. 064101, 2007. 49

ROSENBLUM, M. G.; PIKOVSKY, A. S.; KURTHS, J. Synchronization approach to analysis of biological systems. **Fluctuation and noise letters**, World Scientific, v. 4, n. 01, p. L53–L62, 2004. 37

SARNE, D.; GROSZ, B. Determining the value of information for collaborative multi-agent planning. **Autonomous Agents and Multi-Agent Systems**, Springer US, v. 26, n. 3, p. 456–496, 2013. ISSN 1387-2532. Available from: <<http://dx.doi.org/10.1007/s10458-012-9206-9>>. 2, 3

SAYAMA, H.; SINATRA, R. Social diffusion and global drift on networks. **Physical Review E**, APS, v. 91, n. 3, p. 032809, 2015. 63

SCHARF, D.; HADAEGH, F.; PLOEN, S. A survey of spacecraft formation flying guidance and control (part 1): guidance. In: **American Control Conference, 2003. Proceedings of the 2003**. [S.l.: s.n.], 2003. v. 2, p. 1733–1739. ISSN 0743-1619. 4

_____. A survey of spacecraft formation flying guidance and control. part ii: control. In: **American Control Conference, 2004. Proceedings of the 2004**. [S.l.: s.n.], 2004. v. 4, p. 2976–2985 vol.4. ISSN 0743-1619. 4

SCHWABEDAL, J. T.; PIKOVSKY, A.; KRALEMANN, B.; ROSENBLUM, M. Optimal phase description of chaotic oscillators. **Physical Review E**, APS, v. 85, n. 2, p. 026216, 2012. 34

SHOUCRI, R. Mathematical aspects of the mechanics of left ventricular contraction. **Modelling in Medicine and Biology**, WIT Press, p. 87, 2011. 3

SORIANO, M. C.; GARCÍA-OJALVO, J.; MIRASSO, C. R.; FISCHER, I. Complex photonics: Dynamics and applications of delay-coupled semiconductor lasers. **Reviews of Modern Physics**, APS, v. 85, n. 1, p. 421, 2013. 36

SPORNS, O.; ZWI, J. D. The small world of the cerebral cortex. **Neuroinformatics**, Springer, v. 2, n. 2, p. 145–162, 2004. 2

STEEN, M. v. **Graph theory and complex networks : an introduction**. Lexington: Maarten van Steen, 2010. ISBN 978-90-815406-1-2. Available from: <<http://opac.inria.fr/record=b1130915>>. 7, 12

STROGATZ, S. H. From kuramoto to crawford: exploring the onset of synchronization in populations of coupled oscillators. **Physica D: Nonlinear Phenomena**, v. 143, n. 1, p. 1 – 20, 2000. ISSN 0167-2789. Available from: <<http://www.sciencedirect.com/science/article/pii/S0167278900000944>>. 4

_____. Exploring complex networks. **Nature**, Department of Theoretical and Applied Mechanics and Center for Applied Mathematics, Cornell University, Ithaca, New York 14853-1503, USA. strogatz@cornell.edu, v. 410, n. 6825, p. 268–276, March 2001. ISSN 0028-0836. Available from: <<http://dx.doi.org/10.1038/35065725>>. 2, 3

_____. **Nonlinear dynamics and chaos: with applications to physics, biology, chemistry, and engineering**. [S.l.]: Westview press, 2014. 32

TANNER, H.; JADBABAIE, A.; PAPPAS, G. Stable flocking of mobile agents part i: dynamic topology. In: **Decision and Control, 2003. Proceedings. 42nd IEEE Conference on**. [S.l.: s.n.], 2003. v. 2, p. 2016–2021 Vol.2. ISSN 0191-2216. 3

TEMIRBAYEV, A. A.; NALIBAYEV, Y. D.; ZHANABAEV, Z. Z.; PONOMARENKO, V. I.; ROSENBLUM, M. Autonomous and forced dynamics of oscillator ensembles with global nonlinear coupling: An experimental study. **Phys. Rev. E**, v. 87, p. 062917, 2013. 49

- TEMIRBAYEV, A. A.; ZHANABAEV, Z. Z.; TARASOV, S. B.; PONOMARENKO, V. I.; ROSENBLUM, M. Experiments on oscillator ensembles with global nonlinear coupling. **Phys. Rev. E**, v. 85, p. 015204, 2012. 49
- THIEBAULT, A.; MULLERS, R. H.; PISTORIUS, P. A.; TREMBLAY, Y. Local enhancement in a seabird: reaction distances and foraging consequence of predator aggregations. **Behavioral Ecology**, ISBE, v. 25, n. 6, p. 1302–1310, 2014. 3
- TRAPPENIERS, L.; FEKI, M. A.; KAWSAR, F.; BOUSSARD, M. The internet of things: the next technological revolution. **Computer**, IEEE Computer Society, v. 46, n. 2, p. 0024–25, 2013. 2
- TURCI, L. F. R.; MACAU, E. E. N. Adaptive node-to-node pinning synchronization control of complex networks. **Chaos: An Interdisciplinary Journal of Nonlinear Science**, AIP, v. 22, n. 3, p. 033151, 2012. 2
- VASSILIEVA, E.; PINTO, G.; BARROS, J. Acacio de; SUPPES, P. Learning pattern recognition through quasi-synchronization of phase oscillators. **Neural Networks, IEEE Transactions on**, IEEE, v. 22, n. 1, p. 84–95, 2011. 4
- VICSEK, T.; ZAFEIRIS, A. Collective motion. **Physics Reports**, Elsevier, v. 517, n. 3, p. 71–140, 2012. 3, 35
- WATTS, D. J.; STROGATZ, S. H. Collective dynamics of ‘small-world’ networks. **nature**, Nature Publishing Group, v. 393, n. 6684, p. 440–442, 1998. 1
- WINFREE, A. T. Biological rhythms and the behavior of populations of coupled oscillators. **Journal of theoretical biology**, Elsevier, v. 16, n. 1, p. 15–42, 1967. 26
- WIRKUS, S. **The dynamics of two coupled van der Pol oscillators with delay coupling**. Cornell University, August, 1999. Available from: <<http://books.google.com.br/books?id=ntRUAAAAYAAJ>>. 31
- WOLF, A.; SWIFT, J. B.; SWINNEY, H. L.; VASTANO, J. A. Determining lyapunov exponents from a time series. **Physica D: Nonlinear Phenomena**, v. 16, n. 3, p. 285 – 317, 1985. ISSN 0167-2789. 34
- WURMAN, P. R.; D’ANDREA, R.; MOUNTZ, M. Coordinating hundreds of cooperative, autonomous vehicles in warehouses. **AI magazine**, v. 29, n. 1, p. 9, 2008. 2

XIE, J.; KELLEY, S.; SZYMANSKI, B. K. Overlapping community detection in networks: The state-of-the-art and comparative study. **Acm computing surveys (csur)**, ACM, v. 45, n. 4, p. 43, 2013. 26

YU, W.; CHEN, G.; CAO, M.; KURTHS, J. Second-order consensus for multiagent systems with directed topologies and nonlinear dynamics. **Systems, Man, and Cybernetics, Part B: Cybernetics, IEEE Transactions on**, IEEE, v. 40, n. 3, p. 881–891, 2010. 3, 17

ZEMANOVÁ, L.; ZHOU, C.; KURTHS, J. Structural and functional clusters of complex brain networks. **Physica D: Nonlinear Phenomena**, Elsevier, v. 224, n. 1, p. 202–212, 2006. 3

ZHANG, Q.; LAPIERRE, L.; XIANG, X. Distributed control of coordinated path tracking for networked nonholonomic mobile vehicles. **Industrial Informatics, IEEE Transactions on**, v. 9, n. 1, p. 472–484, 2013. ISSN 1551-3203. 2

ZHANG, Z.; LONG, K.; WANG, J.; DRESSLER, F. On swarm intelligence inspired self-organized networking: its bionic mechanisms, designing principles and optimization approaches. **Communications Surveys & Tutorials, IEEE**, IEEE, v. 16, n. 1, p. 513–537, 2014. 3

**Appendix 1: The discrete complex wavelet approach to phase assignment
and a new test bed for related methods**



The discrete complex wavelet approach to phase assignment and a new test bed for related methods

Maria Teodora Ferreira, Celso Bernardo Nóbrega Freitas, Margarete O. Domingues, and Elbert E. N. Macau

Citation: *Chaos: An Interdisciplinary Journal of Nonlinear Science* **25**, 013117 (2015); doi: 10.1063/1.4906814

View online: <http://dx.doi.org/10.1063/1.4906814>

View Table of Contents: <http://scitation.aip.org/content/aip/journal/chaos/25/1?ver=pdfcov>

Published by the [AIP Publishing](#)

Articles you may be interested in

[A Robust and NonBlind Watermarking Scheme for Gray Scale Images Based on the Discrete Wavelet Transform Domain](#)

AIP Conf. Proc. **1019**, 565 (2008); 10.1063/1.2953047

[Image Normalization and Discrete Wavelet Transform Based Robust Digital Image Watermarking](#)

AIP Conf. Proc. **963**, 1404 (2007); 10.1063/1.2836017

[Optical Planar Discrete Fourier and Wavelet Transforms](#)

AIP Conf. Proc. **949**, 114 (2007); 10.1063/1.2812286

[Autocorrelation based denoising of manatee vocalizations using the undecimated discrete wavelet transform](#)

J. Acoust. Soc. Am. **122**, 188 (2007); 10.1121/1.2735111

[The shift-invariant discrete wavelet transform and application to speech waveform analysis](#)

J. Acoust. Soc. Am. **117**, 2122 (2005); 10.1121/1.1869732



The discrete complex wavelet approach to phase assignment and a new testbed for related methods

Maria Teodora Ferreira,^{a)} Celso Bernardo Nóbrega Freitas,^{b)} Margarete O. Domingues,^{c)} and Elbert E. N. Macau^{d)}

Laboratory of Computing and Applied Mathematics - LAC,
 Brazilian National Institute for Space Research - INPE, São José dos Campos, Brazil

(Received 26 August 2014; accepted 15 January 2015; published online 26 January 2015)

A new approach based on the dual-tree complex wavelet transform is introduced for phase assignment to non-linear oscillators, namely, the *Discrete Complex Wavelet Approach—DCWA*. This methodology is able to measure phase difference with enough accuracy to track fine variations, even in the presence of Gaussian observational noise and when only a single scalar measure of the oscillator is available. So, it can be an especially interesting tool to deal with experimental data. In order to compare it with other phase detection techniques, a testbed is introduced. This testbed provides time series from dynamics similar to non-linear oscillators, such that a theoretical phase choice is known in advance. Moreover, it allows to tune different types of phase synchronization to test phase detection methods under a variety of scenarios. Through numerical benchmarks, we report that the proposed approach is a reliable alternative and that it is particularly effective compared with other methodologies in the presence of moderate to large noises. © 2015 AIP Publishing LLC.

[<http://dx.doi.org/10.1063/1.4906814>]

In the context of interacting non-linear oscillators, phase synchronization is a remarkable phenomenon in which a certain relation between phases appears, while their amplitudes can remain with no significant correlation.^{1–4} So, investigating phase synchronization requires a clear choice of phase variables, in order to test, for example, if the condition⁵ $\Delta\phi(t) = |\phi_2(t) - \phi_1(t)| < \text{constant}$, where $\phi_1(t)$ and $\phi_2(t)$ are the phases of two systems. Therefore, the process of assigning a phase variable to empirical data, also known as phase detection, is the first step required to reveal a myriad of phase synchronization configurations. This process has been fundamental for instance to study ecological systems,⁶ coupled neurons,^{7,8} geophysical phenomena,⁹ chemical oscillators,¹⁰ lasers,¹¹ plasma physics,^{12,13} and biomedical systems.^{14–19}

avoid instantaneous phase measurement of the involved signals. Instead, average estimations are considered along well-defined temporal or spatial landmarks, or even statistical measures are applied to certain time windows. These are the cases of the following approaches: Poincaré surface of section,²¹ recurrence plots,^{22,23} localized sets,²⁴ and phase diffusion coefficient comparison.²⁵ These techniques, we should emphasize, are effective in providing indications of phase synchronization in the context of the specific situations for which they were designed. Even so, there are several scenarios for which these methods fail to provide an appropriate response, as will be shown with a variety of numerical experiment in this work. One of these situations is when it is necessary to follow over time instantaneous changes in the phase relationship between the systems, especially in the presence of noise. For example, there are technological applications in which information is embedded in the phase difference between systems evolution,²⁶ or if one is interested in following the interaction delay between systems.²⁷

If one assigns phases via linear interpolation between arrival times of the trajectory in a Poincaré section, by construction, this function will be monotonously increasing with time. However, the phase may lose its physical meaning with this imposition. Some epochs of orientation changes are typically expected,²⁸ mainly if one considers noise and/or interacting oscillators.^{5,29} So, we stress that all methods tested in this work allow increasing or decreasing phase values.

In order to choose a phase variable for a non-linear oscillator, one can use, in principle, direct measurements of phase angles on a attractor projection, as well as more sophisticated techniques such as: Hilbert transform,^{1,8} Poincaré surface of section, curvature and recurrence plots,^{22,23} localized sets,²⁴ phase estimation by means of frequency method,^{30,31} short-time Fourier transforms, and Continuous

I. INTRODUCTION

For periodic oscillators, one can easily define its phase by taking a variable parameterizing the motion along the limit cycle, with growth proportional to time. Nevertheless, the concept of phase for oscillatory systems is not unique, in the sense that any choice which corresponds to an increment of 2π at each cycle of the phenomenon in the time-scale that one wishes to analyze is equally valid. See Ref. 20 for further discussions about multi-scale synchronization.

In a more general case, involving chaotic systems, for example, phase assignment can be a nontrivial task. Thus, tests of the phase synchronization between systems normally

^{a)}Electronic address: mteodoraf25@gmail.com

^{b)}Electronic address: cbnfreitas@gmail.com

^{c)}Electronic address: margarete.domingues@inpe.br

^{d)}Electronic address: elbert.macau@inpe.br

Complex Wavelet Transform (CWT) methodologies.^{32–41} In particular, CWT approaches rely on the complex Morlet wavelet to perform phase detection in chaotic time series, yielding good results for coherent systems.^{34,38} So, although it has a high computational cost and may present some interpretation difficulties when applied to large time series, CWT strategies are considered one of the best among the known methods.^{8,42}

Aiming to address this shortcoming of the CWT, we propose a new method to phase assignment, the *Discrete Complex Wavelet Approach—DCWA*, based on the Dual-Tree Complex Wavelet Transform (DT-CWT) to pointwise phase assignment. The DT-CWT is a transform that employs two real Discrete Wavelet Transforms (DWTs). The main qualities of this transform are that it is nearly shift invariant, limited redundancy, and reduced computational cost.^{43–49}

To allow comparisons among different phase detection methodologies, an innovative testbed is also introduced here. We tailored special orbits with non-linear chaotic oscillators characteristics, such that a theoretical phase choice is known *a priori*. This framework was adopted, instead of classical chaotic oscillators like Rössler or Lorenz, to avoid the usage of a canonical method to obtain a reliable phase choice for comparison purposes. As so, we consider first a Kuramoto model with three interconnected oscillators. Empirically choosing their parameters and the interconnect topology, it is possible to simultaneously produce specific synchronization regimes over each pair of oscillators, ranging from unsynchronized to synchronized, with or without phase slips. Then, the phase signals generated for each oscillator in this Kuramoto model is projected into a surface. We refer this type of coordinate transformation as *embedding*. Our more directed accuracy indicator will be the correct detection in the signal, after this transformation, of phase-slips. Three embedding are considered in this paper to emulate different types and properties of non-linear oscillators: with periodic, coherent and non-coherent orbits. Different intensities of Gaussian observational noise were also added to the data.

Using this testbed, we compare the DCWA with some of the most solid methods in the literature: arctangent method, Hilbert transform, and CWT transform. Besides the advantages of only requiring as input a scalar signal and being robust under moderate noise levels, we point out that our technique has an efficient computational performance when applied to large time series. It is applicable to both phase coherent and non-coherent oscillators. Moreover, it can be successfully applied to non-stationary signals and the choice of parameter values to be used is readily available.

A. Related work

Over time, several methods to phase synchronization detection from experimental measures were introduced.^{1,19,22–24,31,34–36,41,50} Also, many other phase detection methods exist in the literature, for example, the synchro-squeezed wavelet transforms⁵¹ (for application, see in Refs. 52–54) which is based on EMD algorithm and the continuous complex wavelet transform. In Ref. 55, it is used proto-phases for phase extraction from the signal, which utilizes

the concepts of the Hilbert and Fourier transform, see Ref. 56. In Ref. 57, the phase description of chaotic oscillators is made by generalizing the concept of standard iso-phases (isochrones) of periodic oscillators.

There are also measures to test the condition of phase synchronization between systems.^{15,19,42,58} For example, in Ref. 19, two synchronization indices are introduced, while in Ref. 15, it is described an application using the mean phase coherence of an angular distribution as a statistical measure. Phase synchronization measures as defined from the Hilbert transform and from the wavelet transform are presented in Ref. 42 and, a method of detecting synchrony in a precise frequency range is shown in Ref. 58. However, to calculate the measures described above, it is first necessary to calculate the phase. Most studies use the Hilbert transform to compute the instantaneous phase (see Refs. 15, 19, 42, and 59) or the continuous complex wavelet transform.^{14,42,58–60} As a valuable alternative, we claim that our DCWA for phase assignment can be applied in association with those techniques to obtain more accurate results.

The remainder of this paper is organized as follows. In Sec. II, we present our proposed approach for phase detection. Then, in Sec. III, we construct the testbed to measure the efficiency of the methods. Finally, in Sec. IV, we present results and analysis of our numerical experiments.

II. METHODOLOGY

It is presented in this section our proposed *Discrete Complex Wavelet Approach (DCWA)* for phase detection, based on DT-CWT. We begin with a brief description of the DT-CWT and then we follow to our proposed DCWA for phase detection. In order to compare our proposed approach, other three traditional methods in the literature for phase assignment are discussed: the arctangent, the Hilbert transform, and the CWT. A description of these methods is include in Appendix A.

A. Dual-tree complex wavelet transform

The DT-CWT is a very carefully constructed transform, from a mathematical and filter bank theory point of view, by Nick Kingsbury in the late 1990s.^{44,45,49} We are interested here in the following main features of this quasi-orthogonal complex multi-scale transform: the low computation cost when compared to continuous wavelet transform with Morlet analyzing wavelet, perfect reconstruction with short support filters, good shift invariance, and limited redundancy. More details about these features are discussed in Refs. 43–49.

This is a transform that employs two real DWTs, for details see Appendix B. The first DWT is associated with a filter bank of the upper tree, and it uses low-pass filters \bar{h}_0 and high-pass filters \bar{h}_1 . It computes the multilevel real wavelet coefficients \bar{d}^j that will be used as the real part of the desired complex wavelet coefficients d^j . The second DWT is associated with a filter bank of the lower tree, and it is composed of low-pass filters h_0 and high-pass filters h_1 . Similarly, it computes the d^j , which contributes to the pure imaginary part of d^j . A schematic representation of the DT-CWT decomposition is illustrated in Appendix C.

In this work, we used first scale decomposition (13, 19)-tap-filters, which are bi-orthogonal and near symmetric. For scales $j > 1$, the filters were used Q-Shift filters with (14, 14)-tap-filters.⁴⁹ The values for these filters are presented in Appendix D.

B. Discrete complex wavelet approach - DCWA

In order to calculate the phase of an oscillator using our DCWA method, the time series x of oscillator 1, i.e., x_1 , is analyzed by the multi-scale DT-CWT. As a result of this transform, we have the time series of the complex wavelet coefficients d^j at each scale j . With these coefficients, the energy E^j at each scale j is calculated as the square of the modulus of complex wavelet coefficients, i.e., $E^j(n) = |d^j(n)|^2$. When, the global wavelet spectrum is computed using $\mathbb{E}^j = \sum_n E^j(n)$. In the next step, the scale J_1 is chosen as the scale of the maximal global energy, i.e., $\mathbb{E}^{J_1} = \max_j \mathbb{E}^j$. Subsequently, the same procedure is applied to the time series x_2 of oscillator 2 and the time series x_3 of oscillator 3. For each oscillator, we have the scale of the maximal global energy J_1, J_2 , and J_3 . When J_1 was different from J_2 and different from J_3 we chose the scale $J = \min(J_1, J_2, J_3)$. This choice was based on the fact that the number of points N in this multi-scale phase time series is proportional to the scale, i.e., $N = 2^{L-J}$, therefore we chose the larger phase time series. Next, we calculated the phase time series of each oscillator, ϕ_1^J, ϕ_2^J , and ϕ_3^J . The phase ϕ_1^J is calculated from the expression

$$\phi_1^J(t) = \text{atan2}(\underline{d}^{J_1}, \bar{d}^{J_1}), \tag{1}$$

wherein atan2 is the arctangent function with two arguments; \underline{d}^{J_1} is the imaginary part of the complex wavelet coefficient in the scale J_1 , and \bar{d}^{J_1} is the real part of the complex wavelet coefficient in the scale J_1 . The atan2 routine is already built in into many different programming languages. Instead of a single variable, like the standard atan , the former function receives as input two real numbers. Thus, it is possible to correctly choose the quadrant of the computed angle. The phases of the other oscillators are calculated in the same way.

Subsequently, with the objective of verifying the phase synchronization, the combination of the phase difference between them was computed as $\Delta\phi_{12}^J = |\phi_2^J - \phi_1^J|$, $\Delta\phi_{13}^J = |\phi_3^J - \phi_1^J|$, and $\Delta\phi_{23}^J = |\phi_3^J - \phi_2^J|$. Finally, the phase synchronization test condition $\Delta\phi_{12}^J(n) < \text{const} < 2\pi$, $\Delta\phi_{13}^J(n) < \text{const} < 2\pi$, and $\Delta\phi_{23}^J(n) < \text{const} < 2\pi$ is evaluated for each combination.

The phase difference using the phase calculated via our DCWA method considering oscillators 1 and 2 are denoted by $\Delta\phi_{12}^w$; between oscillators 1 and 3 are $\Delta\phi_{13}^w$ and between oscillators 2 and 3 are $\Delta\phi_{23}^w$.

III. THE TESTBED

In this section, we begin with the definition of the Kuramoto Model (KM),⁶¹ which is the core of our testbed. It comprises three not identical Kuramoto oscillators interconnected, so different synchronization regimes between each

pairs of oscillators can be obtained by adjusting its parameters. Then, the output signal of the oscillators is transformed through three different embedding. The first one (a) is an embedding from phase variable ϕ into a unit circle in the plane. So, we can illustrate with a simple periodic orbit the usage of the methods. The second one (b) is an embedding from phase variable ϕ to a chaotic curve inside a Möbius strip. Since the Möbius strip has well defined rotation, this embedding plays the role of a coherent attractor. The last one (c) is an embedding from phase variable ϕ to a chaotic curve inside a surface that we call *Double strip*. Since this curve presents larger diffusion coefficient, we may regard it as a non-coherent case. Finally, we explain how the Gaussian observational noise is added to all test sets.

A. Kuramoto model

We assume the following equation for each oscillator $i = 1, \dots, N$ in KM:

$$\dot{\phi}_i = \omega_i - k \sum_{j=1}^N A_{ij} \sin(\phi_i - \phi_j), \tag{2}$$

wherein $\phi_i(t)$ is the phase variable of the i th oscillator, assuming values in the real line \mathbb{R} , which can also be seen as an angle in the unit circumference, $\phi_i(t) \bmod 2\pi$. The natural frequencies, also known as angular frequencies, of the oscillators are given by the parameters $\omega = (\omega_1, \dots, \omega_N) \in \mathbb{R}^N$. The constant $k \in \mathbb{R}$ is the coupling strength, which adjusts the intensity of the influence between neighbor oscillators. The coupling graph, which can be direct of undirected, is expressed by its adjacency matrix $A_{N \times N} = (A_{ij})$, with $A_{ii} = 0$; $A_{ij} = 1$, if oscillator i is influenced by oscillator j ; and $A_{ij} = 0$, otherwise.

It is chosen to our numerical simulation a KM with $N = 3$ oscillators, because we want to show that our discrete complex wavelet approach is able to simultaneously detect fixed phase synchronization and phase slips.⁵ We selected a coupling graph with oscillators 1 and 2 mutually coupled and oscillator 3 acting as a forcing to those oscillators, see Figure 1. The natural frequencies and initial conditions are $\omega = (1.00, 1.05, 1.50)$ and $\phi_0 = (0, \frac{2\pi}{3}, \frac{4\pi}{3})$, respectively. Thus, the coupling strength $k = 0.475$ was empirically fixed to show those two different types of synchronization regimes.

It is used an Adams-Bashforth-Moulton Method for the numerical integration (see Ref. 62), with fixed step size $h = 0.01$. The final integration interval is $t_f = 2 \cdot h \cdot 2$,¹⁸ but its first half is eliminate as a transient time. For simplicity, we present time variables beginning at instant $t = 0$.

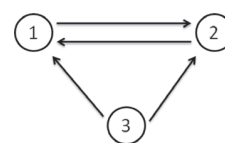


FIG. 1. Schematic representation of the topology connection between oscillators.

B. Kuramoto embeddings

In this subsection, we present the embeddings made in the Kuramoto model and the procedure to add noise.

1. Plane

An embedding in the plan is the simplest, and, this way, we can validate our proposed method with a model that is already described in the variable phase.

To transform the phase variables $\phi \in \mathbb{R}$ of KM (according to Eq. (2)) into the plane $(x, y) \in \mathbb{R}^2$, we simply see ϕ as point in the unit circle with this angle, i.e., we let

$$\begin{aligned} x &= \cos \phi, \\ y &= \sin \phi. \end{aligned} \tag{3}$$

2. Möbius strip

Now, concerning the Möbius strip,⁶³ the usual parametrization is

$$\begin{aligned} x(u, v) &= \left(1 + \frac{1}{2} v \cos\left(\frac{u}{2}\right)\right) \cos u, \\ y(u, v) &= \left(1 + \frac{1}{2} v \cos\left(\frac{u}{2}\right)\right) \sin u, \\ z(u, v) &= \frac{1}{2} v \sin\left(\frac{u}{2}\right), \end{aligned} \tag{4}$$

wherein $0 \leq u \leq 2\pi$ and $-1 \leq v \leq 1$, but we will let $u \in \mathbb{R}$ and set u equal to ϕ from the KM. Figure 2(a) shows schematically two constant lines of this parametrization. Figures 2(b) and 2(c) show one example of this construction increasing the final integration time. Furthermore, we chose v equals to $\cos \phi$, where ϕ is an auxiliary oscillator, with $\dot{\phi}(t) = \tilde{\omega} t$, where $\tilde{\omega}$ is an *irrational natural frequency*. So, the orbits defined like this are dense in the Möbius strip, which can be seen as an analogous of the topological transitivity property for chaotic attractors, as discussed in Ref. 64.

We choose irrational natural frequencies for the auxiliary oscillators as $\tilde{\omega} = (\frac{\sqrt{3}}{10}, \frac{\pi}{20}, \frac{\sqrt{2}}{10})$, which is approximately equal to (0.173, 0.157, 0.141) and ten times slower than the oscillators in the direction of u .

3. Double strip

We introduce here a new Kuramoto embedding, the *Double strip*. Roughly speaking, this surface associates an annulus with a Möbius strip in \mathbb{R}^3 . It was empirically designed to present orbits with higher diffusion constant, which is a feature found, for instance, in the non-coherent Rössler Attractor $\dot{x} = y + z, \dot{y} = x + 0.2y, \dot{z} = 0.2 + xz - 5.7z$ (for information about non-coherent Rössler Attractor look,⁶⁵ and for diffusion constant see Ref. 6).

The position of the oscillator in this figure is defined by a seed $v \in [0, 1]$ and a phase ϕ , so we denote this point by $X(v, \phi)$. Moreover, this map will be defined such that, at every cycle of the oscillator, it returns to a Poincaré Section S given by the line segment joining the origin to $(1, 0, 0)$, more specifically $X(v, 2k\pi) \in S$ for all $k \geq 0$. Thus, we may also define a Poincaré map $P(v_k) = v_{k+1}$ of the successive returns of the orbit to S , since $X(v_k, 2(k+1)\pi) = (v_{k+1}, 0, 0) \in S$.

For a given point in $(v, 0, 0) \in S$, the oscillator will travel in its next cycle $\phi \in [0, 2\pi]$ through a annulus-like surface, that we call *Normal strip*, if $v \in [0, 0.5]$ (as can be seen in Figure 3(a)). Or through a surface similar to a Möbius strip, that we name *Inversion strip*, if $v \in (0.5, 1]$ (as can be seen in Figure 3(b)). Another property of the map X that will be established by construction is that $P(v) = 2v$, if v belongs to the Normal strip; and $P(v) = -2v + 2$, if v belongs to the Inversion strip (as can be seen in Figure 3(d)). For this reason, we can argue that the dynamics in the Double strip is chaotic, since its Poincaré Map P is the Tent Map, which is a classical chaotic discrete map (for more information see Ref. 66).

The position of the oscillator in the Normal strip is given by $X(v, \phi) = f(v, \phi)$ defined by

$$\begin{aligned} f(v, \phi) &:= (1 - \lambda_f(v)) v_0(\phi) + \lambda_f(v) v_{0.5}(\phi), \\ \text{for } (v, \phi) &\in [0, 0.5] \times \mathbb{R}, \end{aligned} \tag{5}$$

where

$$\begin{aligned} v_0(\phi) &= 0.5(\cos \phi, \sin \phi, 0) - (0.5, 0, 0); \\ v_{0.5}(\phi) &= (\phi/(4\pi) + 1)(\cos \phi, \sin \phi, 0) - (0.5, 0, 0); \\ \lambda_f(v) &= 2v. \end{aligned} \tag{6}$$

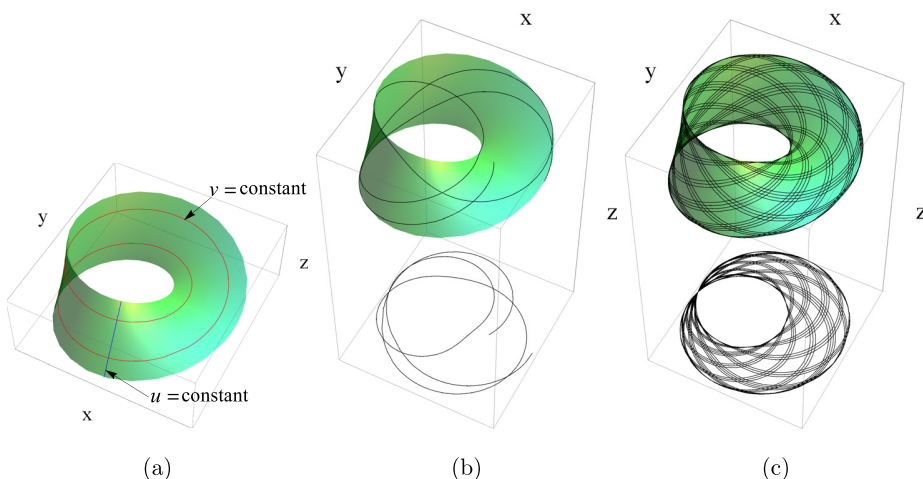


FIG. 2. Möbius strip (a) indicates two curves given by constant lines of its parametrization (according to Eq. (4)); (b) and (c) orbit of an uncoupled oscillator combined with an irrational auxiliary oscillator, with final integration time $t_f = 4\pi$ and $t_f = 40\pi$, respectively. A projection into (x, y) plane is also shown.

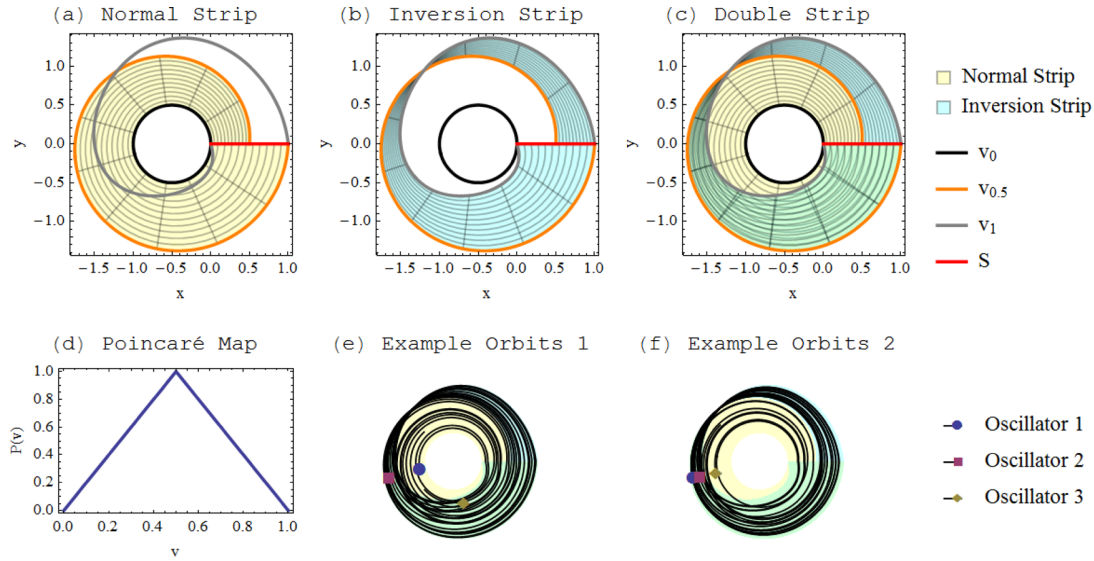


FIG. 3. (a)–(c) Double strip construction scheme. (d) The Poincaré return map considering section S . (e) and (f) Examples of embedded orbits for the Kuramoto model described in Subsection III A. (e) The most common behavior, while (f) display the moment during phase slips when oscillator 3 gives an additional spin and crosses oscillators 1 and 2.

In the other hand, the position of the oscillator in the Inversion strip is given by $X(v, \phi) = g(v, \phi)$ with

$$g(v, \phi) := (1 - \lambda_g(v)) v_{0.5}(\phi) + \lambda_g(v) v_{1.0}(\phi),$$

for $(v, \phi) \in (0.5, 1] \times \mathbb{R}$, (7)

wherein

$$v_{1.0}(\phi) = ((1 + 0.5\gamma(\phi) \cos(\phi/2)) \cos \phi - 0.5, \\ \times (1 + 0.5 \cos(\phi/2) \sin(u), 0.5 \sin(\phi/2));$$

$$\gamma(v) = 0.5(v - \pi)^2 / \pi^2 + 0.5;$$

$$\lambda_g(v) = -1 + 2v. \quad (8)$$

Geometrically, the image of X was designed such that $X([0, 0.5] \times [0, 2\pi])$ interpolates between curves $v_0([0, 2\pi])$ and $v_{0.5}([0, 2\pi])$, which forms the Normal strip; while $X([0.5, 1] \times [0, 2\pi])$ interpolates between $v_{0.5}([0, 2\pi])$ and $v_1([0, 2\pi])$, defining the Inversion strip, see Fig. 3(c). The initial seeds for each of the three oscillators were chosen randomly with uniform distribution over $[0, 1]$.

Figures 3(e) and 3(f) illustrate the Double strip embedding for the Kuramoto model with parameters described in Subsection III A.

4. Applying noise

Through numerical integration, a discrete approximation $\phi(0), \dots, \phi(t_f)$ for the solution of model (2) is computed, according to Subsection III A. Then, one of the embeddings $F(\cdot)$ is applied, yielding $F(\phi(0)), \dots, F(\phi(t_f))$. Let X_i denote the time series of the i th coordinates obtained like this, i.e., $X_i := (F(\phi(0))_i, \dots, F(\phi(t_f))_i)$.

We separately perturb each coordinate with a non-correlated additive noise $X_i + \xi\alpha$, where α is the intensity of the white noise. If $\alpha = 0$, no noise is included. Otherwise, we generate $\xi_\alpha = \alpha \tilde{\sigma} \mathcal{N}$, where $0 \leq \alpha \leq 1$; $\tilde{\sigma}$ is the standard

deviation of X_i ; and \mathcal{N} are random numbers chosen from a standard normal distribution. Noise intensities of $\alpha = 0, 0.10, \dots, 0.90, 1.0$ are explored in this article.

Figures 4(a)–4(c) show the orbits of those three oscillators in the Möbius strip, according to Subsection III A, considering the intensity noise $\alpha = 0$ in (a); (b) $\alpha = 0.10$ and (c) $\alpha = 0.20$.

C. Unwrapping stage

In a first moment, all methods studied here provide wrapped phases, meaning that they are limited to the unit circle $[0, 2\pi)$. Thus, to quantify how many cycles one oscillator overtakes another, we must apply an unwrapping stage. This procedure accumulates the phase difference between consecutive discrete times, with a threshold difference of π to distinguish between phase increments and phase decrements. Thus, it is clearly necessary a sufficiently small discretization time. Otherwise, successive phase differences may become larger than π not because a phase decrement, but due to its fast dynamics in comparison with the sampling rate. Since our fastest uncouple oscillator evolves 0.015 rad per time step (see Sec. III A), in general, this assumption is easily satisfied.

IV. RESULTS

We present now the results of the phase difference assignment considering the Kuramoto model embedding in the plane, in the Möbius strip, and in the Double strip. The theoretical phase difference between oscillators i and j , from the Kuramoto model itself, is denoted by $\Delta\phi_{ij}^k$. The phase difference assigned by the arctangent method, Hilbert transform, the CWT and our DCWA method are denoted by $\Delta\phi_{ij}^t$, $\Delta\phi_{ij}^{hilbert}$, $\Delta\phi_{ij}^{cwt}$, and $\Delta\phi_{ij}^w$, respectively.

We stress that no preliminary filter or denoising procedure is applied before using any of the methods studied.

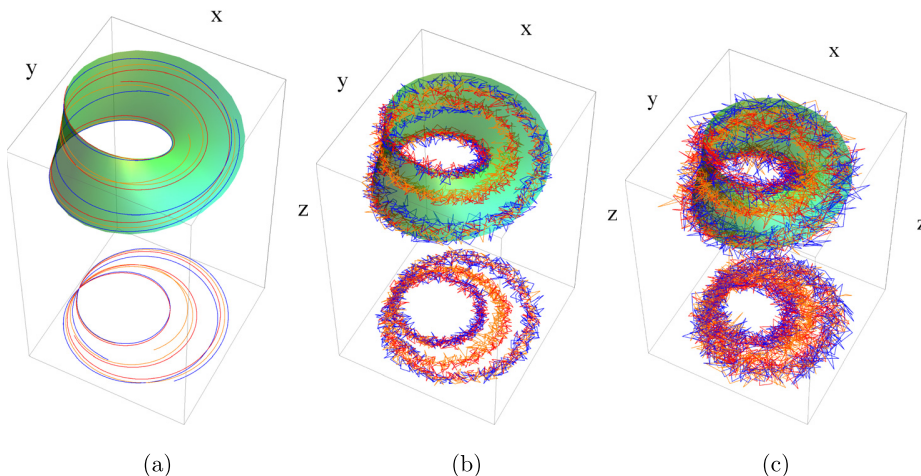


FIG. 4. (a)–(c) Illustrate the orbit of oscillators in the Möbius strip with oscillator 1 in blue, 2 in orange, and 3 in red as described in Subsection III A, considering the intensity noise in (a) $\alpha=0$, (b) $\alpha=0.10$, and (c) $\alpha=0.20$. Projections into (x, y) plane are also shown.

Besides, an unwrapping process to transform consecutive phase points from the unit circle $[0, 2\pi)$ into continuous real values, adding 2π every complete cycle, is applied in all methods according to Sec. III C.

A. Kuramoto model in the plane

We discuss now the results for the Kuramoto model embedded in the plane.

In this case, were found very small values of diffusion coefficient, describing a system with coherent phase, as discussed in Ref. 6. The values for each oscillator are $\tilde{D}_1 = 0.049659$, $\tilde{D}_2 = 0.11847$, and $\tilde{D}_3 = 0.01476$. The average diffusion coefficient is $\tilde{D}_{average} = 0.060963$.

Figure 5 displays (a) the global wavelet spectrum of the Kuramoto model in the plane considering $\alpha=0$. The phase difference between oscillators of the Kuramoto model in the plane without noise ($\alpha=0$) using (b) the theoretical KM, (c) arctangent method, (d) Hilbert transform, (e) the CWT transform, and (f) our DCWA method.

Note that, for oscillators 1 and 2, the scale of maximum energy is $J=9$ and for oscillator 3, the scale of maximum energy is $J=8$, as can be seen in Fig. 5(a). Here, we consider the scale $J=9$ in the phase difference assignment. The scale $J=8$ was also tested and showed similar results when used to scale $J=9$ and, for this reason, there is illustrated here. When we consider the presence of noise, the global wavelet spectrum shows the same scale of maximum energy found when $\alpha=0$ and, therefore is not illustrated here.

Note in Figure 5 that all methods were able to verify phase synchronization between oscillators 1 and 2, as well as the phase slips between oscillators 1 and 3 and oscillators 2 and 3. Note that applying CWT, as can be seen in Fig. 5(e), the detection of phase slips were not as expected given by theoretical KM, as can be seen in Fig. 5(b).

Considering the presence of noise $\alpha=0.10$, $\alpha=0.20$, and $\alpha=0.30$, the results are similar for the three tested methods, arctangent method, Hilbert transform, and our DCWA method, were able to reconstruct the original phase difference of the Kuramoto model. Figure 6 shows the phase difference between oscillators of the Kuramoto model in the plane, with the intensity of noisy $\alpha=0.30$ considering in (a)

the theoretical KM, (b) arctangent method, (c) Hilbert transform, and (d) our DCWA method.

Observed from Figure 6 that even with an intensity of noise $\alpha=0.30$, the three methods were able to reconstruct the original phase difference of the Kuramoto model. Oscillators 1 and 2 are phase synchronized, since their phase difference is almost zero. Oscillator 3 presents phase slips relative to oscillators 1 and 2: for approximately every 500 time units, oscillator 3 gives one additional spin around oscillators 1 and 2, almost like a jump, and then returns to an almost constant phase difference. An important feature was that our discrete complex wavelet approach was much less sensitive to the noise than the arctangent method and Hilbert transform.

However, for further increments in the noise level ($\alpha=0.40$), the arctangent method and the Hilbert transform fail to correctly identify phase slips and phase synchronization, as can be seen in Figures 7(b) and 7(c).

Figure 7 shows the phase difference between oscillators, of the Kuramoto model in the plane, with the intensity of noisy $\alpha=0.40$ considering in (a) the theoretical KM, (b) arctangent method, (c) Hilbert transform, and (d) our DCWA method.

Analysing the results obtained from arctangent method, Figure 7(b), three false phase slips are detected between oscillators 1 and 2, in the interval $t \approx 640$, $t \approx 860$, and $t \approx 1950$. Considering the oscillators 1 and 3 three false phase slips are detected in the interval $t \approx 640$, $t \approx 790$, and $t \approx 885$; and between oscillators 2 and 3 four false phase slips are detected in the interval $t \approx 790$, $t \approx 860$, $t \approx 885$, and $t \approx 1950$.

Note in Figure 7(c), the Hilbert transform fail to correctly identify phase slips and phase synchronization. When we consider the phase difference between oscillators 1 and 2, the Hilbert transform erroneously detects 12 regions of phase slips. Considering the phase difference between oscillators 1 and 3, are erroneously detected 15 phase slips and when we consider oscillators 2 and 3 are erroneously detected 12 phase slips.

The our DCWA method correctly detect phase slips and phase synchronization, as can be seen in Figure 7(d) and compared with the theoretical KM in Figure 7(a). Even for

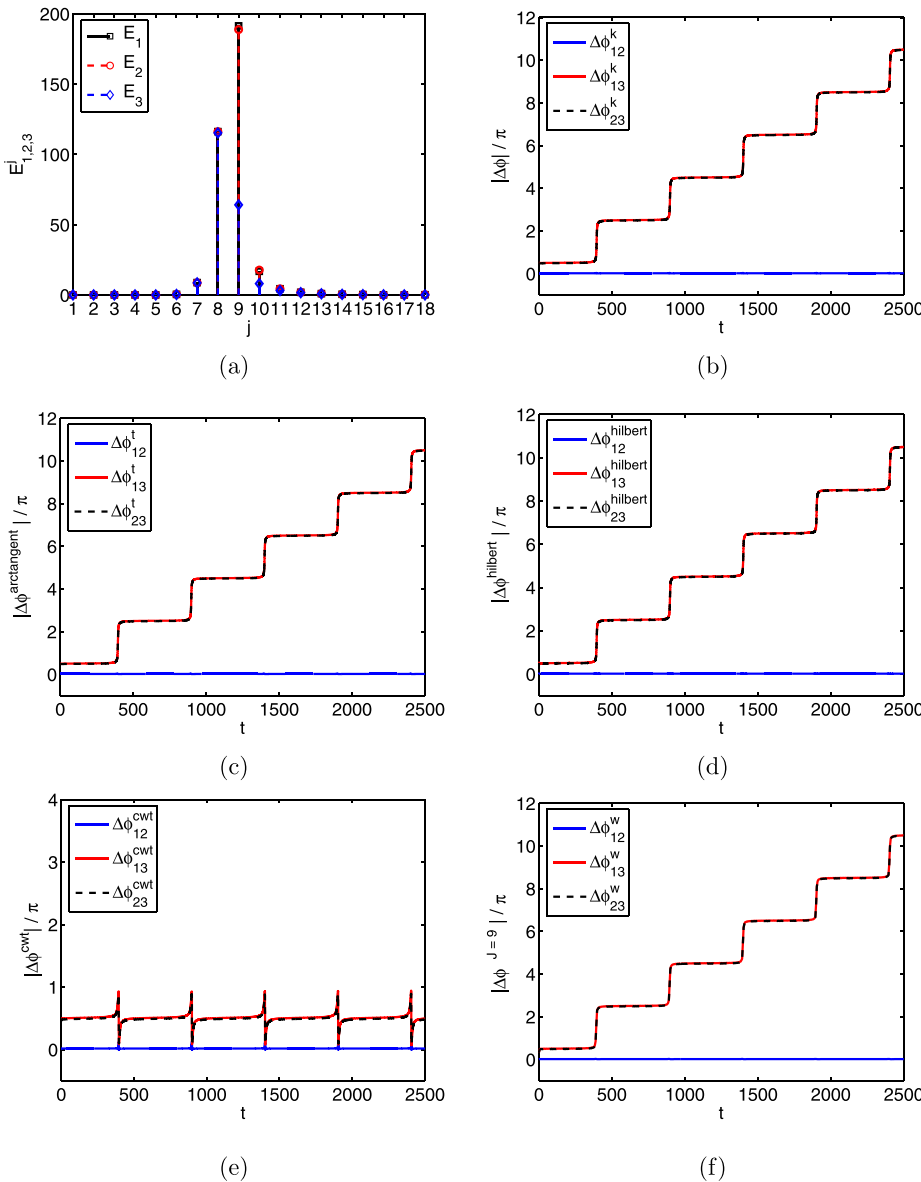


FIG. 5. In (a), the global wavelet spectrum of the Kuramoto model in the plane considering $\alpha = 0$. The phase difference between oscillators when $\alpha = 0$ Kuramoto model plane, considering in (b) the theoretical KM, (c) arctangent method, (d) Hilbert transform, (e) the CWT transform, and (f) our DCWA method.

noise levels up to $\alpha = 2.0$, our DCWA method correctly detect phase slips and phase synchronization, not shown here.

B. Kuramoto model in the Möbius strip

We discuss now the results of the Kuramoto model embedded in a Möbius strip.

In this case, were found small values of diffusion coefficient characterizing a system with coherent phase, as discussed in Ref. 6. The values for each oscillator are $\tilde{D}_1 = 0.18605$, $\tilde{D}_2 = 0.11314$, and $\tilde{D}_3 = 0.013888$. The average diffusion coefficient is $\tilde{D}_{average} = 0.10436$.

Figure 8 displays (a) the global wavelet spectrum of the Kuramoto model in Möbius strip, considering $\alpha = 0$. The phase difference between oscillators of the Kuramoto model in Möbius strip without noise ($\alpha = 0$) using in (b) the theoretical KM, (c) arctangent method, (d) Hilbert transform, (e) the CWT transform, and (f) our DCWA method. Note that, for oscillators 1 and 2, the scale of maximum energy $J = 9$

and for oscillator 3, the scale of maximum energy is $J = 8$, as can be seen in Fig. 8(a). Both results of the global wavelet spectrum are similar with noise, and therefore are not illustrated here. The scale $J = 9$ was used to calculate the phase difference between oscillators. The scale $J = 8$ was also tested and showed similar results when used to scale $J = 9$, and for this reason, there is illustrated here.

Observed from Figures 8(c), 8(d), and 8(f) that the arctangent method, Hilbert transform, and our DCWA method were able to reconstruct the original phase difference of the Kuramoto model (see Figure 8(b)). The CWT transform erroneously detected two phase slips between oscillators 1 and 2. With respect to phase slips occurring between oscillators 1 and 3 and oscillators 2 and 3, the CWT correctly detect the intervals (in time) occurring this phase slips, but do not correctly detect the value thereof, as can be seen in Fig. 8(e).

Despite the fact that our DCWA method presented small perturbations in its results, the method successfully detected the phase slips and phase synchronization. Below, we discuss what can be these perturbations.

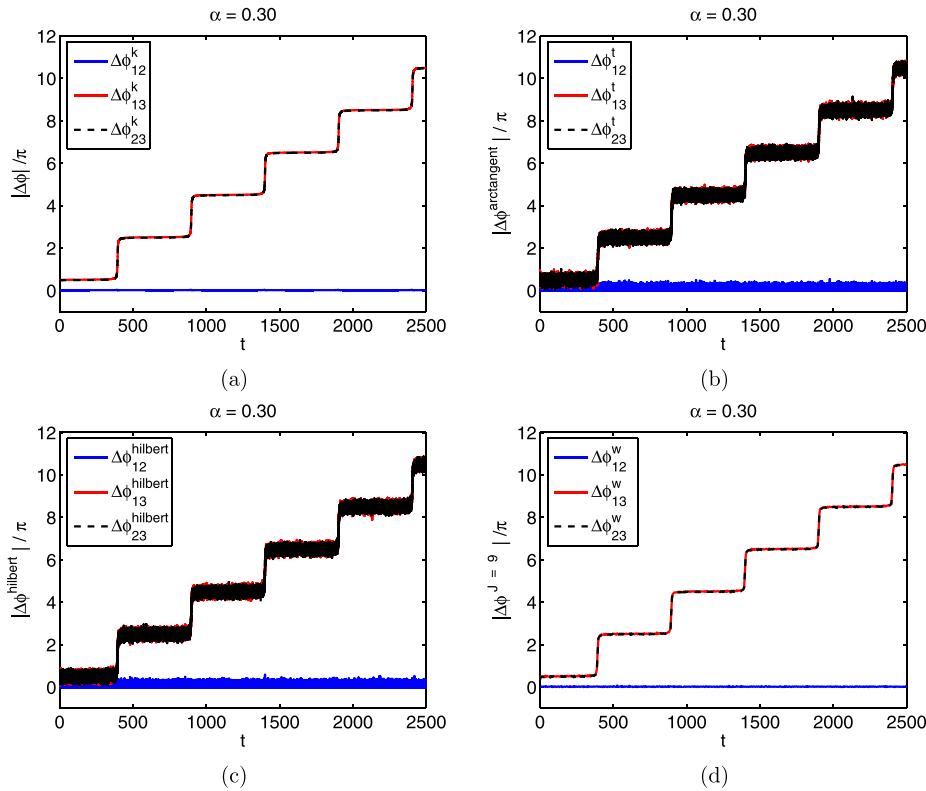


FIG. 6. The phase difference between oscillators, of the Kuramoto model in the plane, with the intensity of noisy $\alpha = 0.30$ considering in (a) the theoretical KM, (b) arctangent method, (c) Hilbert transform, and (d) our DCWA method.

Figure 9(a) displays the zoom of phase difference between oscillators of the Kuramoto model in Möbius strip without noise, $\alpha = 0$, considering our DCWA method. Here, we want to show why the perturbations were found in the

phase difference when applied our DCWA method. In Figures 9(b), 9(c), and 9(d), the interval $t = [1350, 1450]$ of the time series of oscillators 1 and 2; 1 and 3; and 2 and 3 are presented, respectively. Note that in Figure 9(a) the phase

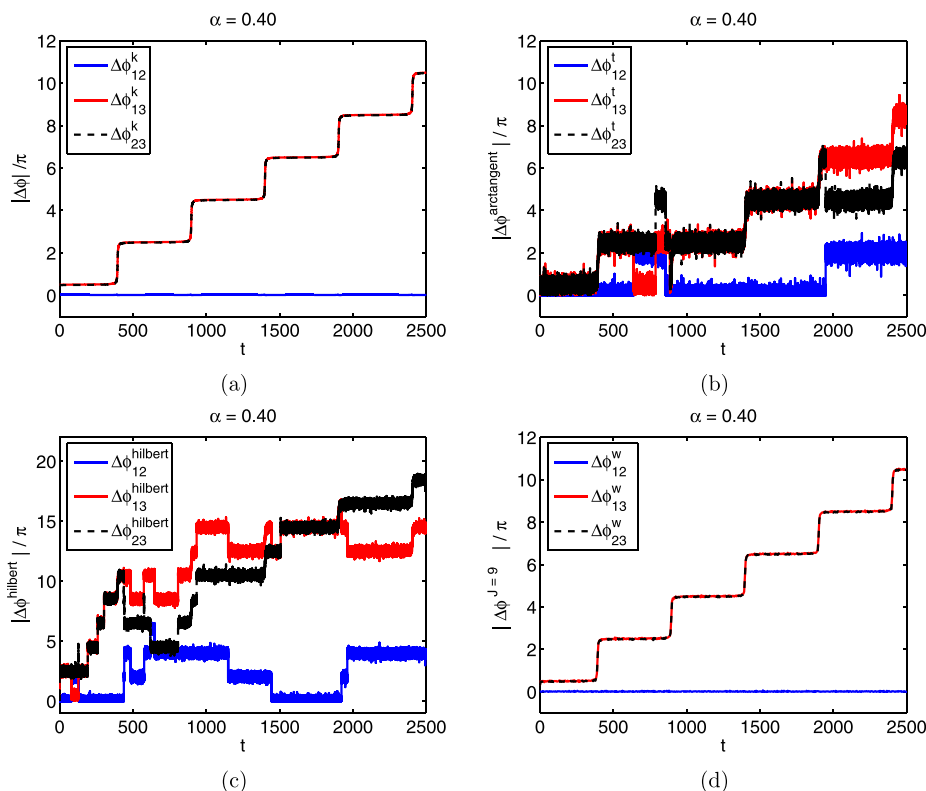


FIG. 7. The phase difference between oscillators, of the Kuramoto model in the plane, with the intensity of noisy $\alpha = 0.40$ considering in (a) the theoretical KM, (b) arctangent method, (c) Hilbert transform, and (d) our DCWA method.

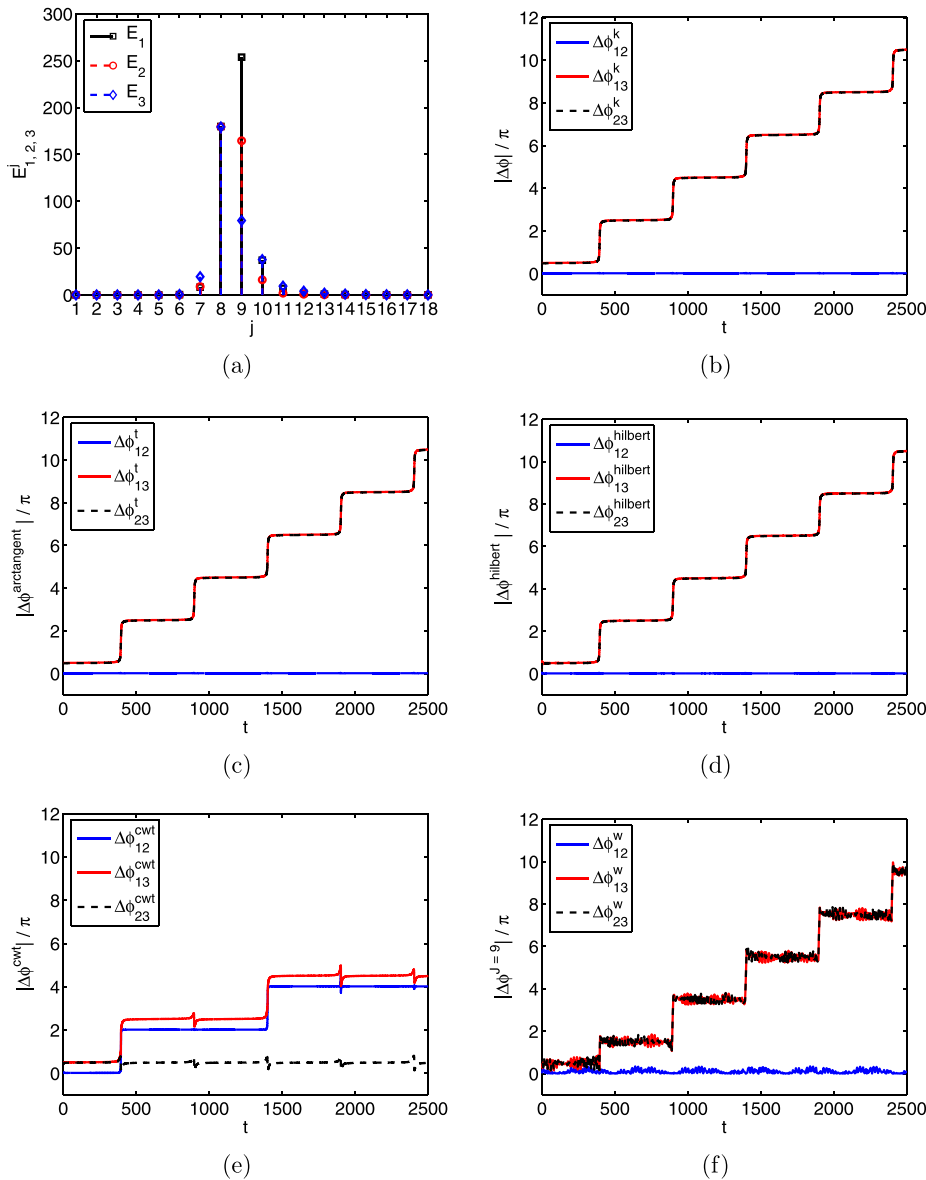


FIG. 8. Results of the Kuramoto model embedded in a Möbius strip. In (a), the global wavelet spectrum and the phase difference between oscillators, considering in (b) the Kuramoto model in the Möbius strip with $\alpha = 0$; (c) arctangent method; (d) Hilbert transform; (e) the CWT transform; and (f) our DCWA method.

difference of oscillators 1 and 2 oscillate around zero and the phase difference of the oscillators 1 and 3 and 2 and 3 oscillate around 3.5 in $t \approx [1350, 1390]$. In the interval $t = [1390, 1410]$, there is a phase slips between oscillators 1 and 3 and 2 and 3, and the phase difference starts to oscillate around 5.5. Observing this interval of the time series of oscillators (see Figures 9(b)–9(d)), we note that the method was able to associate the oscillations found in the phase difference with their delays and/or advances present in time series of oscillators. Note that the other methods were not able to verify this phenomenon, being this one of characteristic of the proposed method.

Considering the presence of noise $\alpha = 0.10$ and $\alpha = 0.20$, the results are similar for the three methods, arctangent method, Hilbert transform, and our DCWA method, were able to reconstruct the original phase difference of the Kuramoto model.

Figure 10 shows the phase difference between oscillators, of the Kuramoto model in Möbius strip, with the

intensity of noisy $\alpha = 0.20$ considering in (a) the theoretical KM, (b) arctangent method, (c) Hilbert transform, and (d) our DCWA method.

Fig. 10 shows that the three methods were able to detect phase synchronization, like in the previous experiment without noise (Figure 8). However, the Hilbert transform erroneously detects a region of the phase slip between oscillators 1 and 3 and oscillators 2 and 3 in the interval $t \approx 490$ (see Figure 10(c)). Nevertheless, our DCWA method was again much less sensitive to the noise than the arctangent method and Hilbert transform.

Increasing the amount of noise for $\alpha = 0.30$, the arctangent method and the Hilbert transform fail to correctly identify phase slips and phase synchronization, as can be seen in Figures 11(b) and 11(c). In this case, these methods detect various phase slips which verifying in the evolution of the time series, the same does not occur. However, the our DCWA method correctly detects phase slips and phase synchronization, as can be seen in Figure 11(d).

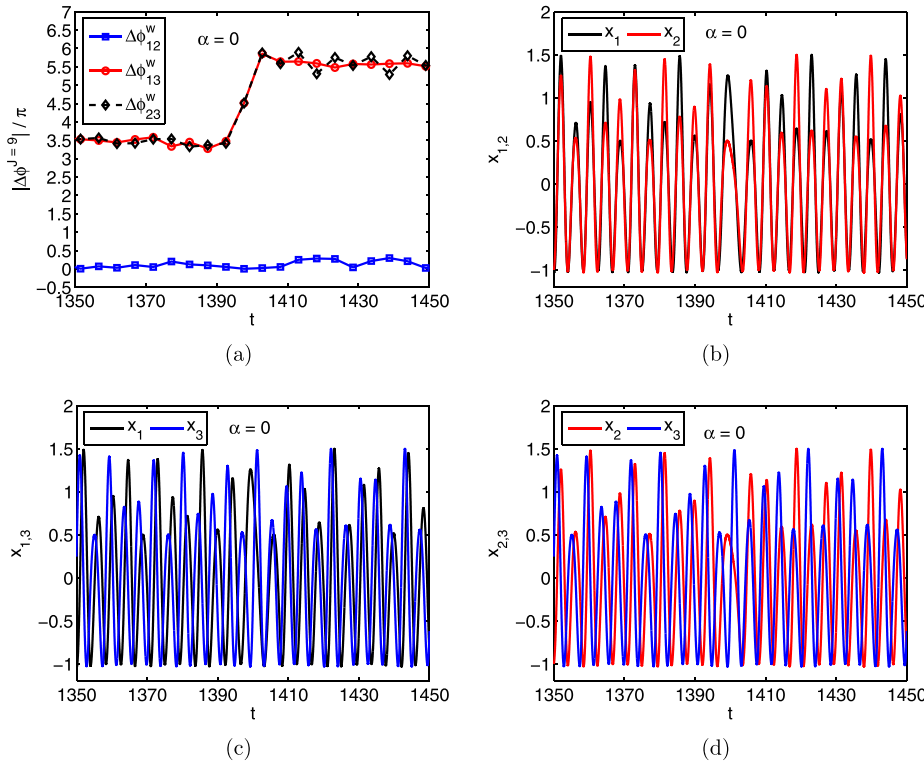


FIG. 9. In (a), the zoom of phase difference between oscillators when $\alpha = 0$ considering our DCWA method and the interval $t = [1350, 1450]$ of the time series of the oscillators in (b) 1 and 2; (c) 1 and 3, (d) 2 and 3.

Figure 11 shows the phase difference between oscillators of the Kuramoto model in a Möbius strip, with intensity of noise $\alpha = 0.30$, considering in (a) the theoretical KM, (b) arctangent method, (c) Hilbert transform, and (d) our DCWA method.

Beyond this level of noise $\alpha = 0.30$, our DCWA method does not detect correctly phase slips and phase synchronization only for $\alpha = 1.6$, not shown here.

C. Kuramoto model in the Double strip

We discuss now the results of the Kuramoto model embedded in a Double strip.

In this case, higher values of diffusion coefficient were found, characterizing a system with more non-coherent phase, as discussed in Ref. 6, The values for each oscillator

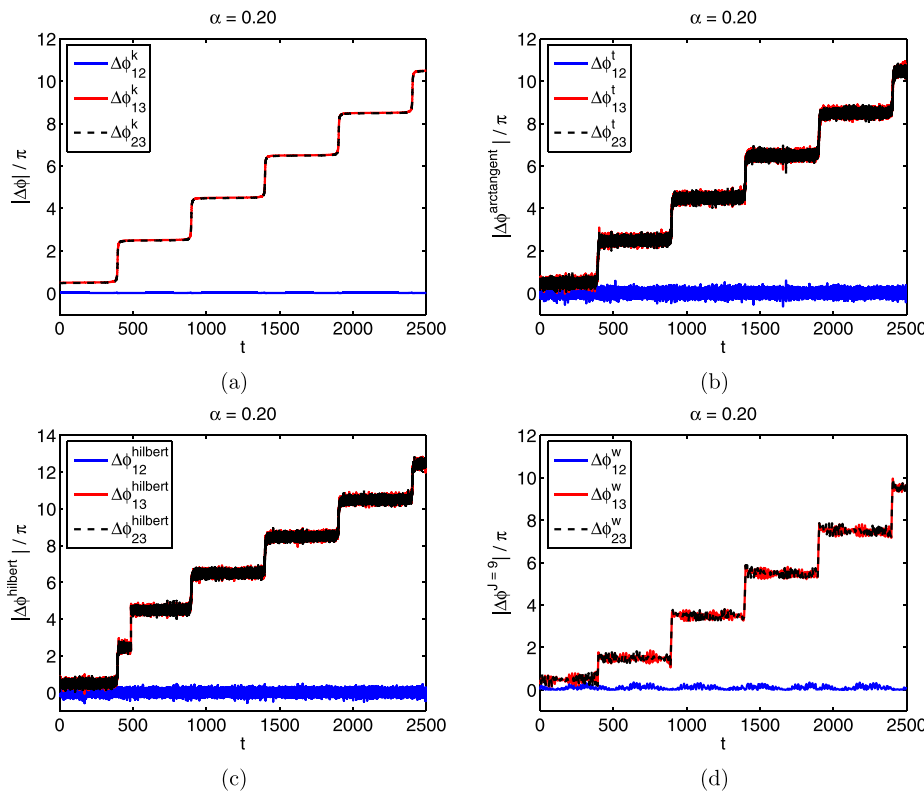


FIG. 10. The phase difference between oscillators, of the Kuramoto model in Möbius strip, with intensity of noise $\alpha = 0.20$, considering in (a) the theoretical KM, (b) arctangent method, (c) Hilbert transform, and (d) our DCWA method.

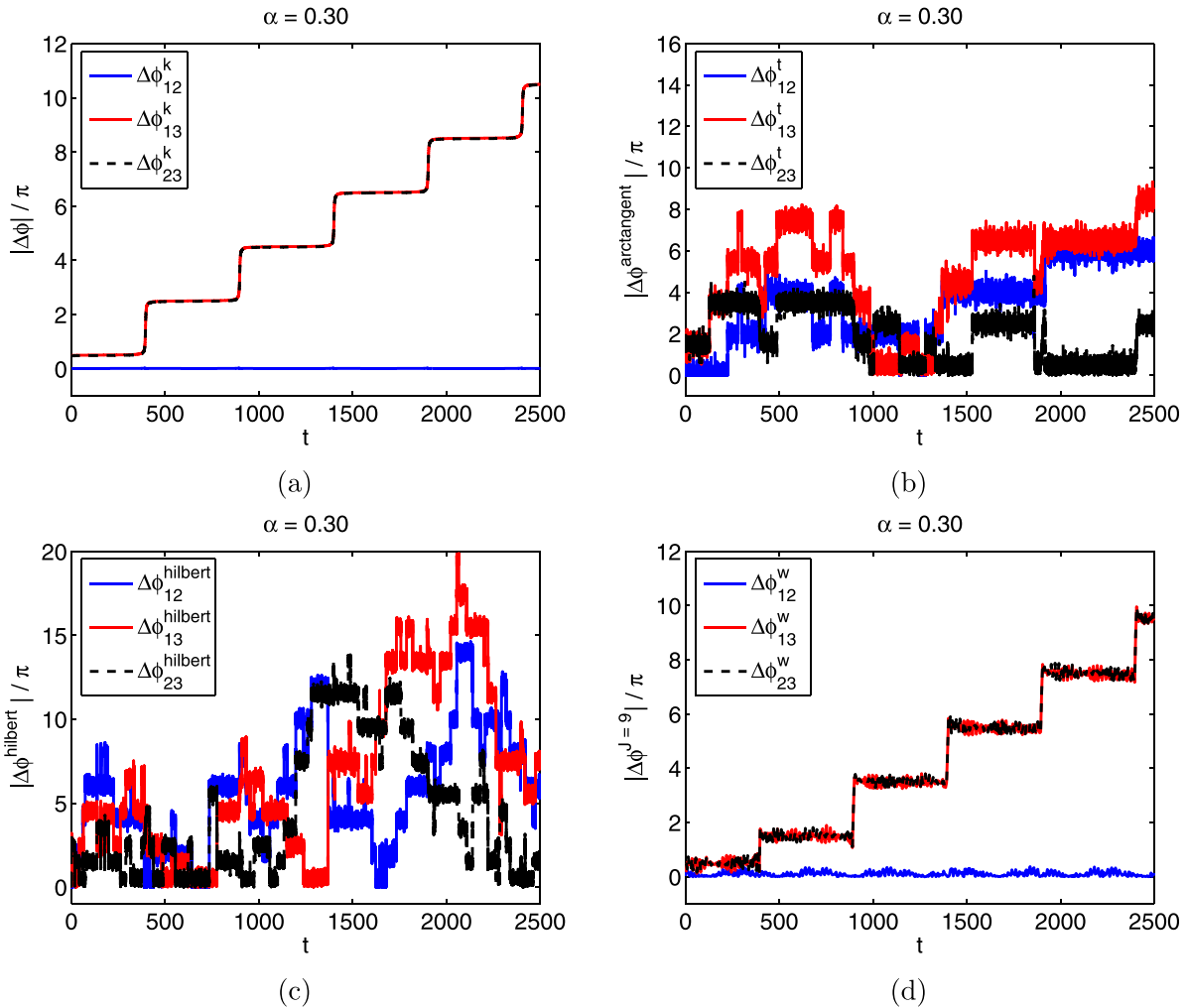


FIG. 11. The phase difference between oscillators, of the Kuramoto model in Möbius strip, with the intensity of noise $\alpha = 0.30$ considering in (a) the theoretical KM, (b) arc tangent method, (c) Hilbert transform, and (d) our DCWA method.

are $\tilde{D}_1 = 0.0894731$, $\tilde{D}_2 = 0.159167$, and $\tilde{D}_3 = 0.11774$. The average diffusion coefficient is $\tilde{D}_{average} = 0.12213$.

Figure 12 shows (a) the global wavelet spectrum and the phase difference between oscillators, considering (b) the Kuramoto model in the Double strip without noise ($\alpha = 0$), (c) arc tangent method, (d) Hilbert transform, (e) CWT transform, and (f) our DCWA method.

Considering without noise and with the presence of noise, from $\alpha = 0.10$ to $\alpha = 2.0$, the method based on arc tangent detects erroneously the phase slips between oscillators 1 and 3 and oscillators 2 and 3 in intervals $t \approx 1550$, $t \approx 1780$, and $t \approx 2210$. The phase slip in intervals $t \approx 1550$ and $t \approx 1780$ are detected erroneously between oscillators 1 and 2.

Considering without noise and with the presence of noise $\alpha = 0.10$ up to $\alpha = 2.0$, the method based Hilbert transform detects erroneously the phase slips between oscillators 1 and 3 and oscillators 2 and 3 in intervals $t \approx 650$, $t \approx 1100$, $t \approx 1550$, $t \approx 1750$, $t \approx 2210$, and $t \approx 2420$. The phase slip in intervals $t \approx 650$, $t \approx 1100$, $t \approx 1550$, $t \approx 1750$, and $t \approx 2420$ are detected erroneously between oscillators 1 and 2.

Applying the CWT, considering without noise, the phase slip in intervals $t \approx 1400$ and $t \approx 2400$, are detected

erroneously between oscillators 1 and 2. Again, the method detects the intervals at which phase slips occur, but does not correctly detect the value of it.

Considering the case without noise and with the presence of noise $\alpha = 0.10$ up to $\alpha = 2.0$, our DCWA method correctly detect the phase slips between oscillators 1 and 3 and oscillators 2 and 3 and the phase synchronization between oscillators 1 and 2.

V. CONCLUSIONS

In this work, we introduced a new approach, based on the DT-CWT, for phase detection. This approach is not just able to measure the phase difference between oscillators, but also presents sensitivity enough to track instantaneous variation in the phase difference between them, even in the presence of noise. The main advantage of our approach is that it can be applied directly to scalar experimental time series. Furthermore, our methodology allows us to work with time series with a large number of points and it presents a low computational cost (order of $2N$, where N is the number of points).

In order to compare different techniques, we also introduced an innovative testbed. Three test sets based on

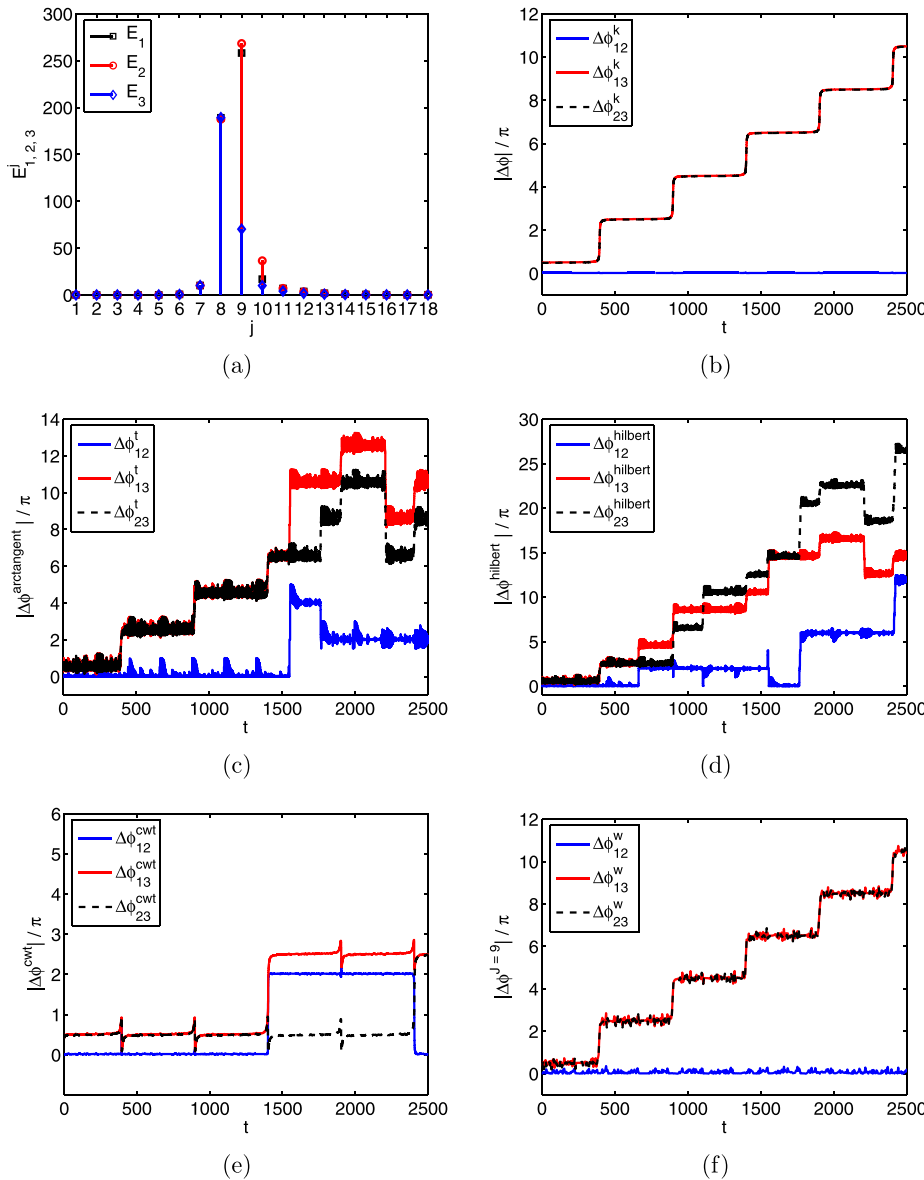


FIG. 12. Results of the Kuramoto model embedded in a Double strip. In (a), the global wavelet spectrum and the phase difference between oscillators, considering in (b) the Kuramoto model in Double strip, without noisy $\alpha=0$ (c) arctangent method; (d) Hilbert transform; (e) CWT transform; and (f) our DCWA method.

embedding of the Kuramoto model in \mathbb{R}^3 were discussed, which are a by-product contribution of this work.

The evaluations reported allow us to claim that our proposed approach, the *Discrete Complex Wavelet Approach—DCWA*, is very effective in accomplish the task for which it was conceived.

The next step in the research will be to extend the method to enable the analysis of energy over time, as well as other filters in the analysis. The applicability of our proposed method will also be tested in chaotic dynamic systems, such as Rössler and Lorenz systems, and sets of experimental data, possibly under different time-scale synchrony regimes.

ACKNOWLEDGMENTS

This work was supported by CAPES, CNPq (Grant Nos. 309667/2013-5, 306828/2010-3, 483226/2011-4, 10571/13-2, and 304582/2010-7) and FAPESP (Grant No. 2011/50151-0).

Nick Kingsbury for giving the algorithm DT-CWT and presented two mini-courses on this subject in the WWlet/CNMAC 2012.

APPENDIX A: OTHER METHODS

1. Arctagent method

It is the most common method for measuring phase if it is possible to project the underlying attractor on a plane so that the projection looks like a smeared limit cycle⁶⁷ with well-defined rotation center.

In this and other similar cases, the phase $\phi(t)$ presents coherent phase and can be measured as the angle in the polar coordinate system on the plane (x, y) , as proposed by Ref. 1, as follows:

$$\phi(t) = \arctan\left(\frac{y}{x}\right). \quad (\text{A1})$$

In the case where the system displays non-coherent phase, the phase can be defined using the projection of the attractor on the plane of the derivative, as proposed in Ref. 68 using the equation

$$\phi(t) = \arctan\left(\frac{\dot{y}}{\dot{x}}\right). \tag{A2}$$

Note that, to calculate the phase using these methods it is necessary to know the two state variables, namely, x and y . But, this is not always available.

In this approach, the arctangent function is defined as a four-quadrant operation.

In this work, the phase difference using the phase calculated via the method based on arctangent function considering oscillators 1 and 2 are denoted by $\Delta\phi_{12}^t$; between oscillators 1 and 3 are $\Delta\phi_{13}^t$ and oscillators 2 and 3 are $\Delta\phi_{23}^t$.

2. Hilbert transform

A consistent way to define the phase for an arbitrary signal is known in signal processing as the analytic signal concept.⁵ This general approach, based on the Hilbert transform (HT), unambiguously gives the instantaneous phase $\phi(t)$ and amplitude $A(t)$ for a signal $s(t)$ via construction of the analytic signal $\zeta(t)$, which is a complex function of time defined as (for details see Ref. 5)

$$\zeta(t) = s(t) + i s_H(t) = A(t) e^{i\phi(t)}. \tag{A3}$$

Here, the function $s_H(t)$ is the HT of $s(t)$

$$s_H(t) = \pi^{-1} P.V. \int_{-\infty}^{\infty} \frac{s(\tau)}{t - \tau} d\tau \tag{A4}$$

where P.V. means that the integral is taken in the sense of the Cauchy principal value.

In this work, the phase difference using the phase calculated via the method based on Hilbert transform considering oscillators 1 and 2 are denoted by $\Delta\phi_{12}^{hilbert}$; between oscillators 1 and 3 are $\Delta\phi_{13}^{hilbert}$ and oscillators 2 and 3 are $\Delta\phi_{23}^{hilbert}$.

3. Continuous wavelet transform

The CWT is a tool that allows to decompose the time series into different components of frequencies. This transform considers that the translation and scale parameters are continuous, and transforms a one-dimensional time series (time) in a two-dimensional representation (time, scale) that can be highly redundant.

The CWT in $L^2(\mathbb{R})$ of a time series $f(t)$ can be defined as

$$\mathcal{W}_n^s(t) = \frac{1}{\sqrt{s}} \int_{-\infty}^{\infty} f(t) \psi^* \left(\frac{t-n}{s} \right) dt, \tag{A5}$$

wherein $s, n \in \mathbb{R}, s \neq 0$, $*$ denotes the complex conjugate and the term $\frac{1}{\sqrt{s}}$ is a normalization factor of the signal energy.

The wavelet spectra, also called scalograms, represent the squared amplitudes of the module of wavelet coefficients, which can be interpreted as the distribution of signal energy in time t by its scale.⁶⁹

The global wavelet spectrum is the time integration of scalogram, or

$$S_\psi(s) = \int \mathcal{W}_n^s(s, n) dt. \tag{A6}$$

The Morlet wavelet consists of a plane wave modulated by a Gaussian function that is expressed by

$$\psi^{Morlet}(t) = e^{-i\omega_0 t} e^{-t^2/2}, \tag{A7}$$

wherein ω_0 is a non dimensionless frequency. This wavelet function is a complex function, which allows to analyze the phase and the modulus of the decomposed signal.

In this work, the phase difference using the phase calculated via the method based on CWT considering oscillators 1 and 2 are denoted by $\Delta\phi_{12}^{cwt}$; between oscillators 1 and 3 are $\Delta\phi_{13}^{cwt}$ and oscillators 2 and 3 are $\Delta\phi_{23}^{cwt}$.

APPENDIX B: DISCRETE WAVELET TRANSFORM

The DWT presents four important attractive characteristics, namely, good compression of signal energy, perfect reconstruction with short support filters, no redundancy, and very low computation cost (order N operations).⁴⁹ As this transform is a real transform, we cannot use it to compute the phase. However, it will be used here as a tool to compute the DT-CWT.

The DWT is implemented in discrete values of scale j and localization n , and provides a time-scale analysis of any finite energy signal x , where $j, n \in \mathbb{Z}$. Mathematically, the signal x can be decomposed in terms of basis functions, as for instance, the scale function φ . However, we can represent this signal also in a multi-scale way using a multi-resolution analysis (MR) tool.

A MR is constructed by using embedded spaces $V^j \supset V^{j+1}$ that have as basis functions φ^j , which are a Riez basis; the union of these spaces are $L^2(\mathbb{R})$; the intersection of these spaces is zero; their functions have scalability proprieties. The difference between two spaces V^j and V^{j+1} is the detail space, where the wavelet functions are Riesz basis, as described in detail in Refs. 69 and 70. Thus, we can represent x in a multi-scale way considering just one scale function φ and its associated wavelet functions ψ as

$$x(t) = \sum_{n \in \mathbb{Z}} c_n^j \varphi_n^j(t) + \sum_{j, n \in \mathbb{Z}} d_n^j \psi_n^j(t), \tag{B1}$$

wherein c_n^j are scale coefficients, $c_n^j = \int x(t) \varphi_n^j(t) dt$, and d_n^j are wavelet coefficients $d_n^j = \int x(t) \psi_n^j(t) dt$. These coefficients are calculated by using a very efficient, linear complexity algorithm based on convolutions of the analyzed signal x with a discrete-time low-pass filter h_0 and a high-pass filter h_1 with downsampling operations $\downarrow 2$. This is called the Mallat algorithm or Mallat-tree decomposition^{69,70} and it is the DWT. The c_n^j and d_n^j are associated to h_0 and h_1 . Moreover, they have a scale relation

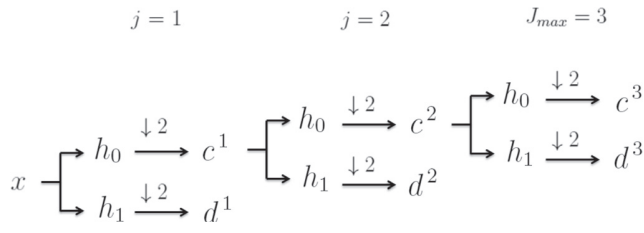


FIG. 13. Scheme of the DWT decomposition of the signal x in three scales, $j=1, 2$ and $j=3$).

$$c_n^j = \sum_{k \in \mathbb{Z}} h_0(k) c_{n-k}^{j-1}, \quad d_n^j = \sum_k h_1(k) c_{n-k}^{j-1},$$

where one possibility is to choose $h_1(k) = (-1)^k h_0(1-k)$. Therefore, the following relations can be obtained:

$$\varphi_n^j(t) = \sum_n h_0(n) \varphi_n^{j-1}(t), \quad \psi_n^j(t) = \sum_n h_1(n) \varphi_n^{j-1}(t).$$

Figure 13 shows a scheme of the DWT decomposition in three scales of the real signal x . The signal is analyzed independently and simultaneously by using the filters h_0 and h_1 and then decimated by a factor of 2 (denoted as $\downarrow 2$), generating two 1-scale coefficients given, respectively, by the following convolutions:

$$c^1 = [x * h_0] \downarrow 2, \quad d^1 = [x * h_1] \downarrow 2.$$

Note that for $j=2$ and $j=3$ we have

$$c^2 = [h_0 * c^1] \downarrow 2, \quad d^2 = [h_1 * c^1] \downarrow 2, \\ c^3 = [h_0 * c^2] \downarrow 2, \quad d^3 = [h_1 * c^2] \downarrow 2.$$

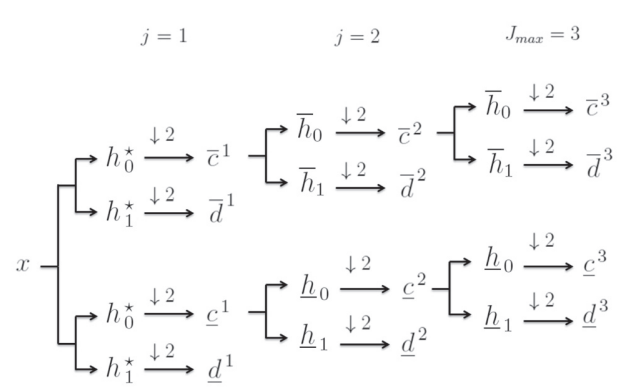


FIG. 14. Schematic multi-scale representation of three scales DT-CWT decomposition of the real time series x in three levels, where the filters h_0^* and h_1^* are considered in the level $j=1$. In levels $j=2$ and $j=3$, the filters of the upper and lower tree are \bar{h}_0, \bar{h}_1 and $\underline{h}_0, \underline{h}_1$, respectively.

APPENDIX C: DT-CWT DECOMPOSITION

A schematic representation of the DT-CWT decomposition is illustrated in Fig. 14. The real time series x is decomposed in $J_{max}=3$ scales, i.e., $j=1, j=2, j=3$, and the notation $*$ is included in the first scale filters, i.e., h_0^* and h_1^* .

In Ref. 49, it is shown that the implementation of the DT-CWT requires that the first scale of the dual-tree filter bank be different from the succeeding scales. A schematic representation of the DT-CWT decomposition is illustrated in Fig. 14. The real time series x is decomposed in $J_{max}=3$ scales, i.e., $j=1, 2$ and 3 , and the notation $*$ is included in the first scale filters, i.e., h_0^* and h_1^* .

TABLE I. Non-zero near-symmetric (13, 19) and Q-Shift (14, 14)-tap filter coefficients. Credits N. G. Kingsbury, Appl. Comput. Harmonic Anal. 10, 234–253 (2001). The coefficients are multiplied by 10^{-2} .

n	Near-symmetric		Q-shift			
			Upper tree		Lower tree	
	h_0^*	h_1^*	\bar{h}_0	\bar{h}_1	\underline{h}_0	\underline{h}_1
1	-0.17578	-7.0626×10^{-5}	0.32531	-0.45569	-0.45569	-0.32531
2	0	0	-0.38832	0.54395	-0.54395	-0.38832
3	2.22660	0.13419	3.46600	1.70250	1.70250	-3.46600
4	-4.68750	-0.18834	-3.88730	-2.38250	2.38250	-3.88730
5	-4.82420	-0.71568	-11.72000	-10.67100	-10.67100	11.72000
6	29.68800	2.38560	27.53000	-1.18660	1.18660	27.53000
7	55.54700	5.56430	75.61500	56.88100	56.88100	-75.61500
8	29.68800	-5.16880	56.88100	-75.61500	75.61500	56.88100
9	-4.82420	-29.9760	1.18660	27.53000	27.53000	-1.18660
10	-4.68750	55.9430	-10.67100	11.72000	-11.72000	-10.67100
11	2.22660	-29.9760	2.38250	-3.88730	-3.88730	-2.38250
12	0	-5.16880	1.70250	-3.46600	3.46600	1.70250
13	-0.17578	5.56430	-0.54395	-0.38832	-0.38832	0.54395
14		2.38560	-0.45569	-0.32531	0.32531	-0.45569
15		-0.71568				
16		-0.18834				
17		0.13419				
18		0				
19		-7.0626×10^{-5}				

APPENDIX D: DUAL-TREE FILTERS

In this work, we have chosen the Q-shift (14, 14) tap-filters where scales $j > 1$, which has provided a group delay of either 1/4 or 3/4 of a sample period, while also satisfying the usual 2-band filterbank constraints of no aliasing and perfect reconstruction.⁷¹ For the first scale (13, 19) tap-filters were used, which are bi-orthogonal and near symmetric.

Table I presents the analysis filters coefficients used in this work.

- ¹M. G. Rosenblum, A. S. Pikovsky, and J. Kurths, "Phase synchronization of chaotic oscillators," *Phys. Rev. Lett.* **76**, 1804–1807 (1996).
- ²M. G. Rosenblum, A. S. Pikovsky, and J. Kurths, "From phase to lag synchronization in coupled chaotic oscillators," *Phys. Rev. Lett.* **78**, 4193–4196 (1997).
- ³M. G. Rosenblum, A. S. Pikovsky, J. Kurths, C. Schäfer, and P. A. Tass, "Phase synchronization: From theory to data analysis," in *Handbook of Biological Physics* (Elsevier, New York, 2001), Vol. 4, pp. 279–321.
- ⁴M. G. Rosenblum, A. S. Pikovsky, J. Kurths, G. V. Osipov, I. Z. Kiss, and J. L. Hudson, "Locking-based frequency measurement and synchronization of chaotic oscillators with complex dynamics," *Phys. Rev. Lett.* **89**, 264102 (2002).
- ⁵A. S. Pikovsky, M. G. Rosenblum, and J. Kurths, *Synchronization: A Universal Concept in Nonlinear Sciences* (Cambridge, New York, 2003).
- ⁶B. Blasius and L. Stone, "Chaos and phase synchronization in ecological systems," *Int. J. Bifurcation Chaos* **10**, 2361–2380 (2000).
- ⁷J. Fell and N. Axmacher, "The role of phase synchronization in memory processes," *Nat. Rev. Neurosci.* **12**, 105–118 (2011).
- ⁸M. L. V. Quyen, J. Foucher, J. P. Lachaux, E. Rodriguez, A. Lutz, J. Martinerie, and F. J. Varela, "Comparison of Hilbert transform and wavelet methods for the analysis of neuronal synchrony," *J. Neurosci. Methods* **111**, 83–98 (2001).
- ⁹E. Lauro, S. Martino, M. Falanga, and S. Petrosino, "Synchronization between tides and sustained oscillations of the hydrothermal system of campi flegrei (Italy)," *Geochem. Geophys. Geosyst.* **14**, 2628–2637 (2013).
- ¹⁰I. Z. Kiss and J. L. Hudson, "Phase synchronization of nonidentical chaotic electrochemical oscillators," *Phys. Chem. Chem. Phys.* **4**, 2638–2647 (2002).
- ¹¹M. Nixon, M. Friedman, E. Ronen, A. A. Friesem, N. Davidson, and I. Kanter, "Synchronized cluster formation in coupled laser networks," *Phys. Rev. Lett.* **106**, 223901 (2011).
- ¹²E. Rosa, C. M. Ticos, W. B. Pardo, J. A. Walkenstein, M. Monti, and J. Kurths, "Experimental Chua-plasma phase synchronization of chaos," *Phys. Rev. E: Stat. Nonlinear Soft Matter Phys.* **68**, 025202 (2003).
- ¹³E. Rosa, C. M. Ticos, W. B. Pardo, J. A. Walkenstein, M. Monti, and J. Kurths, "Phase synchronization in a plasma discharge driven by a chaotic signal," *AIP Conf. Proc.* **676**, 301–306 (2003).
- ¹⁴A. Bandrivskyy, A. Bernjak, P. McClintock, and A. Stefanovska, "Wavelet phase coherence analysis: Application to skin temperature and blood flow," *Cardiovasc. Eng.* **4**, 89–93 (2004).
- ¹⁵F. Mormann, K. Lehnertz, P. David, and C. E. Elger, "Mean phase coherence as a measure for phase synchronization and its application to the eeg of epilepsy patients," *Phys. D* **144**, 358–369 (2000).
- ¹⁶C. Schäfer, M. G. Rosenblum, H. H. Abel, and J. Kurths, "Synchronization in the human cardiorespiratory system," *Phys. Rev. E* **60**, 857–870 (1999).
- ¹⁷S. H. Strogatz and I. Stewart, "Coupled oscillators and biological synchronization," *Sci. Am.* **269**, 102–109 (1993).
- ¹⁸M. G. Rosenblum, A. S. Pikovsky, and J. Kurths, "Synchronization approach to analysis of biological systems," *Fluctuation Noise Lett.* **4**, L53–L62 (2004).
- ¹⁹P. Tass, M. G. Rosenblum, J. Weule, J. Kurths, A. Pikovsky, J. Volkmann, A. Schnitzler, and H. J. Freund, "Detection of $n:m$ phase locking from noisy data: Application to magnetoencephalography," *Phys. Rev. Lett.* **81**, 3291–3294 (1998).
- ²⁰T. Pereira, M. S. Baptista, and J. Kurths, "Multi-time-scale synchronization and information processing in bursting neuron networks," *Eur. Phys. J. Spec. Top.* **146**, 155–168 (2007).
- ²¹A. Pikovsky, M. Rosenblum, and J. Kurths, "Phase synchronization in regular and chaotic systems," *Int. J. Bifurcation Chaos* **10**, 2291–2305 (1999).
- ²²M. C. Romano, M. Thiel, J. Kurths, I. Z. Kiss, and J. L. Hudson, "Detection of synchronization for non-phase-coherent and non-stationary data," *Europhys. Lett.* **71**, 466 (2005).
- ²³J. Kurths, M. C. Romano, M. Thiel, G. V. Osipov, M. V. Ivanchenko, I. Kiss, and J. L. Hudson, "Synchronization analysis of coupled noncoherent oscillators," *Nonlinear Dyn.* **44**, 135–149 (2006).
- ²⁴T. Pereira, M. S. Baptista, and J. Kurths, "General framework for phase synchronization through localized sets," *Phys. Rev. E* **75**, 026216 (2007).
- ²⁵H. Fujisaka, T. Yamada, G. Kinoshita, and T. Kono, "Chaotic phase synchronization and phase diffusion," *Phys. D* **205**, 41–47 (2005).
- ²⁶C. Kim, K. Kumar, B. Raj, and R. M. Stern, "Signal separation for robust speech recognition based on phase difference information obtained in the frequency domain," in *INTER_SPEECH* (2009), pp. 2495–2498.
- ²⁷A. Tyrrell and G. Auer, "Biologically inspired intercellular slot synchronization," *J. Wireless Commun. Networking* **2009**, Art. No. 12, 854087 (2009).
- ²⁸T. Pereira, M. Baptista, and J. Kurths, "Phase and average period of chaotic oscillators," *Phys. Lett. A* **362**, 159–165 (2007).
- ²⁹A. Balanov, N. Janson, D. Postnov, and O. Sosnovtseva, *Synchronization: From Simple to Complex* (Springer, New York, 2008).
- ³⁰R. Follmann, E. E. N. Macau, and E. Rosa, "Detecting phase synchronization between coupled non-phase-coherent oscillators," *Phys. Lett. A* **373**, 2146–2153 (2009).
- ³¹R. Follmann, E. E. N. Macau, and E. Rosa, "Phase detection of chaos," *Phys. Rev. E* **83**, 016209 (2011).
- ³²A. E. Hramov and A. A. Koronovskii, "An approach to chaotic synchronization," *Chaos* **14**, 603–610 (2004).
- ³³A. E. Hramov, A. A. Koronovskii, and Y. Levin, "Synchronization of chaotic oscillator time scales," *J. Exp. Theor. Phys.* **100**, 784–794 (2005).
- ³⁴A. E. Hramov and A. A. Koronovskii, "Time scale synchronization of chaotic oscillators," *Phys. D* **206**, 252–264 (2005).
- ³⁵A. E. Hramov, A. A. Koronovskii, V. I. Ponomarenko, and M. D. Prokhorov, "Detection of synchronization from univariate data using wavelet transform," *Phys. Rev. E* **75**, 056207 (2007).
- ³⁶A. A. Koronovskii and A. E. Hramov, "Chaotic phase synchronization studied by means of continuous wavelet transform," *Tech. Phys. Lett.* **30**, 587–590 (2004).
- ³⁷A. A. Koronovskii and A. E. Hramov, "Wavelet transform analysis of the chaotic synchronization of dynamical systems," *JETP Lett.* **79**, 316–319 (2004).
- ³⁸A. A. Koronovskii, M. Kurovskaya, and A. E. Hramov, "Relationship between phase synchronization of chaotic oscillators and time scale synchronization," *Tech. Phys. Lett.* **31**, 847–850 (2005).
- ³⁹A. A. Koronovskii, V. I. Ponomarenko, M. D. Prokhorov, and A. E. Hramov, "Diagnostics of the synchronization of self-oscillatory systems by an external force with varying frequency with the use of wavelet analysis," *J. Commun. Technol. Electron.* **52**, 544–554 (2007).
- ⁴⁰E. B. Postnikov, "On precision of wavelet phase synchronization of chaotic systems," *J. Exp. Theor. Phys.* **105**, 652–654 (2007).
- ⁴¹E. B. Postnikov, "Wavelet phase synchronization and chaoticity," *Phys. Rev. E* **80**, 057201 (2009).
- ⁴²R. Q. Quiroga, A. Kraskov, T. Kreuz, and P. Grassberger, "Performance of different synchronization measures in real data: A case study on electroencephalographic signals," *Phys. Rev. E* **65**, 041903 (2002).
- ⁴³I. Daubechies, "The wavelet transform, time-frequency localization and signal analysis," *IEEE Trans. Inf. Theory* **36**, 961–1005 (1990).
- ⁴⁴N. G. Kingsbury, "The dual-tree complex wavelet transform: A new efficient tool for image restoration and enhancement," in *EUSIPCO* (1998), pp. 319–322.
- ⁴⁵N. G. Kingsbury, "Shift invariant properties of the dual-tree complex wavelet transform," in *ICASSP* (1999), pp. 1221–1224.
- ⁴⁶N. G. Kingsbury, "Image processing with complex wavelets," *Philos. Trans. R. Soc. London, Ser. A* **357**, 2543–2560 (1999).
- ⁴⁷N. G. Kingsbury, "A dual-tree complex wavelet transform with improved orthogonality and symmetry properties," *Int. Conf. Image Process.* **2**, 375–378 (2000).
- ⁴⁸N. G. Kingsbury, "Complex wavelets for shift invariant analysis and filtering of signals," *Appl. Comput. Harmonic Anal.* **10**, 234–253 (2001).
- ⁴⁹I. W. Selesnick, R. G. Baraniuk, and N. G. Kingsbury, "The dual-tree complex wavelet transform," *IEEE Signal Process. Mag.* **22**, 123–151 (2005).
- ⁵⁰E. E. N. Macau, C. Grebogi, and Y.-C. Lai, "Active synchronization in nonhyperbolic hyperchaotic systems," *Phys. Rev. E* **65**, 027202 (2002).

- ⁵¹I. Daubechies, J. Lu, and H. T. Wu, "Synchrosqueezed wavelet transforms: An empirical mode decomposition-like tool," *Appl. Comput. Harmonic Anal.* **30**, 243–261 (2011).
- ⁵²D. Iatsenko, A. Bernjak, T. Stankovski, Y. Shiogai, P. J. Owen-Lynch, P. Clarkson, P. McClintock, and A. Stefanovska, "Evolution of cardiorespiratory interactions with age," *Philos. Trans. R. Soc. London, Ser. A* **373**, 1–18 (2013).
- ⁵³G. Thakur, E. Brevdo, N. S. Fuckar, and H.-T. Wu, "The synchrosqueezing algorithm for time-varying spectral analysis: Robustness properties and new paleoclimate applications," *Signal Process.* **93**, 1079–1094 (2013).
- ⁵⁴H. T. Wu, Y. H. Chan, Y. T. Lin, and Y. H. Yeh, "Using synchrosqueezing transform to discover breathing dynamics from ecg signals," *Appl. Comput. Harmonic Anal.* **36**, 354–359 (2014).
- ⁵⁵B. Kralemann, M. Frühwirth, A. Pikovsky, M. Rosenblum, T. Kenner, J. Schaefer, and M. Moser, "In vivo cardiac phase response curve elucidates human respiratory heart rate variability," *Nat. Commun.* **4**, 2418 (2013).
- ⁵⁶B. Kralemann, L. Cimponeriu, M. Rosenblum, A. Pikovsky, and R. Mrowka, "Phase dynamics of coupled oscillators reconstructed from data," *Phys. Rev. E* **77**, 066205 (2008).
- ⁵⁷J. T. C. Schwabedal, A. Pikovsky, B. Kralemann, and M. Rosenblum, "Optimal phase description of chaotic oscillators," *Phys. Rev. E* **85**, 026216 (2012).
- ⁵⁸J. P. Lachaux, E. Rodriguez, J. Martinerie, and F. J. Varela, "Measuring phase synchrony in brain signals," *Hum. Brain Mapp.* **8**, 194–208 (1999).
- ⁵⁹L. W. Sheppard, A. Stefanovska, and P. V. E. McClintock, "Testing for time-localized coherence in bivariate data," *Phys. Rev. E* **85**, 046205 (2012).
- ⁶⁰A. V. Tankanag, A. A. Grinevich, T. V. Kirilina, G. V. Krasnikov, G. M. Piskunova, and N. K. Chemeris, "Wavelet phase coherence analysis of the skin blood flow oscillations in human," *Microvasc. Res.* **95**, 53–59 (2014).
- ⁶¹Y. Kuramoto, "Self-entrainment of a population of coupled non-linear oscillators," *International Symposium on Mathematical Problems in Theoretical Physics* (1975), Vol. 39, pp. 420–422.
- ⁶²R. L. Burden and J. D. Faires, *Numerical Analysis* (Brooks Cole, Belmont, MA, 2010).
- ⁶³W. Kühnel, *Differential Geometry: Curves, Surfaces, Manifolds*, Europe and Central Asia Environmentally and Socially Sustain (American Mathematical Society, Providence, 2002).
- ⁶⁴M. W. Hirsch, S. Smale, and R. L. Devaney, *Differential Equations, Dynamical Systems, and an Introduction to Chaos* (Elsevier, New York, 2004), Vol. 60.
- ⁶⁵O. E. Rössler, "An equation for continuous chaos," *Phys. Lett. A* **57**, 397–398 (1976).
- ⁶⁶K. Alligood, T. Sauer, and J. Yorke, *Chaos: An Introduction to Dynamical Systems* (Springer, New York, NY, 1997).
- ⁶⁷S. Boccaletti, J. Kurths, G. Osipov, D. Valladares, and C. Zhou, "The synchronization of chaotic systems," *Phys. Rep.* **366**, 1–101 (2002).
- ⁶⁸J. Y. Chen, K. W. Wong, and J. W. Shuai, "Properties of phase locking with weak phase-coherent attractors," *Phys. Lett. A* **285**, 312–318 (2001).
- ⁶⁹S. G. Mallat, *A Wavelet Tour of Signal Processing* (Academic Press, New York, 1998).
- ⁷⁰S. G. Mallat, "A theory for multiresolution signal decomposition: The wavelet representation," *IEEE Trans. Pattern Anal. Mach. Intell.* **11**, 674–693 (1989).
- ⁷¹N. G. Kingsbury, "Design of q-shift complex wavelets for image processing using frequency domain energy minimization," *Int. Conf. Image Process.* **1**, I-1013-16 (2003).

Appendix 2: Partial synchronization in networks of non-linearly coupled oscillators: The Deserter Hubs Model

Partial synchronization in networks of non-linearly coupled oscillators: The Deserter Hubs Model

Celso Freitas¹, Elbert Macau¹, and Arkady Pikovsky¹

Citation: *Chaos* **25**, 043119 (2015); doi: 10.1063/1.4919246

View online: <http://dx.doi.org/10.1063/1.4919246>

View Table of Contents: <http://aip.scitation.org/toc/cha/25/4>

Published by the [American Institute of Physics](#)

Partial synchronization in networks of non-linearly coupled oscillators: The Deserter Hubs Model

Celso Freitas,^{1,a)} Elbert Macau,^{1,b)} and Arkady Pikovsky^{2,c)}

¹Associate Laboratory for Computing and Applied Mathematics - LAC, Brazilian National Institute for Space Research - INPE, Brazil

²Department of Physics and Astronomy, University of Potsdam, Germany and Department of Control Theory, Nizhni Novgorod State University, Gagarin Av. 23, 606950, Nizhni Novgorod, Russia

(Received 13 January 2015; accepted 16 April 2015; published online 30 April 2015)

We study the Deserter Hubs Model: a Kuramoto-like model of coupled identical phase oscillators on a network, where attractive and repulsive couplings are balanced dynamically due to nonlinearity of interactions. Under weak force, an oscillator tends to follow the phase of its neighbors, but if an oscillator is compelled to follow its peers by a sufficient large number of cohesive neighbors, then it actually starts to act in the opposite manner, i.e., in anti-phase with the majority. Analytic results yield that if the repulsion parameter is small enough in comparison with the degree of the maximum hub, then the full synchronization state is locally stable. Numerical experiments are performed to explore the model beyond this threshold, where the overall cohesion is lost. We report in detail partially synchronous dynamical regimes, like stationary phase-locking, multistability, periodic and chaotic states. Via statistical analysis of different network organizations like tree, scale-free, and random ones, we found a measure allowing one to predict relative abundance of partially synchronous stationary states in comparison to time-dependent ones. © 2015 AIP Publishing LLC.

[<http://dx.doi.org/10.1063/1.4919246>]

Regarding large populations of coupled oscillators, phase-synchronization may emerge due to attractive coupling, while repulsive coupling favors desynchronized states. However, the nature of coupling may depend on the strength of the local forcing: if the force on the oscillator from a sufficiently large number of neighbors becomes too strong, it can desert switch from a “conformist” to a “contrarian” behavior. We study such a population on a network. Here, the oscillators connected to many others become contrarians first, so that synchrony breaks. This is why our approach can be fairly understood as Deserter Hubs Model. We show that the partial synchrony regimes can be rather complex, with a large degree of multistability. Besides, we suggest a network measure which allows predicting relative abundance of static and dynamic regimes.

approach can be used as a framework to several natural and technological systems where an ordered behavior (synchronization) emerges from the interactions of many dynamical agents.^{1,25} Furthermore, works have shown that the Kuramoto model can be exploited as a building block to develop highly efficient strategies to process information.^{7,30}

Recently, generalizations of the Kuramoto model toward interconnections between the elements more complex than the mean field one, have received considerable attention. Indeed, in many real-world problems, each dynamical agent interacts with a subset of the whole ensemble,^{5,15,24} which can be better described using networks. A myriad of studies have analyzed the onset of the synchronization regime in this context. For a general class of linearly coupled identical oscillators, the Master Stability Function, originally proposed by Pecora and Carroll,¹⁹ allows one to determine an interval of coupling strength values that yields complete synchronization, as a function of the eigenvalues of Laplacian matrix of the coupling graph. For networks of oscillators with non-identical natural frequencies, Jadbabaie *et al.*¹³ were able to give similar bounds for the coupling strength of the Kuramoto model without the assumption of infinitely many phase-oscillators. Among related works, Ref. 8 deals with a model whose natural frequency oscillators change with time, even when they are isolated. Reference 18 explores the effects of delay in the communication between oscillators. Besides, Ref. 20 builds a bridge between graph symmetry and cluster synchronization.

Taking into consideration all of these previous results, one can roughly state that the Kuramoto transition to synchronization happens if the coupling between oscillators is attractive; while this synchronization state is absent when it

I. INTRODUCTION

In a seminal work,¹⁴ aiming to understand synchronization phenomena, Kuramoto proposed a mathematical model of non-identical, nonlinear phase-oscillators, mutually coupled via common mean field. Studying this system, he identified a synchronization transition to an oscillating global mode when the coupling strength is larger than a critical value, which is proportional to the range of the distribution of the natural frequencies. Over the time, subsequent outcomes based on Kuramoto propositions have shown that his

^{a)}cbnfreitas@gmail.com.

^{b)}elbert.macau@inpe.br.

^{c)}pikovsky@uni-potsdam.de.

changes to repulsiveness.^{28,29} However, the structure of the coupling can non-trivially depend on the level of synchrony itself. Such a dependence, called nonlinear coupling scheme, has been explored in recent theoretical^{3,6,21,23} and experimental^{26,27} studies dealing with setup of global coupling. The main effect here is the partial synchrony, which establishes at moderate coupling strengths, where the coupling is balanced between the attractive and repulsive one.

Here, we consider the effects of the non-linear coupling on a network: a set of identical oscillators, which communicate via a connected simple coupling graph. Each element is forced by a (local) mean field, which encompasses the oscillators that are connected to it. The coupling function is tailored so that its influence is attractive, if the local acting field is small, or repulsive, otherwise. This coupling strategy implies that only nodes with a large enough number of connections may become repulsive. Thus, the hubs play a key role for the ensemble dynamics. A non-linear coupling parameter in the system tunes the critical quantity of connections and how cohesive this mean field must be in order to allow this transition. So, our *Deserter Hubs Model (DHM)* can be considered as a dynamical generalization of the inhomogeneous populations of oscillators consisting of *conformists* and *contrarians*.¹² Nevertheless, the kind of behavior depends on the force acting on it.

One of real-world situations where such a nonlinear coupling on a network may be relevant is the deep brain stimulation of neural synchronous oscillations at Parkinson disease by a nonlinear feedback.²² While in Ref. 22 nonlinear coupling has been treated in the framework of global field approximation, a setup where different parts of the neural network are subject to different nonlinear actions, leading to deserter hubs, appears to be more realistic.

Overall dynamics in the model can be qualitatively understood as follows: Let us assume initially that all the mean fields are small. Then, there are only attractive interactions (*conformists*) in the system. So, in a first moment, they start to mutually adjust their phases. Above a threshold, the most connected oscillators start to feel a repulsive effect that drives them away from the synchronous state. In other words, if an oscillator has a sufficiently large number of neighbors and if it suffers enough cohesive pressure from them, instead of attractiveness, it becomes a *contrarian*, wishing to be in anti-phase with the force. Then, due to the repulsiveness of some nodes, other mean fields may also become smaller. Finally, this tendency can shift nodes to attractiveness again. As a consequence, an intermediate configuration may emerge due to the balance these conflicting tendencies in the system.

Depending on the non-linear coupling parameter, we report a variety of qualitative dynamic behaviors. In general, for small values of the non-linear coupling parameter, we observed full synchronization and phase-locked states. When this parameter is increased, multistability, periodic and chaotic dynamics take place.

The paper is organized as follows. Initially, we discuss the basic details of the model in Sec. II. In Sec. III, the analytical result about the stability of full synchronization is presented. Numerical experiments in Sec. IV illustrate different

possible regimes that the present model can display. In Sec. IV C, we perform a numerical exploration to address the correlation of stationary phase locking states with partial synchronization with the network parameters, by exploring different network topologies and sizes.

II. MODEL OF OSCILLATOR NETWORK WITH NONLINEAR COUPLING: THE DESERTER HUBS MODEL (DCM)

Mainly inspired by ideas from Ref. 21, the DHM is a Kuramoto-like model whose dynamic explicitly depends on a local cohesion quantifier. Let us consider a system of N identical phase-oscillators represented by $(\theta_1, \dots, \theta_N) \in [0, 2\pi)^N$ coupled through a simple and connected undirected graph A . The dynamics for the i -th oscillator in the DHM, with $i = 1, \dots, N$, is given by the following ordinary differential equation

$$\dot{\theta}_i = (1 - \varepsilon Z_i^2) \sum_{j \in \mathcal{N}_i} \sin(\theta_j - \theta_i), \quad (1)$$

where \mathcal{N}_i denotes the set of neighbors of i in the coupling graph A . Equations (1) are formulated in the reference frame rotating with the common frequency of the oscillators, so that the latter one does not appear in the equations. The time is normalized by the linear coupling strength.

The main feature of the DHM (1) is the non-negative¹⁶ *nonlinear coupling parameter* ε , which modifies the coupling at each node. If $\varepsilon = 0$, the standard setup of the Kuramoto model with constant unitary coupling strength on a network is recovered.¹³

We denote by d_i the degree of the i -th vertex, that is, the number of incoming or outgoing connection, since the graph is undirected. Also, we make use of the local mean field (or local order parameter)

$$Z_i e^{i\bar{\theta}_i} := \sum_{j \in \mathcal{N}_i} e^{i\theta_j}, \quad (2)$$

where Z_i is the *norm of the local i -th order parameter* which measures the magnitude of the force acting on oscillator with index i . In addition, $\bar{\theta}_i$ can also be expressed as $(d_i)^{-1} \sum_{j \in \mathcal{N}_i} \theta_j$, which corresponds to the *direction pointed by the i -th local mean field*. Note that for the standard Kuramoto model, we have that

$$\dot{\theta}_i = d_i Z_i \sin(\bar{\theta}_i - \theta_i). \quad (3)$$

Thus, unless $\bar{\theta}_i - \theta_i = \pi \bmod 2\pi$, the state of the of the i -th oscillator will get closer to $\bar{\theta}_i$, which is precisely what we mean by “attractive coupling”. If the opposite happens, for instance, if we change the sign of the r.h.s. of Eq. (3), we say that the coupling is repulsive.

On the other hand, we represent the (*global*) *order parameter* by

$$R e^{i\psi} = \frac{1}{N} \sum_{i=1}^N e^{i\theta_i}, \quad (4)$$

where $R \in [0, 1]$ is its norm and $\psi \in (0, 2\pi]$ is its phase.

We stress that Z_i is not normalized (in the sense that there is no division by the number of the terms in the summation, like in R), as it measures the total action of the neighbors on the i -th oscillator, which is called *local mean field*. Simple calculations show that $Z_i^2 \in [0, d_i^2]$. Thus, a necessary condition for a node to suffer repulsive coupling, i.e., $1 - \varepsilon Z_i^2 < 0$, is that $\varepsilon > d_i^{-2}$.

Notice also that instead of attenuating local coherent, we wanted to enhance its effect over the dynamics, this is why we opt not to normalize the r.h.s of Eq. (1) by the associated in-degree d_i .

The introduced order parameters R and Z_1, \dots, Z_N are maximal in the case of full synchronization $\theta_1 = \dots = \theta_N$, while they decrease when oscillators begin to move apart from each other.

If $\varepsilon Z_{\max}^2 < 1$, where $Z_{\max}^2 := \max\{Z_1^2, \dots, Z_N^2\}$, then all oscillator will attract each other so that the full synchronization is established. Next, if Z_{\max}^2 becomes larger than ε^{-1} , the corresponding oscillator begins to be repulsive related to its local mean field, and the full synchronization breaks. As a result, Z_{\max}^2 may decrease and switch again the node to be attractive. Depending on the coupling graph A , on the initial condition $(\theta_1^0, \dots, \theta_N^0)$, and on the intensity of the nonlinear coupling parameter ε , numerical simulation reveals that model (1) can exhibit different qualitative behaviors.

If the largest degree in the coupling graph satisfies $\varepsilon < d_{\max}^{-2}$, with $d_{\max} := \max\{d_1, \dots, d_N\}$, then no node can be repulsive. We demonstrate in Sec. III via the Lyapunov analyses, that in fact this condition guarantees that the full synchronized state is stable.

III. STABILITY OF FULL SYNCHRONIZATION

The basic procedure to obtain the results in this section follows.¹³ We begin presenting some preliminary concepts, including elements of the graph theory needed, and a generalized norm of the order parameter to define our Lyapunov function.

Let B be the *directed incidence matrix* of a graph A . Thus, B is a matrix with N rows and E columns, where E is the number of *directed edges* of the matrix. The number of *undirected edges*, i.e., ignoring the direction, equals is $E/2$. The columns of B represent the edges of the graph: if the k -th arrow (directed edge) of the graph goes from i to j , then the k -th column of B is zero, except at positions i and j , where $B_{ik} = 1$ and $B_{jk} = -1$. Regarding the dynamics of the system, an arrow from node i to node j in the graph means that node i influences node j . Although the directed incidence matrix is generally defined for directed graphs, it must be emphasized that only undirected graphs are considered here. We abuse terminology and identify a graph A with its *adjacency matrix*, which is an $N \times N$ matrix where $A_{ii} = 0$; $A_{ij} = A_{ji} = 1$, if there is an edge between nodes i, j ; and $A_{ij} = A_{ji} = 0$, otherwise. So, $E = \sum_{i,j=1}^N A_{ij}$. Another common characterization of a graph is its *Laplacian matrix*, $L := \text{diag}(d_1, \dots, d_N) - A$. One can check that $L = 1/2BB^\top$. A simple illustration of these concepts is given at Fig. 1.

The usage of the directed incidence matrix allows us to rewrite model (1) in a vector form:

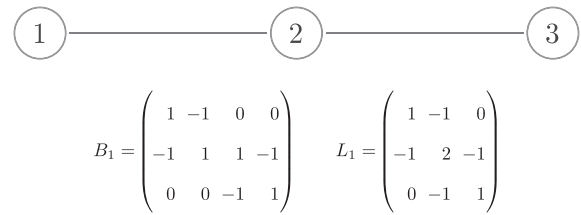


FIG. 1. Example of graph with $N=3$ and $E=4$, its directed incidence matrix B_1 and its Laplacian matrix L_1 .

$$\dot{\theta} = -\frac{1}{2} \text{diag}(1_N - \varepsilon Z^2) B \sin(B^\top \theta), \quad (5)$$

where $Z^2 := (Z_1^2, \dots, Z_N^2)$, $1_N := (1, \dots, 1) \in \mathbb{R}^N$ and $\text{diag}(\cdot)$ stands for the matrix with the elements of a vector on the leading diagonal, and 0 elsewhere.

The square of the global order parameter can be expressed as

$$R^2 = \frac{1}{N^2} \left(N + 2 \sum_{j < k} \cos(\theta_j - \theta_k) \right).$$

However, to build our Lyapunov function, we define a *generalized norm of order r* as

$$r^2 := 1 - \frac{E - 1_E^\top \cos(B^\top \theta)}{N^2}. \quad (6)$$

Note that R^2 requires the sum of *all* $\cos(\theta_j - \theta_k)$ with $j < k$ (for $j, k = 1, \dots, N$), but its generalization r^2 takes into account the sum $(1_E^\top \cos(B^\top \theta))$ *only* through the edges of the graph. In the case of full coupling graph, direct substitution yields that both global and generalized norm of the order parameter have the same expression.

For any connected symmetrical coupling graph, one can check that the maximum of r^2 is the unit, and that $R^2 = 1$ if and only if this value is achieved.¹⁷

Let

$$U(\theta) = 1 - r^2 \quad (7)$$

be a candidate Lyapunov function. It is clear that the minimum value of $U(\theta) = 0$ corresponds to the maximum value of $r^2 = 1$, which is equivalent to the fully synchronized state.

In fact, algebraic manipulations reveal that

$$U(\theta) = \frac{2}{N^2} \left\| \sin\left(\frac{B^\top \theta}{2}\right) \right\|^2, \quad (8)$$

and that the differential of U is given by

$$DU = \frac{1}{N^2} (B \sin(B^\top \theta))^\top. \quad (9)$$

As a result, we synthesize in the next theorem the previously suggested argument that if ε is small enough, then full synchronization is a robust phenomenon related to small perturbations over initial conditions.

Theorem 1. *In Model (1), if ε is smaller than a critical value $\varepsilon_c := 1/d_{\max}^2$, then the synchronized stated ($R = 1$) is Lyapunov stable.*

Proof. Consider the potential field $U(\theta)$ defined in Eq. (7). So, using the vector form of the model (5) and the expression of the differential DU from Eq. (9), we have that $\frac{d}{dt}U(\theta(t))$ equals to

$$-\frac{1}{2N^2}(\sin(B^T\theta))^T B^T \text{diag}(1_N - \varepsilon Z^2) B \sin(B^T\theta). \quad (10)$$

If we set $x := B \sin(B^T\theta)$, then we have that $x^T \text{diag}(1_N - \varepsilon Z^2)x$ is larger or equal than $(1 - \varepsilon d_{\max}^2)\|x\|^2$. Moreover, we can also define a lower bound for $\|x\|^2$, since $\|x\|^2 = \sin(B^T\theta)^T B^T B \sin(B^T\theta) \geq \lambda_2(B^T B)\|\sin(B^T\theta)\|^2 = 2\lambda_2(L)\|\sin(B^T\theta)\|^2$; where $\lambda_2(L)$ is the algebraic connectivity of the graph. In the last inequality, we used that $\frac{1}{2BB^T} = L$ and that both matrices BB^T and $B^T B$ have the same non-trivial eigenvalues $0 \leq \lambda_2(L) < \dots < \lambda_N(L)$, where $\lambda_2(L)$ is strictly larger than zero because the coupling graph A is connected.⁹ Therefore,

$$\frac{d}{dt}U(\theta(t)) \leq -\frac{1}{N^2}\lambda_2(L)(1 - \varepsilon d_{\max}^2)\|\sin(B^T\theta)\|^2.$$

As a result, $\varepsilon < \varepsilon_c := 1/d_{\max}^2$ implies that $\frac{d}{dt}U(\theta(t)) \leq 0$, then the fully synchronized state $R = 1$ is stable. \square

IV. DYNAMICS OF PARTIALLY SYNCHRONOUS STATES

In this section, numerical simulations are performed to illustrate the rich repertoire of behaviors that model (1) may exhibit, specially beyond the threshold $\varepsilon > \varepsilon_c$, where Theorem 1 cannot be applied.

A. Quantification of dynamical regimes

The numerical integration scheme applied is a fourth order Adams-Bashforth-Moulton Method (see Ref. 4) with discretization time step $h = 0.01$. We calculate the *partial synchronization metrics* from Ref. 11, which, for every two oscillators i, j in the network, takes values $s_{ij}(I) \in [0, 1]$, indicating how much the *mean phase difference* between θ_i and θ_j varies in the time interval $I := [t_1, t_2]$, with $t_1 < t_2$. This metric is defined as

$$s_{ij}(I) \doteq \left\| \frac{1}{t_2 - t_1} \int_{t_1}^{t_2} e^{i(\theta_i(t) - \theta_j(t))} dt \right\|.$$

One can check that if $\theta_i(t) \equiv \theta_j(t) + \eta$ for some constant η , then the exponent in the previous integral is constant and $s_{ij}(I) = 1$. Nevertheless, if $\theta_i(t) - \theta_j(t) \bmod 2\pi$ assumes every possible value over the unit circumference with not clear trend, then $s_{ij}(I)$ is close to zero. Now, we average contributions of all neighbor oscillators i, j under a graph A with N nodes to write

$$s(I) \doteq \frac{1}{E} \sum_{i,j=1}^N A_{ij} s_{ij}(I),$$

where E is the quantity of undirected edges in the graph.

To exclude transients and to detect the statistically stationary state, we adopted the following procedure. For all experiments the time interval $[0, 2.10^3]$ is always considered

as transient time. Then, the numerical integration is performed in the subsequent intervals $I_k := [(k - 1), k]10^3$, with $k \geq 3$, until the first $\tilde{k} = k$ such that $|s(I_{\tilde{k}-1}) - s(I_{\tilde{k}})| < 0.01$, or $\tilde{k} = 10$ is achieved. Only such a time interval $I_{\tilde{k}}$ is regarded as non-transient. For the subsequent analysis, we use values of the phases $\theta(t)$ in the stationary time interval regime $I_{\tilde{k}}$ (whose beginning is shifted to $t = 0$ without loss of generality) at points $t \in \tilde{I} := \{ih, i \in \{0, 1, \dots, 10^5 - 1, 10^5\}\}$.

B. Examples of complex behaviors

As it was claimed before, in dependence on the network structure, very different types of the dynamics are possible. In order to give impression on it, we present simulations of model (1) with two different coupling graphs displayed as insets in Fig. 2. Both networks have $N = 10$ nodes and they differ only by the rewiring of a single edge. We performed simulations for 10 random initial conditions chosen with uniform distribution over $[0, 2\pi]$ for each experiment. For all these initial conditions $l = 1, \dots, 10$, the norm of the order parameter $R^l(t)$, according to Eq. (4), is computed from the time series. As explained the last paragraph of subsection, in these calculations a transient time is eliminated and that a statistically stationary regime \tilde{I} of 10^3 units of time and $\#\tilde{I} := 10^5 + 1$ points is considered. Then, also for each distinct initial condition, the maximum, average and minimum values of the associated norm of the order parameter are computed, respectively, denoted by $R_{\max}^l := \max_{t \in \tilde{I}} R^l(t)$; $\langle R^l \rangle := (\#\tilde{I})^{-1} \sum_{t \in \tilde{I}} R^l(t)$; and $R_{\min}^l := \min_{t \in \tilde{I}} R^l(t)$. Of course, $R^l(t)$ converges to a constant if and only if $R_{\max}^l = \langle R^l \rangle = R_{\min}^l$. Now, having different simulations for a fixed coupling graph, we evaluated the maximum, average and minimum value of the *average* value of the norm of the order parameters over this ensemble, denoted by $\max\{\langle R \rangle\} :=$

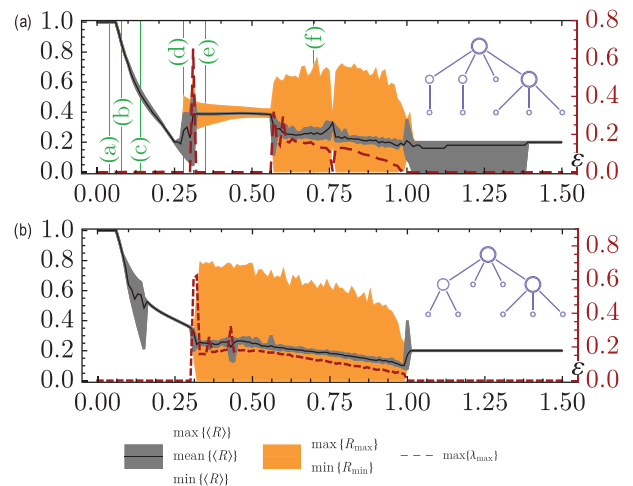


FIG. 2. Numerical results for Model (1) as a function of ε , for the coupling graphs depicted as inset, including 10 random initial conditions. A black line corresponds to $\text{mean}\{\langle R \rangle\}$, while the interval between $\text{min}\{\langle R \rangle\}$ and $\text{max}\{\langle R \rangle\}$ is shown as a gray strip. The gap between $\text{min}\{R_{\min}\}$ and $\text{max}\{R_{\max}\}$ is shown as an orange strip. Since the orange strip is by construction larger or equal than the gray one, the first one is not displayed in the figure when they coincide. Left vertical axes show values related to norm of the order parameter, while the right ones represents the maximum Lyapunov exponent λ_{\max} , shown as a red dashed line. Letters in green vertical lines from the upper experiment correspond to the inset in Fig. 3.

$\max_{l=1,\dots,10} \langle R^l \rangle$; $\text{mean}\{\langle R \rangle\} := (10)^{-1} \sum_{l=1,\dots,10} \langle R^l \rangle$; and $\min\{\langle R \rangle\} := \min_{l=1,\dots,10} \langle R^l \rangle$. So, if the norm of the order parameter converges to the same value for *all* initial conditions simulated, then $\max\{\langle R \rangle\} = \text{mean}\{\langle R \rangle\} = \min\{\langle R \rangle\}$. For the cases where the norm of the order parameter does not converge over all initial conditions, it will be useful to examine the *overall maximum* and *overall minimum* values of the norm of the order parameter, respectively denoted by $\max\{R_{\max}^l\} := \max_{l=1,\dots,10} R_{\max}^l$; and $\min\{R_{\min}^l\} := \min_{l=1,\dots,10} R_{\min}^l$. Thus, if there is no fixed phase synchronization for all the initial conditions simulated, but the norm of the order parameter presents only small deviations around a common value, then the gap between $\max\{R_{\max}^l\}$ and $\min\{R_{\min}^l\}$ is also small. Also notice that $\min\{R_{\min}^l\} \leq \min\{\langle R \rangle\} \leq \text{mean}\{\langle R \rangle\} \leq \max\{\langle R \rangle\} \leq \max\{R_{\max}^l\}$, since $R_{\min}^l \leq \langle R^l \rangle \leq R_{\max}^l$ for all initial conditions. Finally, the maximum Lyapunov exponent λ_{\max}^l for each initial condition is also computed, according to the algorithm in Ref. 2. The maximum Lyapunov exponent over all the chosen initial conditions $\lambda_{\max}^l := \max_{l=1,\dots,10} \lambda_{\max}^l$ is also analyzed.

We now describe different regimes observed in the networks, using also Fig. 3, where we depict time series of $R(\theta(t))$ for some particular choices of ε , indicated as green letters in the upper panel from Fig. 2 (this is the case we choose for illustrating different regimes). Notice that $d_{\max} = 4$ in both cases, so Theorem 1 guarantees that for $\varepsilon < \varepsilon_c = 1/4^2 = 0.0625$ the full synchronization state, $R \rightarrow 1$, is locally stable as illustrated in Fig. 3(a) (with $\varepsilon = 0.04$).

Panel (a) in Fig. 3 illustrates full synchronization in the network for $\varepsilon < \varepsilon_c$. For ε slightly bigger than ε_c , simulations suggest that a stationary regime of partial phase synchronization, where $R \rightarrow c < 1$, is locally stable as shown in Fig. 3(b)

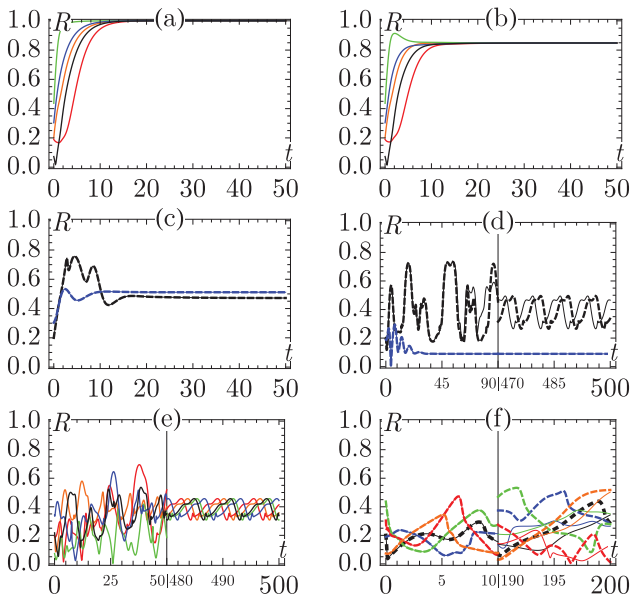


FIG. 3. Evolution of $R(t)$ for different values of ε indicated in green at the upper experiment from Fig. 2. Every color represents a different initial condition, while pairs of solid/dashed lines with the same color correspond to solutions whose initial conditions differ not more than 10^{-4} at each coordinate. (a) $\varepsilon = 0.04$: full synchronization; (b) $\varepsilon = 0.08$: fixed phase synchronization; (c), (d), (e) $\varepsilon = 0.15, 0.28, 0.35$ respect.: examples of multi stability; (f) $\varepsilon = 0.70$: example with $\lambda_{\max} > 0$.

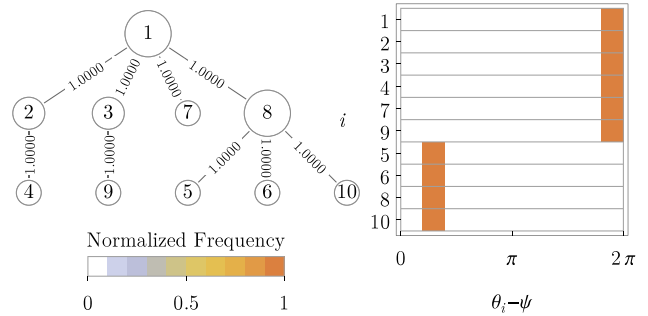


FIG. 4. Example of group formation: details of one of the trajectories from Fig. 3(b) $\varepsilon = 0.08$. On the left side, the coupling graph with $s(i, j)$ in its edges is shown. On the right side, a histogram of $\theta_i - \psi$ in permanent regime is presented with color code representing the normalized frequency. Precisely, we divided the interval $[0, 2\pi)$ into 10 bins with the same size. So, the normalized frequency of the i -th oscillator corresponds to the ratio of points (after the transient time) that the numerical evaluation of $\theta_i - \psi$ placed at each bin.

($\varepsilon = 0.08$). Details of this state are clear from Fig. 4. There we show that the synchronization between the individual oscillators is complete if measured by quantity s_{ij} , and all the oscillators have the same frequency. However, the oscillators are split into two groups with a constant phase shift between them; this division originates in the edge which connects the two largest hubs in the network (vertexes 1, 8).

For larger values of ε , the regimes are still static but with multistability. For instance, at $\varepsilon = 0.15$ (see Fig. 3(c)), two stable configurations emerge with $R \rightarrow c$, with $c \approx 0.471$ (black) or $c \approx 0.511$ (blue), depending on the initial condition. Fig. 5, which is analogous to Fig. 4, shows the existence of three subgroups, whose members may vary according to the initial condition.

Other types of multistabilities appear, for instance, at $\varepsilon = 0.28$ and $\varepsilon = 0.35$, as illustrate in Figs. 3(d) and 3(e). For $\varepsilon = 0.28$ (panel d) some initial conditions do no converge to a fixed phase synchronization, but to a regime where the order parameter R is periodic in time. For $\varepsilon = 0.35$ (panel c), the norm of the order parameter of all trajectories simulated becomes periodic. Fig. 6 provides an illustration of this regime.

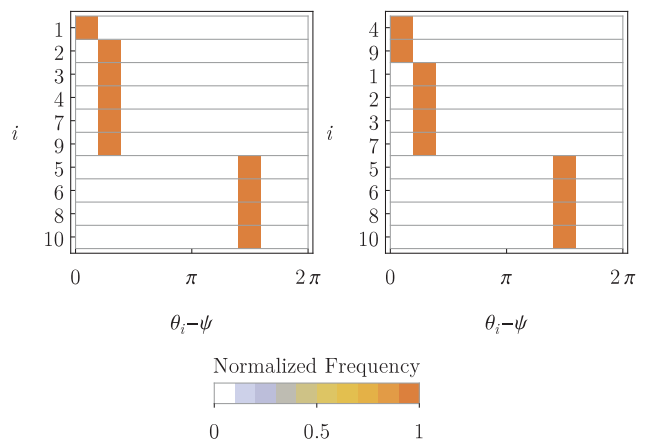


FIG. 5. Example multi-stability with group formation. Details of two trajectories from Fig. 3(c) $\varepsilon = 0.15$ are provided. The left picture corresponds to the solid black line and the right one to the solid blue. Histograms of $\theta_i - \psi$ are like the one in Fig. 4.

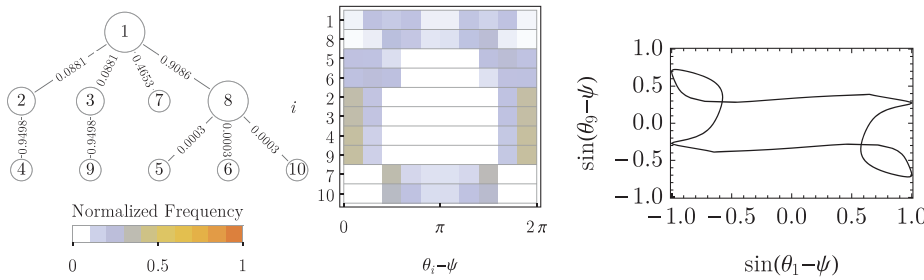


FIG. 6. Example of periodic norm of the order parameter: details of one of the trajectories from Fig. 3(d) $\epsilon = 0.28$. On the left side, the coupling graph with $s(i, j)$ in its edges is shown. A histogram of $\theta_i - \psi$ are like the one in Fig. 4 in the middle figure. We denote by $\psi(t)$ the argument of the order parameter. The picture on the right shows that the curve $(\sin(\theta_1(t) - \psi(t)), \sin(\theta_3(t) - \psi(t)))$ is closed.

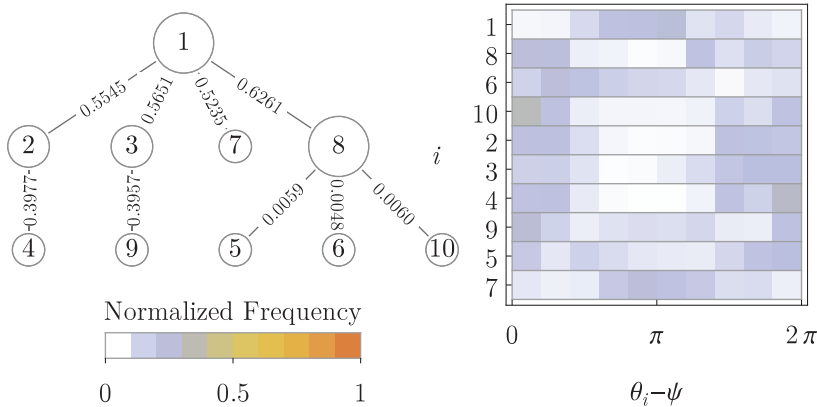


FIG. 7. Example of trajectory with $\lambda_{\max} > 0$: details of one of the trajectories from Fig. 3(f) $\epsilon = 0.70$. On the left side, the coupling graph with $s(i, j)$ in its edges is shown. On the right side, there is a histogram of $\theta_i - \psi$ are like the one in Fig. 4.

For $\epsilon = 0.70$ (Fig. 3(f)), one observes a chaotic state with $\lambda_{\max} > 0$, the distribution of phases and frequencies is illustrated in Fig. 7. The emergence of chaos in the DHM can be seen as the result of irregular contractions and expansions of the oscillator’s state.² Contraction tendencies occur when a node act as conformist (attractiveness), while expansion takes place when it “deserts” due to local mean field cohesion (repulsiveness). When no balance is achieved between these two tendencies, one can observe sensitiveness to initial conditions.

If $\epsilon \in [1, 1.5]$, we also obtained multistability, with the coexistence of solutions converging to phase-lock and irregular order parameter after the transient, similar to Fig. 3(d).

Now, we compare the results for two slightly different networks depicted in panels (a) and (b) in Fig. 2. The interval of values of ϵ with fixed phase synchronization for all initial conditions simulated is very similar for both networks, namely, $\epsilon_c < \epsilon \leq 0.25$; also multistability of static partial synchronous regimes have been observed in both cases.

When $\epsilon \in [1, 1.5]$, contrary to case (a), we observed that the solution for all initial conditions converged to the same phase-lock regime, similar to Fig. 3(b).

In the conclusion of this section, Fig. 8 shows simulation results for two other networks. Panel (a) shows a random network with $N = 10$ nodes and 20 undirected edges. Here predominantly static regimes are observed, only in small ranges of coupling constant chaos with a positive Lyapunov exponent appears. Static regimes, however, demonstrate a large degree of multistability. In panel (b), we show a scale-free network with $N = 50$ nodes and 100 undirected edges. Here static states are rare, typically irregular regimes with low values of the order parameter are observed.

C. Dependence of partial synchronization regimes on network structure

We have seen that partially synchronous states can be rather different even for similar networks. It is therefore difficult to make general predictions for a relation between the network properties and the dynamical behaviors. Here, we attempt such a description, focusing on the property of abundance of static regimes in comparison to time-dependent ones. For this purpose, we define the *convergence index* I_C as the ratio of values of $\epsilon \in [0, 1.5]$ such that R converges to a constant value, considering all the 10 random initial conditions. So, both

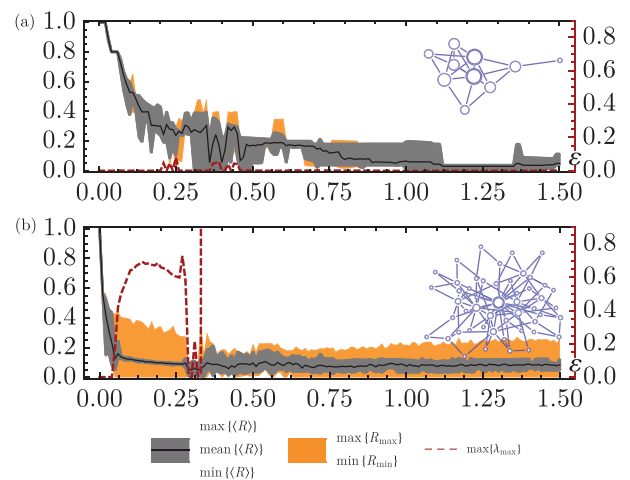


FIG. 8. Numerical results for Model (1) as a function of ϵ , for the coupling graphs depicted as inset, including 10 random initial conditions. The legend of the pictures is the same as in Fig. 2.

networks in Fig. 2 have close values of this index: $I_c \approx 0.530$ in case (a) while $I_c \approx 0.549$ in case (b). In contradistinction, network shown in Fig. 8(a) has very large value of the index $I_c \approx 0.946$, while that in Fig. 8(b) a rather low value $I_c \approx 0.064$.

In order to explore which features of the coupling graph are related with I_c , we performed numerical experiments with three sets of graphs, with $N = 10, 50, 100$ nodes. Each set consists in three common types of networks, each one with 10 members, generated as: (i) random (Erdős-Rényi) graphs with $2N$ edges; (ii) scale-free graphs, also with $2N$; and (iii) tree graphs (N edges). The Barabási-Albert algorithm is applied for the last two types of networks (ii), (iii), with an initial clique of m_0 nodes and with other nodes been connected to m existing ones. For the $2N$ -edges scale-free graphs, we fixed $m_0 = 5$ and $m = 2$; while for the tree graphs (N edges scale-free graphs), $m_0 = m = 1$. We point out that all graphs created are connected and symmetrical. Additionally, three sets of 10 initial conditions $\theta_0 \in \mathbb{R}^N$, with uniform distribution over $[0, 2\pi]$ and $N = 10, 50, 100$, have been explored. So, for each of the 90 coupling graphs we computed its correspondent I_c values by numerical integration of model (1) for $\varepsilon = 0, 0.01, \dots, 1.49, 1.50$.

In Table I, we report the mean value and the standard deviation of I_c for each topology and size of coupling graph. From these data, we see that the mean value of I_c increases if we go from tree to scale-free and to random graphs, respectively. However, this difference becomes less noticeable for larger values of N . Both the mean value and the standard deviation of I_c decrease with larger networks.

We have explored different networks metrics, searching for one mostly correlated with the convergence index I_c . Let $0 = \gamma_1 < \gamma_2 \leq \dots \gamma_N$ denote the Laplacian eigenvalues of the coupling graph.¹⁰ Recall that this graph is assumed to be simple and connected. We stress that these eigenvalues express fundamental characteristics of the graph. For instance, γ_2 is related with graph diameter and γ_N with its largest degree size.

We found that the quantity γ^* , defined as the ratio between the maximum eigenvalue and the average of the non-trivial eigenvalues of the Laplacian matrix of the graph, is rather suitable for this purpose. Formally, it is defined as

$$\gamma^* := \gamma_N \left(\frac{1}{N-1} \sum_{k=2}^{N-1} \gamma_k \right)^{-1}.$$

In Fig. 9, a correlation plot between I_c and measure γ^* for the correspondent graph is presented. From there, we observe a clear trend indicating that the greater the value of γ^* is, the smaller is the value of I_c . Independently of the network type and size, static regimes of partial synchronization,

TABLE I. Mean value of I_c and its standard deviation (in brackets) for each network type and size simulated.

Network	$N = 10$	$N = 50$	$N = 100$
Tree	0.421 (0.260)	0.016 (0.006)	0.008 (0.004)
Scale-free	0.857 (0.029)	0.050 (0.015)	0.013 (0.003)
Random	0.872 (0.090)	0.183 (0.063)	0.077 (0.022)

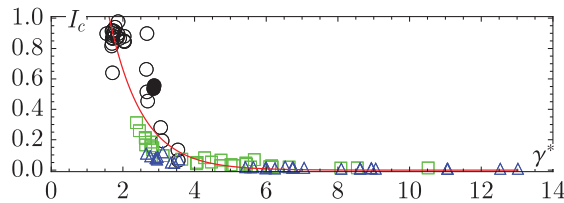


FIG. 9. Convergence index I_c versus γ^* . Networks with $N = 10, 50, 100$ nodes are represented as circles, squares and triangles, respectively. The two experiments from Fig. 2 are shown as disks. We show in red an exponential fit $f(x) = e^{1.7676 - 1.0894x}$ for the data.

full synchronization and phase-lock, are typical for values of $\gamma^* \leq 3$, like in the experiments from Fig. 2. On the other hand, graphs with larger values of this measure yields more irregular dynamics, like time-dependent periodic and chaotic regimes, as the ones from Fig. 8.

V. CONCLUSION

In this work, we introduced and studied the DHM, as a Kuramoto-like model of identical oscillators with non-linear coupling. Our main parameter was ε , which governs the coupling nonlinearity strength. It is clear that the most influence of nonlinearity in the coupling is on the hubs which experience strong forcing from many connected oscillators, while less connected nodes may still operate in a linear-coupling regime.

We proved that if this parameter is smaller than the inverse of the square of the maximum vertex degree in the network, then the full synchronized state is stable. Via numerical experiments, we showed that our model can display a variety of other qualitative behaviors of partial synchronization, like stationary phase locking, multistability, periodic order parameter variations, and chaotic regimes. We explored the relative abundance of stationary phase locking regimes under different network topologies. Our statistical analysis with 90 graphs, comprising a variety of network sizes and topologies and vertex sizes, suggests that tree graphs are much less likely to exhibit stationary phase locking in comparison with scale-free or random networks. In addition, this type of behavior becomes rarer if we increase network sizes, irrespective to the network topology. Finally, we also found a good correlation between the ration between the maximum eigenvalue and the average of the non-trivial eigenvalues of the Laplacian matrix of the graph, and the proportion of the repulsion parameter values which yield stationary phase locking. Our simulations show evidence that the greater this measure is, the smaller tend to be presence of stationary phase locking states in the system.

As a future research, we plan to investigate analytical conditions and correlations involving other graph measures related to other forms of synchronization in the model.

ACKNOWLEDGMENTS

We would like to thank the Coordenação de Aperfeiçoamento de Pessoal de Nível Superior—CAPES (Process: BEX 10571/13-2) for financial support. A.P. V.V. thanks the IRTG 1740/TRP 2011/50151-0, funded by the

DFG/FAPESP, CNPq, and the Grant/Agreement 02.B.49.21.0003 of August 27, 2013 between the Russian Ministry of Education and Science and Lobachevsky State University of Nizhni Novgorod.

- ¹J. A. Acebrón, L. L. Bonilla, C. J. Pérez Vicente, F. Ritort, and R. Spigler, "The Kuramoto model: A simple paradigm for synchronization phenomena," *Rev. Mod. Phys.* **77**(1), 137–175 (2005).
- ²K. T. Alligood, T. D. Sauer, and J. A. Yorke, *Chaos: An Introduction to Dynamical Systems. Chaos: An Introduction to Dynamical Systems* (Springer, New York, NY, 1997).
- ³Y. Baibolatov, M. Rosenblum, Z. Zh. Zhanabaev, M. Kyzgarina, and A. Pikovsky, "Periodically forced ensemble of nonlinearly coupled oscillators: From partial to full synchrony," *Phys. Rev. E* **80**(4 Pt 2), 046211 (2009).
- ⁴R. L. Burden and J. D. Faires, *Numerical Analysis* (Brooks Cole, 2010).
- ⁵F. Dörfler, M. Chertkov, and F. Bullo, "Synchronization in complex oscillator networks and smart grids," *Proc. Natl. Acad. Sci. USA* **110**(6), 2005–2010 (2013).
- ⁶G. Filatrella, N. F. Pedersen, and K. Wiesenfeld, "Generalized coupling in the Kuramoto model," *Phys. Rev. E* **75**, 017201 (2007).
- ⁷R. Follmann, E. E. N. Macau, E. Rosa, and J. R. C. Piqueira, "Phase oscillator network and visual pattern recognition," *IEEE Trans. Neural Netw. Learn. Syst.* **PP**(99), 1 (2014).
- ⁸A. Franci, A. Chaillet, and W. Pasillas-Lépine, "Phase-locking between kuramoto oscillators: Robustness to time-varying natural frequencies," in *49th IEEE Conference on Decision and Control (CDC)* (IEEE, 2010), pp. 1587–1592.
- ⁹C. Godsil and G. Royle, *Algebraic Graph Theory*, volume 207 of Graduate Texts in Mathematics, volume 207 of Graduate Texts in Mathematics (Springer, 2001).
- ¹⁰C. D. Godsil, G. Royle, and C. D. Godsil, *Algebraic Graph Theory* (Springer, New York, 2001), Vol. 207.
- ¹¹J. Gómez-Gardeñes, Y. Moreno, and A. Arenas, "Paths to synchronization on complex networks," *Phys. Rev. Lett.* **98**, 034101 (2007).
- ¹²H. Hong and S. H. Strogatz, "Kuramoto model of coupled oscillators with positive and negative coupling parameters: An example of conformist and contrarian oscillators," *Phys. Rev. Lett.* **106**, 054102 (2011).
- ¹³A. Jadbabaie, N. Motew, and M. Barahona, "On the stability of the kuramoto model of coupled nonlinear oscillators," in *American Control Conference, Proceedings of the 2004* (2004), Vol. 5, pp. 4296–4301.
- ¹⁴Y. Kuramoto, "Self-entrainment of a population of coupled non-linear oscillators," in *International Symposium on Mathematical Problems in Theoretical Physics*, edited by H. Araki, volume 39 of Lecture Notes in Physics (Springer, Berlin/Heidelberg, 1975), pp. 420–422.
- ¹⁵N. Ehrich Leonard, "Multi-agent system dynamics: Bifurcation and behavior of animal groups," *Annu. Rev. Control* **38**(2), 171–183 (2014).
- ¹⁶The reader can notice that if $\varepsilon < 0$ all oscillators are always attractive and the overall idea of the "deserter hubs" is lost. However, we would also have stable full synchronized state in this case as directly follows from Theorem 1.
- ¹⁷On the other hand, the minimum value of r^2 does not necessarily correspond to $R^2 = 0$.
- ¹⁸A. Papachristodoulou, A. Jadbabaie, and U. Munz, "Effects of delay in multi-agent consensus and oscillator synchronization," *IEEE Trans. Autom. Control* **55**(6), 1471–1477 (2010).
- ¹⁹L. M. Pecora and T. L. Carroll, "Master stability functions for synchronized coupled systems," *Phys. Rev. Lett.* **80**(10), 2109 (1998).
- ²⁰L. M. Pecora, F. Sorrentino, A. M. Hagerstrom, T. E. Murphy, and R. Roy, "Symmetries, cluster synchronization, and isolated desynchronization in complex networks," *Nature Communications* **5**, Art. No. 4079 (2013).
- ²¹A. Pikovsky and M. Rosenblum, "Self-organized partially synchronous dynamics in populations of nonlinearly coupled oscillators," *Physica D: Nonlinear Phenom.* **238**(1), 27–37 (2009).
- ²²O. V. Popovych, C. Hauptmann, and P. A. Tass, "Effective desynchronization by nonlinear delayed feedback," *Phys. Rev. Lett.* **94**(16), 164102 (2015).
- ²³M. Rosenblum and A. Pikovsky, "Self-organized quasiperiodicity in oscillator ensembles with global nonlinear coupling," *Phys. Rev. Lett.* **98**, 064101 (2007).
- ²⁴M. Sadilek and S. Thurner, "Physiologically motivated multiplex kuramoto model describes phase diagram of cortical activity," arXiv preprint [arXiv:1409.5352](https://arxiv.org/abs/1409.5352) (2014).
- ²⁵S. H. Strogatz, "From kuramoto to crawford: Exploring the onset of synchronization in populations of coupled oscillators," *Physica D: Nonlinear Phenom.* **143**(1), 1–20 (2000).
- ²⁶A. A. Temirbayev, Y. D. Nalibayev, Z. Zh. Zhanabaev, V. I. Ponomarenko, and M. Rosenblum, "Autonomous and forced dynamics of oscillator ensembles with global nonlinear coupling: An experimental study," *Phys. Rev. E* **87**, 062917 (2013).
- ²⁷A. A. Temirbayev, Z. Zh. Zhanabaev, S. B. Tarasov, V. I. Ponomarenko, and M. Rosenblum, "Experiments on oscillator ensembles with global nonlinear coupling," *Phys. Rev. E* **85**, 015204 (2012).
- ²⁸P. Tomov and M. Zaks, "Phase dynamics on small hexagonal lattices with repulsive coupling," in *Nonlinear Dynamics of Electronic Systems* (Springer, 2014), pp. 246–253.
- ²⁹L. S. Tsimring, N. F. Rulkov, M. L. Larsen, and M. Gabbay, "Repulsive synchronization in an array of phase oscillators," *Phys. Rev. Lett.* **95**, 014101 (2005).
- ³⁰E. Vassilieva, G. Pinto, J. de Barros, and P. Suppes, "Learning pattern recognition through quasi-synchronization of phase oscillators," *IEEE Trans. Neural Netw.* **22**(1), 84–95 (2011).

Appendix 3: Synchronization versus neighborhood similarity in complex networks of nonidentical oscillators

Synchronization versus neighborhood similarity in complex networks of nonidentical oscillatorsCelso Freitas^{*} and Elbert Macau[†]*Associate Laboratory for Computing and Applied Mathematics—LAC,
National Institute for Space Research—INPE, 12245-970, São José dos Campos, SP, Brazil*Ricardo Luiz Viana[‡]*Department of Physics, Federal University of Paraná—UFPR, 81531-990, Curitiba, PR, Brazil
(Received 10 January 2015; published 2 September 2015)*

Does the assignment order of a fixed collection of slightly distinct subsystems into given communication channels influence the overall ensemble behavior? We discuss this question in the context of complex networks of nonidentical interacting oscillators. Three types of connection configurations are considered: Similar, Dissimilar, and Neutral patterns. These different groups correspond, respectively, to oscillators alike, distinct, and indifferent relative to their neighbors. To construct such scenarios we define a vertex-weighted graph measure, the *total dissonance*, which comprises the sum of the dissonances between all neighbor oscillators in the network. Our numerical simulations show that the more homogeneous a network, the higher tend to be both the coupling strength required for phase locking and the associated final phase configuration spread over the circle. On the other hand, the initial spread of partial synchronization occurs faster for Similar patterns in comparison to Dissimilar ones, while neutral patterns are an intermediate situation between both extremes.

DOI: [10.1103/PhysRevE.92.032901](https://doi.org/10.1103/PhysRevE.92.032901)

PACS number(s): 05.45.Xt, 89.75.Fb

I. INTRODUCTION

Some social and biological studies about multiagents reveal that units tend to select similar peers with which to interact [1,2]. However, there are systems which behave in an opposite manner, where their components preferentially choose to connect themselves to others with some distinct inner characteristics [3]. In fact, nature seems to favor the former or the latter construction, which we respectively call *Similar* or *Dissimilar* (neighborhood) patterns, to achieve different agendas [4]. This article explores ideas inspired by these scenarios within the nonidentical-phase-oscillator Kuramoto model, which is one of the main paradigms to describe collective behavior and synchronization [5]. This model is also interesting because, under weak mutual interaction, it approximates dynamics of a large class of nonlinear oscillators near limit cycle [6]. Besides, this is an active research field with a number of applications from different areas [7–10], highlighting the fundamental role that synchronization plays.

Our numerical approach is based on a novel vertex-weighted graph measure: the *total dissonance*. This quantity can be regarded as a generalization of the classical concept of dissonance, that is, the natural frequency difference of two coupled oscillators [6]. So we define Similar and Dissimilar patterns as the assignments of nonidentical oscillators into the coupling graph which yield, respectively, significantly lower and higher total dissonance values. Otherwise, if a pattern has no strong bias related to this quantifier, then we call it *Neutral*. Given a fixed choice of inner properties for each oscillator and a fixed coupling graph, we search for Similar and Dissimilar patterns via an optimization algorithm interchanging oscillator's positions into the graph nodes.

Clearly, oscillator swapping over nodes of fully coupled networks have no influence over synchronization, since they can be solely seen as an index reordering. We focus in this work on networks whose quantity of edges is much smaller than the all-to-all case. Regular, scale-free, random, small-world, and community networks are considered [11] to provide evidence about the ubiquity of our argument. Finally, massive numerical simulations are performed to grasp the influence of these three different neighborhood patterns over phase-synchronization quantifiers.

About related material, Refs. [12] and [13], respectively, explore first- and second-order Kuramoto model versions, both including local correlations between oscillator's natural frequency and node degree. They report an explosive synchronization in the first case and cascade synchronization, according to the node degree, in the second. Our methodology introduces a diverse relationship between natural frequencies and coupling graph, as will be discussed and illustrated in the text.

Optimization studies also have laid the foundation for our research. In Ref. [14], an algorithm is proposed to construct optimized networks related to a combination of local and global synchronization measures. Their objective function is computed and refined after successive numerical integrations. Although we follow a different approach, we point out that our results also support that “the early onset of synchronization and rapid transition to the phase-lock are conflicting demands on the network topology” [14]. Reference [15] associates a percolation process to the spread of synchronization. In addition, they consider node interchange in the graph based on a vertex-weighted graph measure. However, their characterization takes into account only the phase sign of neighbor oscillator. Even so, we also found a similar explosive synchronization.

It is common sense that a way to achieve more homogeneous neighborhood patterns is to gather members with closer intrinsic dynamics into communities. Thus, articles

^{*}cbnfreitas@gmail.com[†]elbert.macau@inpe.br[‡]viana@fisica.ufpr.br

that investigate this framework can also benefit from our findings. Reference [16] addresses a Kuramoto model of identical oscillators showing that, as the transient time dies out, synchronization occurs in stages matching the granular communities of the coupling graph. Reference [17] deals with communities of oscillators having essentially different natural frequencies. The authors of this paper discuss ways to promote or suppress synchrony on individual subgroups. Reference [18] introduces a dynamic feedback control to produce intracommunities synchronization regarding communities of identical nonlinear oscillators. Accordingly, Similar, Neutral, and Dissimilar patterns can be used as an additional tool to tune synchronization properties.

II. MODEL AND METRICS

We consider a system of N phase oscillators, whose dynamics for the i th oscillator is

$$\dot{\theta}_i = \mathcal{W}_i + \frac{\varepsilon}{d_i} \sum_{j=1}^N A_{ij} \sin \theta_j - \theta_i, \quad (1)$$

where $\mathcal{W} = \mathcal{W}_1, \dots, \mathcal{W}_N \in \mathbb{R}^N$ are the oscillator's *natural frequencies*. We consider \mathcal{W} with zero mean [19], randomly drawn from the uniform distribution over $[-\pi, \pi]$. A single choice of \mathcal{W} is drawn for each network size N studied.

The *coupling strength* $\varepsilon \geq 0$ is the system parameter that adjusts the intensity of attractiveness between neighbor oscillators. The symmetrical *coupling graph* is expressed by its adjacency $N \times N$ matrix A , so $A_{ii} = 0$; $A_{ij} = 1$ if oscillators i, j are neighbors (adjacent), and $A_{ij} = 0$ otherwise. We assume connected graphs, meaning that there is a sequence of edges joining any two vertexes in the graph. Also, $d_i := \sum_j A_{ij}$ stands for the i th vertex degree. The Laplacian matrix is defined as $L := \text{diag } d_1, \dots, d_N - A$ and its eigenvalues are $0 = \lambda_1 \leq \lambda_2 \leq \dots \leq \lambda_N$. The first nontrivial eigenvalue λ_2 , the *algebraic connectivity*, is greater than zero if and only if the graph is connected [20].

On one hand, analytical results [21] guarantee convergence to a unique (modulus 2π) stable phase-locked regime, where phase differences between every two oscillators becomes constant. Precisely, this convergence occurs if the coupling strength ε is large enough in comparison with $\|\mathcal{W}\| \lambda_N / \lambda_2^2$, where $\|\cdot\|$ denotes the Euclidean norm in \mathbb{R}^N . Because λ_2 increases when the graph diameter D is decreased and λ_N decreases with its maximum degree d_{\max} [22], phase locking can be achieved for smaller values of ε mostly with the reduction of D but also with smaller values of $\|\mathcal{W}\|$ and d_{\max} . On the other hand, if we consider a system with only two phase oscillators, then it is well known [6] that the relation between its dissonance $\nu := \mathcal{W}_1 - \mathcal{W}_2$ versus the coupling strength ε determines the synchronization regime [23]. So we introduce the *total dissonance* measure for vertex-weighted graphs as

$$\nu_{\text{Total}} := \frac{1}{N} \sqrt{\sum_{i,j=1}^N A_{ij} \mathcal{W}_i - \mathcal{W}_j^2}. \quad (2)$$

Since we consider symmetrical and connected coupling graphs, it is straightforward to check that $\nu_{\text{Total}} = 0$ if and

only if all oscillator are identical. If we write $\nu_{\text{Total}} = \nu_{\text{Total}} \mathcal{W}$, then this measure quantifies how far \mathcal{W} is from a condition where all natural frequencies are identical. Therefore, ν_{Total} encompasses information about the total spreading of \mathcal{W} by summing up individual dissonances over the coupling graph edges.

The norm of the global mean field, the *order parameter*, will be denoted by $R\theta = |1/N \sum_{i=1}^N e^{i\theta_i}|$. This quantity R ranges from 0 to 1, respectively, indicating that the ensemble gradually changes from null global mean field, where all phasors $e^{i\theta_i}$ cancel out, to full synchronization, where $\theta_1 = \dots = \theta_N$. One also makes use of the *edge partial synchronization index* between two oscillators i, j ,

$$S_{ij} = S_{ji} := \left| \lim_{\Delta t \rightarrow \infty} \frac{1}{\Delta t} \int_{t_r}^{t_r + \Delta t} e^{i(\theta_i t - \theta_j t)} dt \right|,$$

where t_r is a large enough transient time [24]. Oscillators i, j are phase locked, that is, $\theta_i t - \theta_j t$ converges to a constant value if and only if $S_{ij} = 1$. Moreover, if this index is decreased towards zero, then weaker forms of synchronization and later uncorrelated trajectories occur [25]. We average contributions of all neighbor oscillators in the network to define the *partial synchronization index*

$$S := \frac{1}{\tilde{E}} \sum_{i,j=1}^N A_{ij} S_{ij}, \quad (3)$$

where $\tilde{E} := \sum_{i,j=1}^N A_{ij}$ is the quantity of directed edges in the graph. Of course, the number of undirected edges is $E := \tilde{E}/2$. Thus, $S = 1$ means that the whole ensemble is phase locked, while $S \approx 0$ yields very low coherent ensemble behavior. Note that $R[\theta t]$ converges to a constant value [26] if and only if $S = 1$.

An Adams-Bashforth-Moulton method for numerical integration is applied. A transient time of at least 2×10^3 units of time was suppressed from the data, while the convergence of approximations of S over successive time windows of 10^3 units of time was the criterion to interrupt the integration. The mean value of $R[\theta(t)]$ after the transient is denoted by $\langle R \rangle$. For a given choice of parameters and initial conditions, we indicate by ε_{PL} the smallest critical coupling strength $\varepsilon > 0$ inducing phase locking, i.e., $S = 1$ and $R[\theta t]$ converges to a constant value, which we denote by R_{PL} .

Several complex networks topologies [11] with N nodes and E (undirected) edges are considered: 4-Regular (N RE), Barabási-Albert (N BA), Erdős-Rényi (N ER), and Watts-Strogatz [27] (N WS). Experiments with relatively small networks with $N = 50$ are performed for the sake of easy visualization. Larger ones, with $N = 500$, are also addressed to illustrate graphs closer to the theoretical degree distribution [11], yet feasible to massive numerical integration. To diminish computational cost and to allow comparison among network topologies, we consider graphs with $\tilde{E} = 4N$ directed edges, which yields mean node degree $\langle d \rangle = \tilde{E}/N = 4$.

An empirical example of complex network with community structure, denoted by 105 CO, is included in the simulations: the Krebs-Amazon Political Books network [28]. This graph

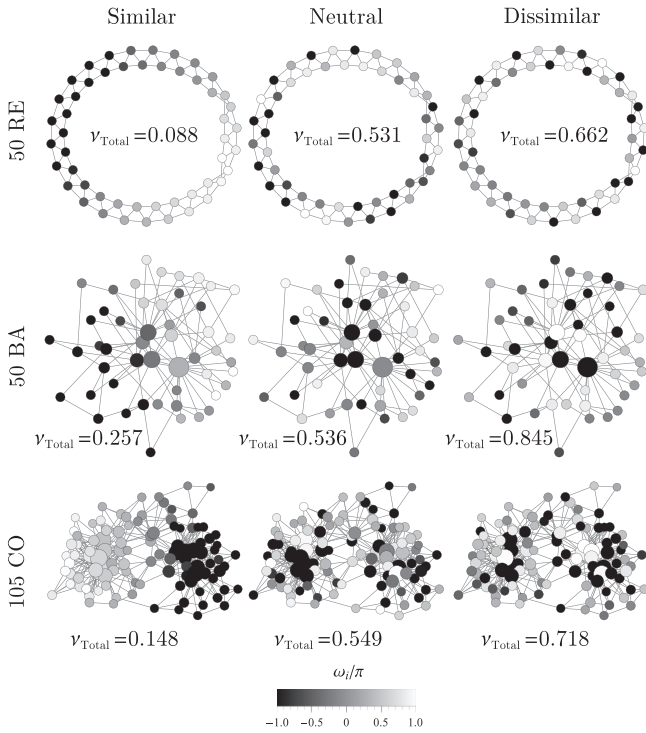


FIG. 1. Examples of Similar, Neutral, and Dissimilar patterns related to N -node graphs following network topology: 4-Regular (N RE); Barabási-Albert (N BA), with $E = 100$ edges and a community graph (N CO) with $E = 441$. Vertex color is presented according to its natural frequency \mathcal{W}_i , ranging from $-\pi$ (black) to π (white); vertex size is proportional to node degree. The associate total dissonance ν_{Total} is displayed.

comprises $N = 105$ nodes, $\tilde{E} = 882$ edges, and two communities.

Our aim now is to make precise the subjective idea of Similar, Neutral, and Dissimilar patterns based on member's local choice of neighbors. Only oscillator swapping among the graph nodes are taken into account. Similar patterns should place oscillators alike into adjacent graph nodes. Thus, a way to achieve it for RE networks is to assign extreme natural frequency values, close to $\pm\pi$, as far as possible in the graph, filling intermediate nodes with gradual values of \mathcal{W}_i ; see Fig. 1 (50 RE Similar).

To consolidate this concept for more general network topologies, a numerical procedure is chosen as a definition. We will call the Similar configuration the permutation obtained by minimizing the objective function $\nu_{\text{Total}}\mathcal{W}$, which corresponds to minimize the dissonance $\mathcal{W}_i - \mathcal{W}_j$ over all edges i, j of the graph. In contradistinction, Dissimilar configurations will be associated with maximization of the total dissonance. For this purpose, a simulated annealing optimization method (SA) [29] is employed to track permutations of \mathcal{W} towards optimal solutions [30].

The reader must be aware that although the SA returns permutations enhancing the objective function value, this is a stochastic scheme, which means that only with infinite iterations one could expect to achieve the global optima regarding all $N!$ permutations. Nevertheless, whether these

numerical approximations of the total dissonance $\nu_{\text{Total}}\mathcal{W}$ values are the global extremes values is not strictly relevant to our analysis.

Medium to large networks with a quantity of edges much smaller than the fully coupled case are the focus of the present study. Therefore, an initial random assignment of \mathcal{W} into the graph nodes, without any optimization process, will be called a neutral configuration. We take this approach by simplicity, because the total number of permutations $N!$ becomes so massive that the probability of randomly drawing a permutation such that ν_{Total} is close to the extreme values is very small, as is numerically confirmed below.

In conclusion, we derive from each pair A, \mathcal{W} the Neutral configuration, without optimization, and the Similar and Dissimilar ones by means of numerical minimization and maximization of $\nu_{\text{Total}}\mathcal{W}$ [31], respectively. We defer to future research the study of other values of this metric, between Similar-Neutral and Neutral-Dissimilar, versus synchronization features.

Figure 1 illustrates RE, BA, and CO graphs with the three neighborhood patterns. As expected, from the RE graph with Similar configuration of this figure, one realizes a homogeneous transition of \mathcal{W}_i values. Each node presents indeed natural frequency close to the respective average of its neighbors. However, this ordering arises differently depending on the network topology. Hubs of the BA graph were colored with medium gray tones, corresponding to the overall mean of natural frequency distribution. But in the CO graph, positive and negative natural frequency values were placed into distinct communities, with hubs close to $\pm\pi/2$ and central nodes (in between communities) close to null \mathcal{W}_i .

Regarding the Dissimilar configurations from Fig. 1, the opposite organization is found: each node receives natural frequency far from its neighbors. For the RE network, we notice sequences of connected nodes with alternating positive and negatives values of \mathcal{W}_i . Moreover, BA and CO graphs presented connected hubs with larger natural frequencies and opposite signs. Eventually, the Neutral configuration can be regarded as a blending between both previous configurations.

We randomly generate and include in our experiments 100 graphs of BA, ER, and WS network topologies in the next experiments. Since RE topology is deterministic and the CO graph was extracted from a data set, these classes contain a single member to be analyzed.

Figure 2 displays a distribution chart of the total dissonances ν_{Total} obtained for the categories included in this article. From this figure, a sharp distinction among patterns is noticed, since there is no ν_{Total} range overlapping within each category. Although this three-cluster structure arose from our data dealing with a variety of networks, it depends on the network size, topology, and suitable optimization algorithm. For instance, if the optimization output were not sufficiently far from the mean of the total dissonance distribution, then these patterns would have no meaning.

The set of graphs with $N = 500$ presented values of ν_{Total} 3 times smaller than the set with $N = 50$. Furthermore, both sets were qualitatively alike, which is an evidence that we were capable to produce Similar and Dissimilar neighborhoods in the large networks, at least as well as the small ones.

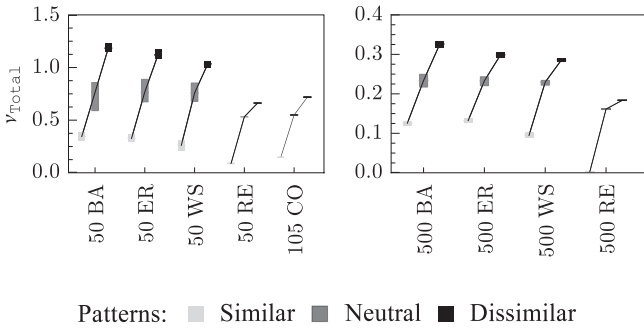


FIG. 2. Total Dissonance ν_{Total} distribution chart of different topologies with Similar (light gray), Neutral (gray), and Dissimilar (black) patterns. Data correspond to the single members from categories 50 RE, 500 RE, and 105 CO and 100 different elements for the others. Colored bars indicate the overall range of ν_{Total} obtained, while mean values of each distribution are joined by a black line within each category.

Because there is only a normalization by the number of vertices in the graph, but not by the quantity of edges, in Eq. (2), the total dissonance decreases with smaller mean degrees in all categories as expected [32]. BA, ER, and WS topologies were almost indistinguishable in the Neutral pattern but were slightly higher in this order for the Dissimilar case. All patterns of 50 RE and 105 CO graphs yielded smaller but comparable with each other total dissonance values.

We use notation and also denote by S , $\langle R \rangle$, ε_{PL} , and R_{PL} the associated mean values of these synchronization quantifiers considering all graphs of each category. A fixed random choice of initial condition $\theta^0 \in \mathbb{R}^N$ is drawn from a uniform distribution over the unit circle for each network size N . So Fig. 3 displays the values of S and $\langle R \rangle$, as solid and dashed lines, respectively, obtained through numerical integration for the three neighborhood configurations colored like in Fig. 2. The time variable of both S and $\langle R \rangle$ times series are rescaled to end at the associated mean critical coupling value ε_{PL} . The S lines finish at value 1, within the numerical tolerance, while

the final value of $\langle R \rangle$ lines equal to the mean critical order parameter R_{PL} .

First, one focus on the phase-locking measures ε_{PL} and R_{PL} . Irrespective to network size, overall results were alike. In general, ε_{PL} decreases from Similar, Neutral, to Dissimilar patterns; while R_{PL} tend to increase in the same ordering. In all topologies, Similar cases demanded higher coupling strength to achieve phase locking. In particular, since this holds true even for RE networks, it shows that total dissonance patterns induce a different phenomenon than the ones from Refs. [12,13].

Moreover, even when these networks were phase locked, R converged to smaller values of R_{PL} . In other words, Similar ensembles tend to be harder to synchronize and to converge to regimes where oscillators were more spread around the unit circle than their counterparts. Neutral patterns required smaller ε_{PL} than Dissimilar ones. RE graphs were the only exception for these behavior of R_{PL} .

For all topologies, higher values of ε_{PL} were measured when N was multiplied by 10. On the other hand, larger networks yielded higher R_{PL} for Similar and Neutral neighborhoods but slightly smaller R_{PL} for Dissimilar ones.

At this point, the influence of Similar, Neutral, and Dissimilar patterns over the emergence of phase synchronization is investigated, especially related to coupling strengths ε much smaller than ε_{PL} .

Again, except for RE graphs, we verify that Similar patterns favor weaker synchronization regimes, since the initial growth of S and $\langle R \rangle$ for small coupling strength ε is more prominent. However, beyond intermediate values of ε , Dissimilar patterns surpass the Similar ones through an abrupt transition. The Neutral case is between these two extremes, closer to the behavior of the Dissimilar group. If we compare network topologies, BA and ER graphs displayed close values of S , which were smaller than WS ones for small and intermediate values of ε .

A parallel of our findings could be made by considering conflicting ideas, associating communication and agreement with the emergence of synchronization and phaselocking,

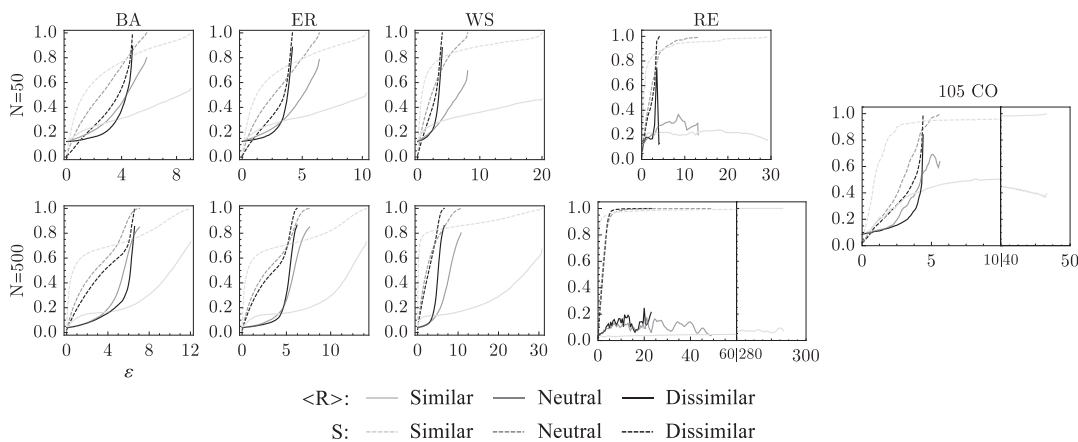


FIG. 3. Mean order parameter after transient $\langle R \rangle$ and partial synchronization index S , solid and dashed lines respectively, as a function of coupling strength ε for different graph topologies. Average values of all graphs simulated within each category are shown. Similar, Neutral, and Dissimilar cases are respectively plotted in light gray, gray, and black. Lines are drawn to ε equal to the respective average critical phase locking ε_{PL} .

respectively. In Similar scenarios, interaction mostly occurs among people with closely related culture backgrounds. Thus, communication can easily spread locally, but the overall population, which contains diverse members, will hardly find a compromise. On the other hand, when networks contain more heterogeneous neighbors, as in the Neutral and Dissimilar cases, communication demands higher effort to be established. But after that, the whole ensemble is capable to rapidly reach consensus.

In summary, experiments with several network topologies were analyzed and a strong numerical trend was found. The Neutral case behaves in general between both extremes, closer to the Dissimilar case. Except for RE networks, under small coupling strength ε , Similar patterns yield larger values of

partial synchronization index S , meaning early synchronization ongoing. In contradistinction, Dissimilar ones present smaller values of S but undergo abrupt increment until phase locking. Moreover, all networks with Similar patterns required higher values of coupling strength to achieve phase locking, while Dissimilar patterns converged to regimes closer to full synchronization.

ACKNOWLEDGMENTS

We thank the Coordenação de Aperfeiçoamento de Pessoal de Nível Superior—CAPES (Process No. BEX 10571/13-2), CNPq, and FAPESP (Grant No. 2011/50151-0) for financial support.

-
- [1] J. V. Hamm, *Dev. Psychol.* **36**(2), 209 (2000).
- [2] H. Abadzi, *J. Educ. Res.* **79**, 36 (1985).
- [3] T. B. Reusch, M. A. Haèberli, P. B. Aeschlimann, and M. Milinski, *Nature* **414**, 300 (2001).
- [4] C. Lozares, J. M. Verd, I. Cruz, and O. Barranco, *Qual. Quant.* **48**, 2657 (2014).
- [5] Y. Kuramoto, *Chemical Oscillations, Waves, and Turbulence*, Springer Series in Synergetics (Springer-Verlag, Berlin, 1984).
- [6] A. Pikovsky, M. Rosenblum, and J. Kurths, *Synchronization: A Universal Concept in Nonlinear Sciences*, Cambridge Nonlinear Science Series (Cambridge University Press, Cambridge, 2003).
- [7] S. H. Strogatz, *Nature* **410**, 268 (2001).
- [8] A. Arenas, A. Díaz-Guilera, J. Kurths, Y. Moreno, and C. Zhou, *Phys. Rep.* **469**, 93 (2008).
- [9] G. Filatella, A. H. Nielsen, and N. F. Pedersen, *Eur. Phys. J. B* **61**, 485 (2008).
- [10] R. Follmann, E. E. N. Macau, E. Rosa, and J. R. C. Piqueira, *IEEE Transactions on Neural Networks and Learning Systems* **26**, 1539 (2015).
- [11] M. v. Steen, *Graph Theory and Complex Networks: An Introduction* (Maarten van Steen, Lexington, 2010).
- [12] J. Gómez-Gardeñes, S. Gómez, A. Arenas, and Y. Moreno, *Phys. Rev. Lett.* **106**, 128701 (2011).
- [13] P. Ji, Thomas K. D. M. Peron, P. J. Menck, F. A. Rodrigues, and J. Kurths, *Phys. Rev. Lett.* **110**, 218701 (2013).
- [14] M. Brede, *Eur. Phys. J. B* **62**, 87 (2008).
- [15] X. Zhang, Y. Zou, S. Boccaletti, and Z. Liu, *Sci. Rep.* **4**, 5200 (2014).
- [16] A. Arenas, A. Díaz-Guilera, and C. J. Pérez-Vicente, *Phys. Rev. Lett.* **96**, 114102 (2006).
- [17] M. Komarov and A. Pikovsky, *Phys. Rev. Lett.* **110**, 134101 (2013).
- [18] K. Wang, X. Fu, and K. Li, *Chaos* **19**, 023106 (2009).
- [19] Without loss of generality, otherwise this mean value can be absorbed into the space stated and eliminated with a coordinate change.
- [20] C. Godsil and G. Royle, *Algebraic Graph Theory*, Graduate Texts in Mathematics, Vol. 207 (Springer-Verlag, New York, 2001).
- [21] A. Jadbabaie, N. Motee, and M. Barahona, in *Proceedings of the American Control Conference, 2004*, Vol. 5 (IEEE, New York, 2004), pp. 4296–4301.
- [22] J.-S. Li and X.-D. Zhang, *Linear Algebra Appl.* **285**, 305 (1998).
- [23] Arnold Tongues, for instance, can describe this interplay [6].
- [24] J. Gómez-Gardeñes, Y. Moreno, and A. Arenas, *Phys. Rev. Lett.* **98**, 034101 (2007).
- [25] C. B. N. Freitas, E. E. M. Macau, and R. L. Viana, in *Proceedings of the 22nd International Congress of Mechanical Engineering (Brazilian Association of Engineering and Mechanical Sciences, Ribeirão Preto, SP, Brazil, 2013)* pp. 10334–10339.
- [26] It is straightforward to check that this constant value cannot be the unit for nonidentical oscillators.
- [27] Watts-Strogatz networks with rewiring probability of 0.25 are considered.
- [28] Data-set description at <http://www.orgnet.com/> and adjacency matrix from <http://moreno.ss.uci.edu/data.html>.
- [29] S. Kirkpatrick, *J. Stat. Phys.* **34**, 975 (1984).
- [30] Actually, successive iterations of the SA using three strategies for node interchange are applied. First, nodes to be swapped are drawn with probability proportional to vertex degree, since they are the ones which influence the most ν_{Total} . We also pick vertexes to be interchanged only within the same modularity-based community. Thus, we can focus the optimization process on relatively detached graph regions. Last, to facilitate escape from local critical points and also to fine adjustments, we consider all nodes equiprobable.
- [31] The essential purpose of the total dissonance ν_{Total} in this work was to lay constructive foundation for Similar, Neutral, and Dissimilar configurations. One could reformulate these concepts based on variations of Eq. (2).
- [32] From the optimization point of view, the normalization by any constant value, whether the number of edges E or the quantity of nodes N , does not influence the Similar and Dissimilar configurations obtained. We opt not to normalize by E to reflect that the more edges a graph contains, the more conflicting pairs of dissonances exist in the network, which yields higher total dissonance.